



**UNIVERSITÀ DEGLI STUDI DI PADOVA**  
**Dipartimento di Fisica e Astronomia “Galileo Galilei”**  
**Master Degree in Astrophysics and Cosmology**

**Final Dissertation**

**Very High Energy observations of the blazar  
1ES1959+650 with the Large-Sized Telescope (LST-1) in  
La Palma**

**Thesis supervisor**

**Prof. Elisa Bernardini**

**Thesis co-supervisor**

**Dr. Mireia Nievas Rosillo**

**Candidate**

**Gaetano Di Marco**

**Academic year 2021/22**



*"Science presents a picture of the world which is much richer in content than what the unaided eye discerns. But science itself teaches us also that it is richer than the unaided eye can discern. For science itself delineates, at least to some extent, the observable parts of the world it describes. Measurement interactions are a special subclass of physical interactions in general. The structures definable from measurement data are a subclass of the physical structures described."*

Bas C. van Fraassen, *The scientific Image*, 1980

# Contents

<b>Abstract</b>	<b>i</b>
<b>1 Introduction</b>	<b>1</b>
<b>2 Blazars</b>	<b>5</b>
2.1 Phenomenology of Blazar spectra . . . . .	9
2.2 High-Peaked BL Lac objects . . . . .	10
2.2.1 Past investigations on 1ES1959+650 . . . . .	10
<b>3 Large-Sized Telescope LST1 and lower frequencies telescopes</b>	<b>13</b>
3.1 LST1 characteristics . . . . .	13
3.2 Cherenkov Telescope Array North perspectives . . . . .	15
3.3 Overview on other instruments . . . . .	16
3.3.1 Fermi-LAT in $\gamma$ -rays . . . . .	16
3.3.2 <i>Swift</i> -XRT in X-rays . . . . .	18
3.3.3 TELAMON program in radio . . . . .	18
<b>4 LST1 data analysis pipeline</b>	<b>20</b>
4.1 Tools and Software . . . . .	20
4.2 From waveforms to direction and energy reconstruction . . . . .	22
4.3 Final data reduction stages . . . . .	26
4.3.1 The simulated instrument response . . . . .	27
4.3.2 Generation of the event files . . . . .	30
4.4 Source dependent and source independent analysis . . . . .	30
4.5 Scientific products . . . . .	33
<b>5 Data reduction of 1ES1959+650 LST1 observations</b>	<b>36</b>
5.1 Data selection . . . . .	36
5.2 Detection plots . . . . .	39
5.3 Applied Instrument Response Functions . . . . .	41
<b>6 Results of 1ES1959+650 analysis</b>	<b>44</b>
6.1 Spectral modeling and fit of high level data . . . . .	44
6.2 Total dataset: two years of observations . . . . .	49
6.3 Energy-dependent cuts to discern $\gamma$ -rays from protons . . . . .	52
6.4 Combination with Fermi-LAT observations . . . . .	55
6.4.1 Broadband modelling of the $\gamma$ -ray emission . . . . .	57
6.4.2 Dependency of the spectral index on the source flux . . . . .	58
6.5 Multiwavelength light curve of the blazar . . . . .	60
<b>7 Conclusions</b>	<b>63</b>
7.1 Summary . . . . .	63

7.2	Results and future perspectives . . . . .	63
<b>A</b>	<b>Details on data quality selection</b>	<b>67</b>
<b>B</b>	<b>Physics of blazar emission</b>	<b>70</b>
B.1	Radiative processes . . . . .	70
B.1.1	Relativistic beaming . . . . .	70
B.1.2	Synchrotron radiation . . . . .	71
B.1.3	Inverse Compton . . . . .	72
B.1.4	Hadronic processes . . . . .	73
B.2	Results from 1ES1959+650 literature . . . . .	74
<b>C</b>	<b>Statistical tools</b>	<b>76</b>
C.1	Li&Ma significance . . . . .	76
C.2	Power Law decorrelation energy . . . . .	76
C.3	Statistic in Gammapy fits . . . . .	77
C.4	Fractional variability amplitude . . . . .	77



# Abstract

**Context** In the context of  $\gamma$ -ray astronomy, Cherenkov Telescope Array (CTA) observatory is the next generation of Cherenkov telescopes. These detect and image Cherenkov light because of the particles moving in the atmospheric medium produced by the interaction of  $\gamma$ -rays with the atmosphere.

With sites in both hemispheres and three telescope sizes, CTA experiment is going to perform high sensitivity observations in the High Energy (between 100 MeV and 100 GeV) and Very High Energy (larger than 100 GeV) bands. Among the three sizes, the Large-Sized Telescope (LST) has the lowest energy threshold at 20 GeV and it detects photons up to tens of TeV. They dominate the performance of CTA from 20 GeV to 300 GeV.

LST1 is the first LST Northern CTA telescope built in 2018 in Roque de Los Muchachos Observatory (ORM), La Palma, Spain.

A better angular resolution and energy reconstruction compared to the predecessors can be achieved thanks to the large amount of telescopes involved, the different sizes and technological developments. CTA will allow for new science to be done.

Among all the  $\gamma$ -ray sources, Active Galactic Nuclei (AGNs) are one of the most intriguing and fascinating objects. Blazars are a class of AGNs: they are characterized by a strongly beamed jet pointing towards us and a typical broad non-thermal Spectral Energy Distribution (SED) that presents two-humps, one in the Low Energy (LE), originated by synchrotron emission by ultra-relativistic electrons, and the other in High Energy, between MeV and GeV, commonly attributed to inverse Compton (IC) in the leptonic scenario. Depending on the broadness of optical emission lines and their luminosity, blazars are classified into Flat Spectrum Radio Quasars and BL Lac Objects.

In BL Lacs the lines and the emission from the dusty torus surrounding the central black hole are dim or absent. An interesting class of those is the High Frequency peaked BL Lac type object (HBL): it has a distinctive LE peak at the ultra-violet/X-ray frequencies.

1ES1959+650 is a quite close ( $z=0.047$ ) TeV HBL, discovered as  $\gamma$  emitter in 1999 by Telescope Array. Regular observations over the years spot an extreme behaviour during the flare states: the Low and High Energy peaks shift towards the extreme-HBL regime and the SED deviates from the Blazar Sequence expectations.

While the source was reaching its highest  $\gamma$ -ray flux since 2002, an extended Multiwavelength (MWL) campaign was carried out in 2016 by *Swift*, *Fermi*-LAT and MAGIC. Such a MWL analysis brought to broaden the knowledge on the source emission processes.

**Aims** The aim of the Thesis is to perform a deep study of the observations performed by the LST1 telescope from 2020 up to May 2022. Emphasis is given to LST1 data analysis from raw data to scientific products.

The analysis steps are followed in all details to estimate 1ES1959+650's emission evolution with time and spectrum. Each analysis phase has been examined and then, if needed, modified and implemented according to the peculiarities of 1ES1959+650's observations (for instance, it is usually observed at large zenith angles). One of the thesis' aims is to compare different approaches to the analysis.

Properties of the blazar light curve and spectrum, as observed by LST1, are analysed together with Fermi-LAT (in  $\gamma$ -rays), *Swift*-XRT (in X-rays) and TELAMON project (in radio) observations.

**Methods** Firstly, quality checks both on data and LST1 performances are accomplished. It is useful to monitor noise levels and the camera optical efficiency; the latter is evaluated by analysing the muon traces.

LST1 data is organized in data levels: it starts from waveforms of signal coming from the shower as detected by the telescope's camera. Those are calibrated and then the number of photons and the mean arrival time is estimated in order to parametrize the trace in the camera. At this stage, we can determine the nature of incident particle (being it a cosmic or  $\gamma$  ray) through a comparison with simulated shower events, as well as its reconstructed energy and arrival direction. Lastly, the simulations of the response of the telescope are incorporated: they are ready to be employed to produce scientific results, such as SEDs, Light Curves and Differential Fluxes.

The effective contribution of 1ES1959+650 analysis begins at the level in which the shower's traces are parametrized. Machine learning techniques are applied to estimate the shower arrival direction, its energy and the nature of the shower, being either of proton or gamma origin.

All the low level steps are performed by the specific LST1 tools, `lstchain`. It relies on a framework that contains `Python` scripts and functions to pass from a level to another, read and train simulated data, check and select data, plot the camera, perform calibration.

As the High Level Analysis concerns, the official Tools library of CTA, `Gammapy`, is used. It is employed to store data, to create binned maps of the sky and the background regions. Then, through a Likelihood fit, the flux points are estimated and the scientific results are produced.

**Results** From the selected 11 nights of 1ES1959+650 observation, the detection plots with the associated significance reveal a consistent detection of the source.

In the Higher analysis level, after checking the migration energy matrix (reconstructed energy *vs* "true" energy from the IRFs) and the exposure area plot, the 1ES1959+650 data are fitted through a `LogParabola` model, with the energy range defined by simulated event statistics. SEDs and Differential fluxes of different datasets are shown, discussed and compared. Performing energy-dependent  $\gamma$ /hadron separation gives better results, especially in the spectrum. Then, those LST1 results would be examined in relation to the past analysis in literature.

A `Python` code, employing `lstchain` and `Gammapy` tools, has been developed and implemented to perform the Higher level and to depict the mentioned plots.

As the MWL campaign concerns, it has been found that the Fermi-LAT and LST1 independent analysis are compatible, useful to determine the location of the HE peak in the SED. Spectral evolution analysis of the two  $\gamma$ -ray detectors reveals a smooth *softer when brighter* trend. Comparing the light curves in different frequencies, an intra-week flare in May 2022 is detected and characterized.

**Conclusions** 1ES1959+650 has lots of open questions that have still to be answered. They are on the emission mechanisms of the source, what caused the flare states and if detected CRs or neutrinos can be related to the source. MWL and Multimessenger campaigns could enrich our knowledge on the source and on HBL objects in general.

Open issues and possible development in LST pipeline are also discussed: LST1 (and next CTA telescopes) will play a significant role in that way.

The Thesis is going to be part of this context. Handling the latest LST data analysis tools, the aims are the monitoring and studying of 1ES1959+650 activity, providing the first analysis of data from this source taken with a CTA telescope. It is corroborated by a preliminary MWL analysis.

# Chapter 1

## Introduction

In the '50s, a new and peculiar class of extragalactic objects arose from radio observations: they were discovered as radio galaxies [41]. Those were years of great turmoil for the Astrophysics research: cosmic rays and the radio emission from our Galaxy had already been discovered, respectively in 1913 by Victor Hess and in 1933 by Karl Jansky, as well as Galactic radio sources. As the new extragalactic radio sources regard, the most remarkable discovery was of the radio emitter Cygnus A<sup>1</sup>, embedded in a  $z=0.057$  galaxy. Its emission turned out to be more powerful than our Galaxy more than one million times. Another crucial point was the discovery of the M87 radio galaxy optical jet [65]: it was attributed to synchrotron radiation (appendix B.1.2). Moreover, more and more optical observations revealed the existence of *quasi-stellar* objects, so-called Quasar.

The development of astronomical instrumentation allowed further discoveries of similar sources and a much better characterization, especially from a spectral and morphological point of view. It became evident that many of the radio galaxies were also Quasars. Those were found to be related to other intermediate sources, Seyferts: the merging of the two brought to the unification scheme [64] and a new family of objects.

They were called **Active Galactic Nuclei (AGNs)** because of their common compactness, brightness and structure. Another distinctive property is their intrinsic broad-band spectrum, i.e. they emit over a large range of wavelengths, from radio photons up to **Very High Energy (VHE)**  $\gamma$ -rays<sup>2</sup>. From the fifties, AGNs became one of the most interesting and intriguing extragalactic objects. The unrevealed mysteries about their emission mechanisms, and the (ultra-)relativistic particles behind, have made AGNs as one the challenges of past, actual and future Astrophysics research.

Among AGNs, **Blazars** are recognized for their jet outflowing the central core and a high flux variability: Blazars are a special AGNs' class since the jet points toward us .

In the early low-frequency range radio surveys, these objects emerged for their peculiar flat radio spectra. During some '60 studies, the compact, variable and radio-flat object VRO 42.22.01 was found to be spectrally related to the *variable star* BL Lacertae [43]. Such famous *star* became the prototype of the AGNs subclass of **BL Lacertae**, or BL Lac, objects. The population of the so called at that time *optically, violently variable* objects (OVVs) was associated with such BL Lacs.

The term blazar was employed to embrace the two closely related families of AGNs: BL Lacs and the OVVs.

Since the 1950s, blazars have been studied in more and more details as the astronomical tech-

---

<sup>1</sup>The observation was carried on by Minkowski and Baade in 1954.

<sup>2</sup>Not all of them emit significantly in all the wavelengths. For instance, from Seyferts is not observed an emission beyond the X-rays [16].

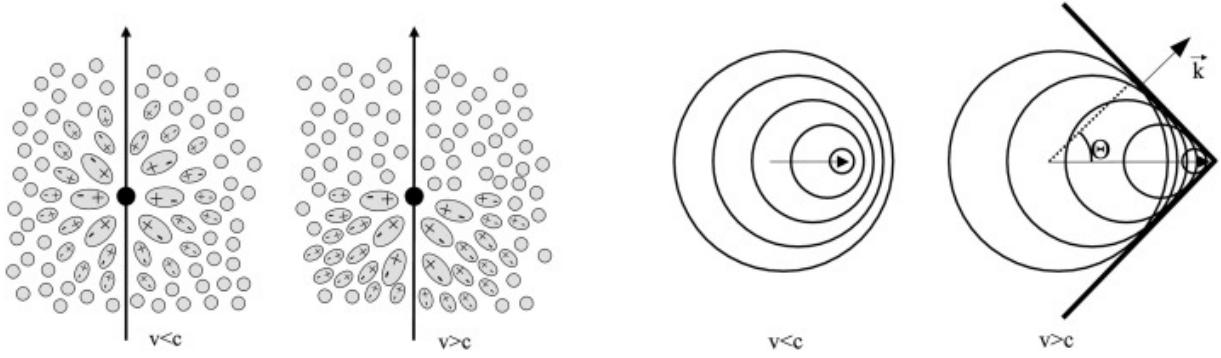


Figure 1.1: (left) Polarization of the medium in relation to the velocity of the ultra-relativistic particle. (right) Wavefronts in dependence on  $v$ . For  $v > c$ , the Cherenkov cone is depicted [42].

nology developed: in particular, higher and higher wavelength emission detection, up to  $\gamma$ -rays, have allowed broader studies of these sources.

In the field of VHE observations, the pioneer was the Whipple 10 m  $\gamma$ -ray telescope (Southern Arizona, United States), in operation since 1968 and decommissioned in 2013. It exploits the Imaging Atmospheric Cherenkov Technique (IACT) to detect photons with an energy  $\gtrsim 100$  GeV, canonical lower threshold to define VHE astronomy. Telescopes relying on IACT detect indirectly  $\gamma$ -rays thanks to ground-based instruments.

The IACT detection of  $\gamma$ -ray works as follows. The incoming VHE  $\gamma$ -ray interacts with the atmosphere, generating an Extensive Air Shower. This happens since the incoming photon undergoes pair production in the proximity of an atmospheric nucleus. It usually occurs at an altitude between  $\sim 10$ -20 km from the sea level<sup>3</sup>.

The electron-positron pair generates high energy photons through Bremsstrahlung, which in turn, produce more pairs. The process continues until the photons' energies are no more enough to produce pairs, so the cascade regresses. The charged particles in the cascade are so energetic that induce a polarization in the medium that, then, beget **Cherenkov light** flashes of a duration  $\sim 5$ -20 ns (figure 1.1) [42].

IACT telescopes image these short flashes, collecting and focusing Cherenkov photons thanks to large mirrors. A comprehensive scheme about how Cherenkov telescopes work is in 1.2. The main problems of IACTs are due to possible sources of light (starlight, Moon etc.), atmosphere evolution and Cherenkov light-absorption during the night (clouds, air glow etc.) and the (isotropic) cosmic-ray background. In particular, the latter produces showers as well as  $\gamma$ -rays, but with different characteristics and developments. To discriminate  $\gamma$ -rays from cosmic-rays on an event basis we can rely on statistical techniques, based on Machine Learning approaches. It is useful to claim or not  $\gamma$  detection.

Nowadays, the operating IACT experiments<sup>4</sup> are: High Energy Stereoscopic System (H.E.S.S.), Major Atmospheric Gamma Imaging Cherenkov Telescopes (MAGIC), First G-APD Cherenkov Telescope (FACT) and Very Energetic Radiation Imaging Telescope Array System (VERITAS). Since 2018, another telescope started observing from La Palma (Canary Islands, Spain) in those energy bands: the first **Large-Sized Telescope** prototype (**LST1**) of Cherenkov Telescope Array (**CTA**) project.

<sup>3</sup>The pair-production process can take place, in the field of the nucleus, only if the  $\gamma$ -ray energy ( $\hbar\omega$ ) is greater than the rest energy of the products ( $2 \cdot m_e c^2$ ). The *mean free path* of a  $\gamma$ -ray going through the atmosphere depends on the *cross section* of the pair-production process, in the well-known relation  $\lambda \sim (n \cdot \sigma_{pair})^{-1}$ ,  $n$  volumetric particle density.  $\sigma_{pair}$  depends on the atomic number of the medium and the energy of the incoming  $\gamma$ -ray. In general, the altitude at which the  $\gamma$ -ray undergoes the first pair production is expressed in terms of the **radiation length**  $\xi_{pair} = M_A / N_{Avogadro} \sigma_{pair}$ , with  $M_A$  atomic mass.

<sup>4</sup>The current generation is called the "third generation" of Cherenkov telescopes.

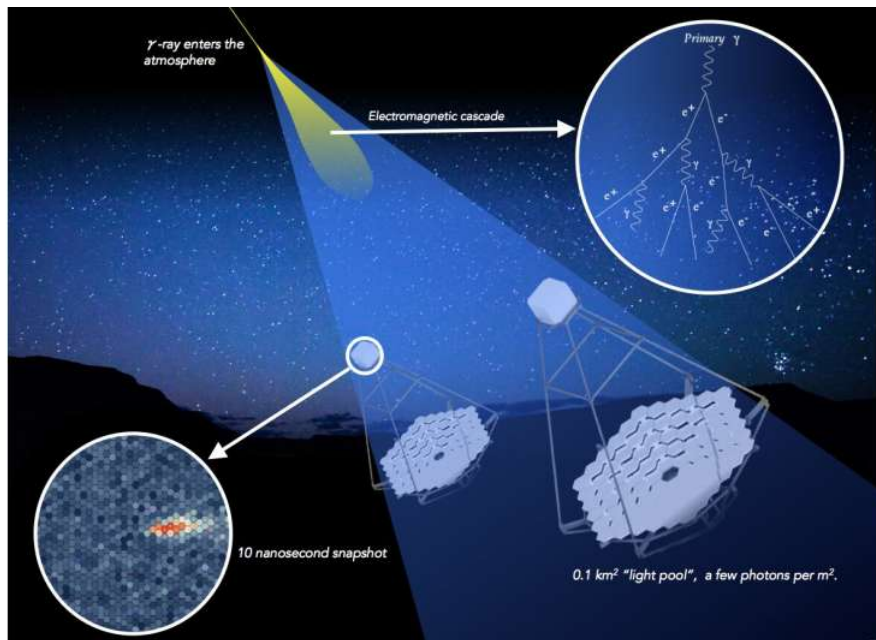


Figure 1.2: Schematic picture on how Cherenkov Telescopes detect VHE  $\gamma$ -rays. On the *left-bottom*, the Cherenkov light trace in the telescope's Camera. *Credit: Cherenkov Telescope Array Observatory (CTAO).*

The present work is utterly placed in the context just introduced: it is going to be the first analysis from LST1 observations of the blazar **1ES1959+650**.

LST1 is the first telescope of the forthcoming CTA observation era. The multinational CTA project will improve VHE Galactic and extragalactic observations' performances with sites in both hemispheres and three classes of telescopes (in total, almost 120 ground-telescopes are going to be installed). The declared goals of CTA collaboration spread from the investigation on relativistic cosmic particles to the dark matter *hunting* [2], also thanks to synergies with many of the major astronomical observatories and astroparticle experiments.

1ES1959+650 is classified as a High Frequency peaked BL Lacertae object, a blazars' subclass. Its measured redshift is of 0.047.

It was discovered as radio source in 1987 during a survey performed by the 91-m NRAO Green Bank Radio Telescope. Since then, further and new observations have been following in the radio, optical (NOT observation in 1.3) and X-ray<sup>5</sup> [35]. It has always been a highly variable object in all frequencies: for example, in the optical it varies within a range of about 3 magnitudes.

1ES1959+650 was the third BL Lac object from which TeV  $\gamma$ -ray emissions were detected. It was detected for the first time in the TeV regime by Telescope Array in 1999 [50]. In addition, also neutrino's events were detected spatially and temporally coincident with this flaring blazar [30].

Nevertheless, many questions on 1ES1959+650 are still open and under discussion. These concern its structure and emission mechanisms, what provokes flares states of different timescales and if it is an emitter of Ultra-High Energy Cosmic Rays and neutrinos. Long-term multi-wavelength (MWL) and multimessenger campaigns are needed for a better understanding of the source and, in general, on blazar objects properties, acceleration of particles and neutrinos' emission.

The aim of this work is to contribute in this framework, trying to better comprehend the

<sup>5</sup>The first X-ray observations of 1ES1959+650 were performed in the early '90s during the Einstein IPC Slew Survey; the first part of its name, 1ES, exactly refers to that observational campaign.

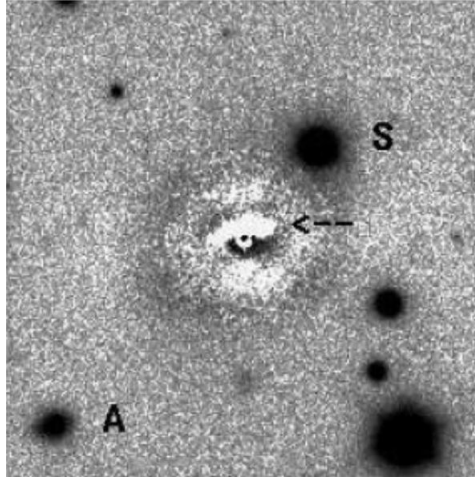


Figure 1.3: Nordic Optical Telescope (NOT) observation of the blazar 1ES1959+650 (it is pointed by the arrow in the picture) [32]. The blazar position in Galactic coordinates is (R.A.  $19^h 59^m 59.8^s$ ; dec.  $+65^\circ 08' 55''$ ) [58]. From the chart a *star-like* nucleus, surrounded by a nebulous halo, are clearly visible. The core corresponds with the central active Supermassive Black Hole.

VHE emission of 1ES1959+650 as detected by the forerunner of next CTA generation of telescopes, LST1.

The organization of the thesis is the following. In chapter 2 an overview on blazars and, in particular, on 1ES1959+650 is provided. Then, a chapter on the Large-Sized Telescope LST1 and its data analysis pipeline are presented in chapters 3 and 4. The former contains also brief descriptions of the telescopes used for the MWL characterization of the source.

The low-level stage data analysis of 1ES1959+650 observations from LST1 are reported in chapter 5. The scientific results of this work are presented in chapter 6, including MWL data analysis from the instruments in chapter 3. In the conclusion, chapter 7, final considerations about the results are drawn and possible scenarios are addressed to future research works.

# Chapter 2

## Blazars

Active Galactic Nuclei are highly luminous compact galaxies, fuelled by a central accreting Super-Massive Black Hole [64]. In figure 2.1 a scheme of the general AGNs' structure. The black hole at the centre is surrounded by an accretion disk, made up of a plasma; thus it is believed that the central engine provides the main powering mechanism. Penrose process [53] states that it is possible to extract energy from a spinning black hole at the price of losing rotational energy<sup>1</sup>.

The region containing rapidly moving clouds of gas that produces broad emission lines is likely above the disk [64]; it is also thought that the disk could contribute to the broad lines too. They produce strong optical and ultraviolet emission light. In the outer part of the accretion disk a thick dusty torus sometimes hides the broad lines emissions from the observer that has a transverse line of sight: continuum spectra or some broad-lines attributed to hot electrons scattering are usually observed. Optical/UV emission lines may also be obscured not only by the warped disk of dust but also by gases outside the accretion disk or the broad-line region. A hot corona could also be present above the accretion disk [40]: it may be responsible for the production of a continuum hard X-ray emission. A scheme of the hot corona is in figure 2.2. The narrow line clouds in figure 2.1 are farther from the central engine.

From the latter, one (or two symmetrical opposites<sup>2</sup>) relativistic jet outflows: it could extend up to the order of kpc [64]. Just to give a feeling about the size of those objects, the central super massive black hole has an estimated mass between  $10^4 - 10^{10} M_{\odot}$ . Considering an intermediate central black hole of  $10^8 M_{\odot}$ , thus a radius  $\sim 3 \cdot 10^{13}$  cm:

- the accretion disk extends between  $\sim 1 - 30 \cdot 10^{14}$  cm from the black hole event horizon edges
- the broad line region is at a distance  $\sim 2 - 20 \cdot 10^{16}$  cm from the system centre
- the dusty torus inner radius is probably at  $\sim 10^{17}$  cm
- the narrow-line zone between  $10^{18} - 10^{20}$  cm
- the observed radio jets extend up to  $10^{17} - 10^{24}$  cm far from the AGN centre

AGNs are empirically classified according to their radio-loudness and optical spectra, namely broad (Type 1), only narrow (Type 2), weak or unusual emission lines. Then, within each group, they are classified according to their luminosity, as showed in table 2.3. These properties depend on the AGN orientation with respect to the observer, i.e. the angle between

---

<sup>1</sup>The angular momentum and spinning properties about the AGNs' central black hole are not still clear and difficult to infer from the observations. One way could be to measure the  $K\alpha$  iron line: if it is close enough to the event horizon it could be broadened and asymmetric for black holes quickly spinning [13].

<sup>2</sup>It thought to be the case of Radio Loud objects.

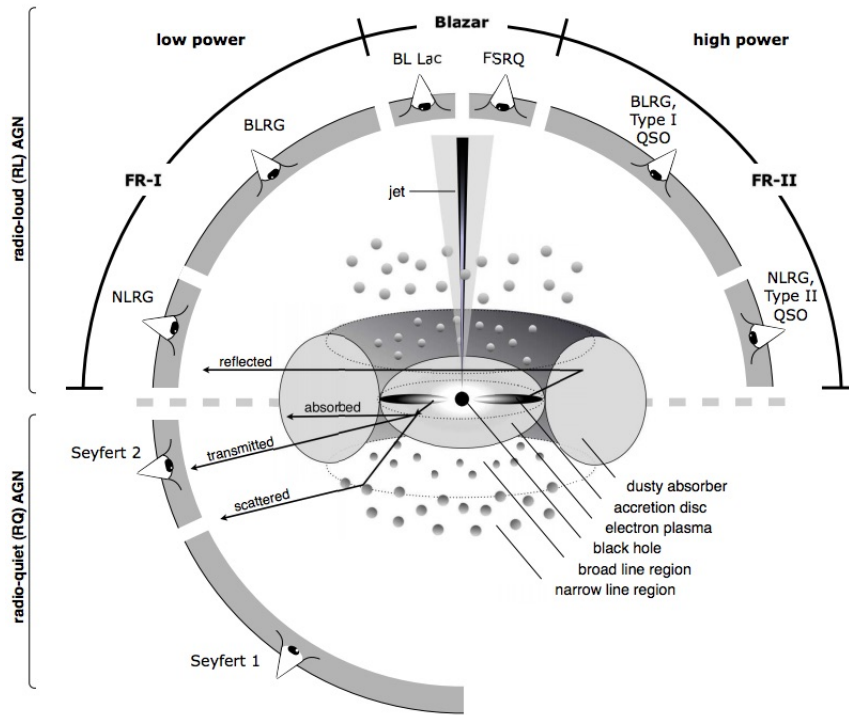


Figure 2.1: Active Galactic Nuclei schematic picture [13]. The various components are explained in the text: the arrows show how photons produced in the accretion disk could be either absorbed or processed by the external features. The circle surrounding AGN structure presents the standard classifications of these objects [64].

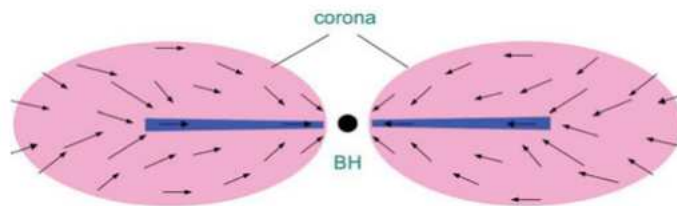


Figure 2.2: Hot corona and the accretion disk (*in blue*) transversal scheme: the arrows follows a possible mass flowing process between the two structures [40].

jet and line of sight (figure 2.1).

To pursue the thesis goals, the focus will be on **blazars**, a particular class of AGNs, for which the jet is oriented at small angle with respect to the observer line of sight. This results in strong relativistic Doppler beaming, described in appendix B.1.1.

From radio interferometry one-sided jets with apparent superluminal motion are often observed outflowing from the source centre, extending up to distances of the kpc order [18].

They emit photons throughout all the electromagnetic spectrum (from radio to Very High Energy  $\gamma$ -ray) and they are among the most violent and extreme sources of  $\gamma$ -ray emission in the Universe so far known, being such emission steady or recurrent. Blazars exhibit variability over a large range of timescales at all frequencies. For instance, in the high energies  $\gamma$ -ray band also less than one hour variability has been observed from some blazars.

The continuum spectra throughout all the wavelength is dominated by non-thermal emission: it is characterized by two humps, as in figure 2.4, one at low energy (located from radio to UV/X-ray) and the other at high energy (X-ray to  $\gamma$ -ray). The simplest model describing such a SED profile is treated in section 2.1. Blazars are on their turn classified in accordance to the peak frequencies and relative  $\nu F_\nu$  fluxes, related to the bolometric luminosities [26].

Indeed, orderly quoting, they are divided in loud Flat Spectrum Radio Quasars (FSQRs), low-

TABLE 1  
AGN Taxonomy  
Optical Emission Line Properties

		Type 2 (Narrow Line)	Type 1 (Broad Line)	Type 0 (Unusual)	
Radio Loudness	Radio-quiet:	Sy 2 NELG IR Quasar?	Sy 1  QSO	  BAL QSO?	Black Hole Spin?
	Radio-loud:	NLRG { FR I FR II	BLRG SSRQ FSRQ	Blazars { BL Lac Objects (FSRQ)	
		Decreasing angle to line of sight →			

Figure 2.3: Historical "Periodic Table of the AGN" from [64], i.e. the AGNs classification scheme. Radio-loudness characteristics could be due to host galaxy type or black hole spin. The three broad categories are based on their optical/UV spectral characteristics (Type 0 was a term invented in [64]: it is related to "close to 0° angle" objects.)

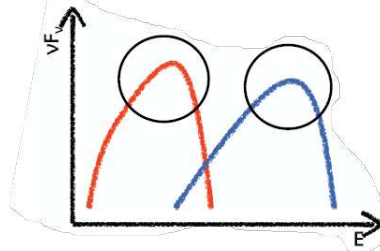


Figure 2.4: Simple scheme representing the usual profile of blazars non-thermal spectrum.

frequency peaked BL Lacs (LBLs) and high-frequency peaked BL Lac objects (HBLs). Starting from the first class (FSQR) an increasing of  $\nu F_\nu$  peak frequencies, a decreasing in the ratio  $\gamma$ -ray fluxes over low-frequency ones and in bolometric luminosity. It is the so called **blazar sequence**: in 2.5 the newest phenomenological model from [29].

Generally, the low energy peak of blazars' SEDs is attributed to synchrotron radiation from non-thermal, ultrarelativistic electrons in the jet [18]. The mechanisms behind the electrons' injection and acceleration are still topics under debate and investigation. However, many scenarios and models have been proposed during the years: impulsive injection at the jet base [20], isolated shocks perturbing the jet [60], internal shocks due to collisions between material shells [61], stochastic particle acceleration in the shear layers of the jet [56], magnetic reconnection in Poynting-flux dominated jets [59], or electrons' avalanches initiated by hadrons [36].

For a better understanding of this processes, source variability has to be taken into account too: it might be explained as a balance between injection/acceleration of ultrarelativistic electrons and the consequent radiative cooling [18]. In general, the parallel shocks acceleration of relativistic particles cause an electron injection spectra  $dN_e(E)/dE \propto E^{-q}$ , with  $2.2 \lesssim q \lesssim 2.3$  - the oblique shocks produce softer injections power law. The stochastic acceleration in resonance with plasma's turbulences behind the shock front causes the hardening of the injection spectral index.

One of the most credited picture presents a jet composed of a quick inner spine and a slower cocoon in the outer region [29]: in this framework the main particle acceleration mechanism occurs at the shear boundary layers. In this scenario the particle reaches an index  $q < 2$  and the high energy hump corresponds to the energy where the particle acceleration rate equals the energy loss one.

It is important to investigate on particle acceleration mechanisms at relativistic shocks, since

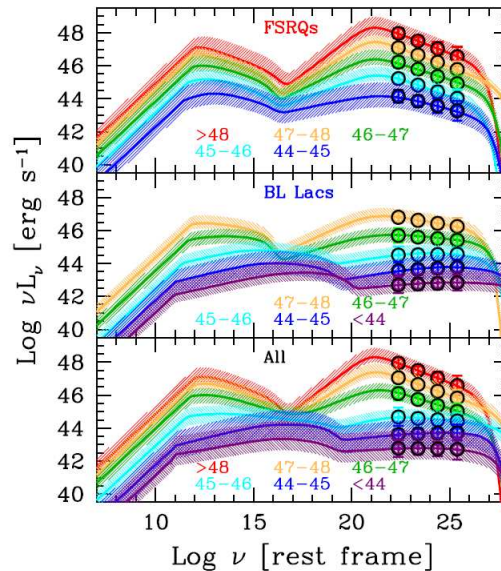


Figure 2.5: Phenomenological blazar sequence, obtained for different bins of  $\log(L_{\gamma\text{-ray}})$ , as in the coloured labels. (*top*) FSRQs, (*middle*) BL Lacs and (*bottom*) all sources, i.e. merging the two classes. [29]

the main goal is the understanding of the conversion of relativistic bulk kinetic energy into relativistic particles acceleration that, lastly, make over into radiation. In this context also the magnetic field in AGN environment plays a determinant role to evaluate the efficiencies of Fermi and stochastic particles acceleration process.

As the high energy emission concerns, two different approaches are proposed [18]. In the **leptonic** model, high energy photons are produced via inverse Compton scattering of ultrarelativistic electrons with photons<sup>3</sup> either produced by synchrotron inside the jet itself (Synchrotron-Self Compton, SSC) or external photons (external Compton, EC), likely coming from the accretion disk - also after being reprocessed by the near gaseous and dusty clouds. It might be the dominant process if protons in the jet are not so energetic to catalyze the  $p\gamma$  pion production.

On the contrary, if the kinetic energy of protons is high enough to reach  $p\gamma$  production threshold, as explained in appendix B.1.4, the **hadronic** model might explain blazars' high energy emissions [18]. A magnetic field of several tens of Gauss is required to accelerate protons towards the required energies. Indeed, the model takes into account synchrotron radiation of primary protons and the emission produced by secondary mesons and muons. Four electromagnetic cascade-types are generated: from  $\pi_0$ -decay and  $\pi^\pm$  (so from the secondary electrons produced), from  $p$ -synchrotron and from  $\mu^-$ ,  $\pi^-$  and  $K^-$  synchrotron emission. In this framework, the former two generate featureless  $\gamma$ -ray spectra, the latter two a double-humped ones. Synchrotron radiation field from protons and muons is generally responsible for the high-energy hump, while the low-energy one is attributed to primary and secondary  $e^-$ .

Most of FSRQs are explained with EC, LBLs are usually consistent with a mixture of SSC and EC, while HBLs' emission are compatible with SSC [18]. The sequence,  $HBL \rightarrow LBL \rightarrow FSRQ$ , as the increasing contribution of EC, may be due to the gradual depletion of the circumnuclear dust and gas. In any case the blazar sequence is not pending to one of the two scenarios: it is not a prediction from which probing the most reliable between the two.

In the reality, both models have to be taken into account to explain the observed emission. Some of the proposed hybrid models are, for instance, the so-called "supercritical" pile [36], hadronic synchrotron mirror [55] and one-zone model for a relativistic plasma whose constituents are protons and electrons [52].

<sup>3</sup>The inverse Compton process is explained in appendix B.1.3.

## 2.1 Phenomenology of Blazar spectra

The non-thermal SED of Blazars (sketch in figure 2.4) could be parametrized over the entire energy range by a simple function with humps and a flat radio spectrum [29]. It is a phenomenological description (see figure 2.6) of their emission that could diverge from the observation, especially in the optical/UV band in which the emission from the accretion disk, torus and the host galaxy (at low redshift) might deviate the spectrum from the simple model.

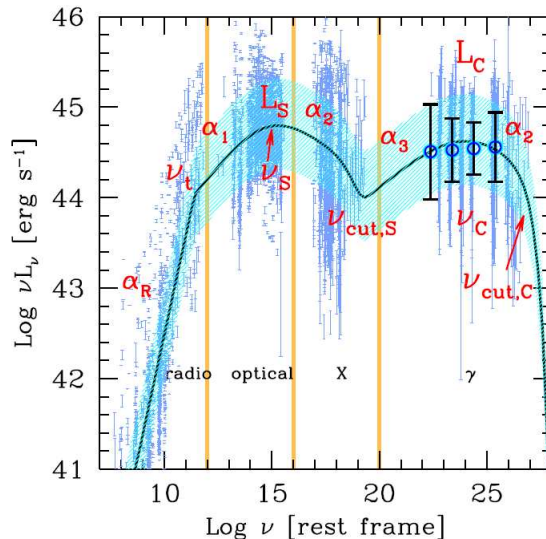


Figure 2.6: Phenomenological SED blazar model: it is showed the BL Lacs averaged SED in  $45 < \log(L_\gamma \text{erg}^{-1} \text{s}^{-1}) < 46$ , the data are from each source analysed in [29]. The hatched stripes correspond to  $1 \sigma$  dispersion around the fitting function (black line). In red the parameters of the entire broad band function introduced in the text.

In the radio a simple power law:

$$L_R(\nu) = A\nu^{-\alpha_R} \quad \nu \leq \nu_t \quad (2.1)$$

connects to a smoothly broken power law describing the two-humps.

$$L_{S+C}(\nu) = L_S(\nu) + L_C(\nu) \quad \nu > \nu_t \quad (2.2)$$

$\nu_t$  is the frequency at which the flat part ends, interpreted as self-absorption frequency of the jet core region. The low-energy hump is modelled as:

$$L_S = B \frac{(\nu/\nu_S)^{-\alpha_1}}{1 + (\nu/\nu_S)^{-\alpha_1 + \alpha_2}} \exp(-\nu/\nu_{\text{cut},S}) \quad (2.3)$$

while the high energy part as:

$$L_C = C \frac{(\nu/\nu_C)^{-\alpha_3}}{1 + (\nu/\nu_C)^{-\alpha_3 + \alpha_2}} \exp(-\nu/\nu_{\text{cut},C}) \quad (2.4)$$

The constraints to the normalization factors (A, B and C) are:

- Equations 2.1 and 2.2 are connected at  $\nu_t$
- $\nu_S$  is the synchrotron spectrum peak at which the luminosity is  $L_S(\nu_S)$
- at the peak of inverse Compton,  $\nu_C$ , the luminosity is  $L_C(\nu_C)$  - parametrized giving the Compton dominance, i.e. ratio of  $\nu L_\nu$  inverse Compton and synchrotron luminosities.

The 11 parameters that appear in the broad wavelength model are:

- 3 typical frequencies (already explained)
- 2 cut-off frequencies  $\nu_{cut,S}$  and  $\nu_{cut,C}$
- 4 spectral indexes:  $\alpha_R$  for 2.1,  $\alpha_1$  that links  $\nu_t$  and  $\nu_S$ ,  $\alpha_2$  slope after the low-energy peak and after high-energy one<sup>4</sup>,  $\alpha_3$  slope before the high-energy peak.
- $L_S(\nu_S)$  and  $L_C(\nu_C)$  in correspondence of the two peaks.

## 2.2 High-Peaked BL Lac objects

1ES1959+650 is a HBL. To introduce the thesis target source the discussion compass moves to HBLs. Such objects have a frequency of the synchrotron peak between  $10^{15}$  and  $10^{17}$  Hz. Exceeding the upper threshold, an object is classified as extreme-HBL, the least luminous blazar class. On the other hand, below  $10^{15}$  Hz, the intermediate peaked BL Lacs are in the middle between LBLs and HBLs.

In the leptonic framework, HBLs require very high electrons energies and relatively low magnetic fields [18]. However, HBLs' spectra are, in the majority of the cases, in agreement with p-synchrotron blazar model. The synchrotron primary photon energy density is small: it consistently explains the low bolometric luminosity observed.

### 2.2.1 Past investigations on 1ES1959+650

The object analysed in this work has been really crucial in the developing of some TeV emission models. Two of the most relevant studies of this blazar were carried during the 2002 and 2016 episodes of flaring state.

The "orphan" TeV flare observed in May 2002 by Whipple 10m Cherenkov telescope has been a benchmark in this context [38]. "Orphan" since the flare detected in TeV did not spot a flaring X-ray counterpart<sup>5</sup>. The "orphan" flare in TeV was preceded by a simultaneous X/ $\gamma$ -ray flare, commonly associated to leptonic SSC models.

The isolated TeV flare is understood taking into account hadronic processes [38]. In particular, the **hadronic synchrotron mirror** model has been developed to understand this phenomenon: a geometrical scheme of the process is in 2.7. A blob made of ultrarelativistic electrons and relativistic protons travels along the jet: the particles are firstly accelerated in F1, a region close to the BL Lac core. It gives rise to the primary simultaneous synchrotron/TeV flare through SSC leptonic process. Jet internal shocks and other acceleration mechanisms sustain particle acceleration producing the observed quiescent emission state (UV/X-ray synchrotron radiation). A fraction of the radiation is reflected by a gas cloud placed at a distance  $R_m$  from the core; the cloud has a certain reprocessing depth  $\tau_m$ . The second flare is consequently produced by the  $p\gamma$  interaction between relativistic protons in the moving blob and the re-entering reflected radiation fraction. The time delay between F1 and F2 is  $\Delta t_{obs} \approx \frac{R_m}{2\Gamma^2 c}$  ( $\Gamma$  is the Lorentz factor,  $c$  vacuum light speed). Given the typical reflecting gaseous cloud radial extension and density, the duration of the secondary flare is expected as  $\omega_{fl}^{obs} \sim 1.2\Gamma_1^{-2}h$ ; it is consistent with the May 2002 1ES1959+650 light curve [38].

Computing some of this mechanism relevant quantities (co-moving synchrotron and reflected radiation fluxes and the co-moving luminosity due to  $p\gamma$  interaction<sup>6</sup>), one infers that TeV "orphan" flares require very extreme conditions: for this reason they are highly rare.

<sup>4</sup>In the Klein-Nishina regime, the synchrotron slope after the first peak is not equal to the one after the high-energy maximum value. It is relevant in blazars detected in TeV regime.

<sup>5</sup>A similar "orphan TeV flare" was also detected in Mrk 421 in the period 2003-2004 [17].

<sup>6</sup>From this co-moving luminosity the peak flux is estimated as  $\nu F_\nu(VHE) \sim \frac{L'_{VHE}\Gamma^4}{4\pi d_L^2}$

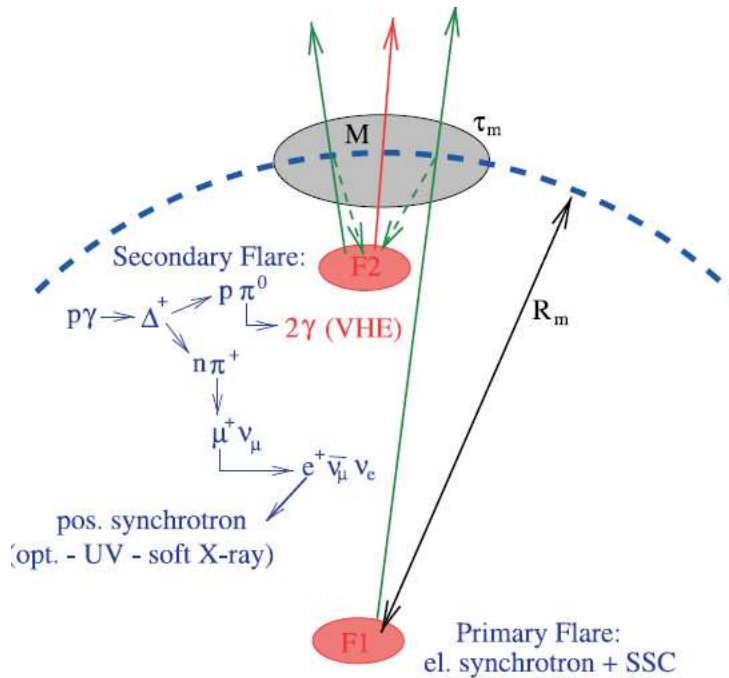


Figure 2.7: Hadronic synchrotron mirror model sketch [18]. The primary flare is generated in F1 near the object core. The synchrotron emission is then reflected by the mirror (M) at a distance  $R_m$ , re-entering in the jet region. Reflected photons are then the primary responsible for the hadronic-dominated secondary flare in a region near to the mirror (F2).

In 2016 - from May to July - increasing fluxes in X-ray and  $\gamma$ -ray till TeV band were detected by *Swift*-XRT/-BAT, Fermi-LAT and MAGIC ([44] and [51]). A long-term Multiwavelength campaign monitored 1ES1959+650 in that period. In particular, a correlation without lags was found between X-ray and VHE  $\gamma$ -ray flux.

The most extreme flaring episodes, with a flux  $>300$  GeV reaching 2.5-3 times Crab Nebula one, were registered in three days, 13<sup>th</sup> and 14<sup>th</sup> of June, 1<sup>st</sup> of July 2016. Intra-night fast variability was also observed during those days. In [44] one-zone leptonic in figure B.5, hadronic in B.6 and lepto-hadronic in B.7 models were tested during the flare states. The parameters obtained from SSC model (leptonic scenario) indicate an Extreme HBL state during the flare period: the two peaks move to higher energies showing a "bluer when brighter" trend (look at figure B.8). The two-zones model was investigated for some periods of 2016 flare states, as shown in figure B.9 [44]. The two-zones SSC model tested in [44] assumes two comoving blobs, having the same Doppler factor, but of different sizes. Magnetic field and electron energy density of the inner region were an order of magnitude higher than the outer. In addition, the inner electron spectra were found softer than the outer.

Important changes were found in electron density of two-zones SSC during the flare evolution, while the magnetic field parameter did not vary so much [44]. The former can be explained as either new particle population injection or re-acceleration mechanism. The narrow electron energy distribution inferred from the analysis could be a hint of Fermi II order acceleration, where Alfvén stochastic moving waves may be responsible for the acceleration.

Cross-checking the power law indexes in different energy bands, different emission regions can be inferred. Indeed, no consistent correlations were spotted between optical/UV fluxes and other energy bands. On the one hand, a "softer when brighter" behaviour is seen for the spectral index evolution in the  $\gamma$ -ray band covered by Fermi, especially when the source is not very active [51]. On the other hand, X-ray observations show a "harder when brighter trend".

Studies on 1ES1959+650 during these two interesting periods have been presented so far. It is

a way to stress the importance of monitoring this source, why it is scientifically relevant. It is also an introduction to the most recent analysis in VHE presented in this thesis. Models and explanations of the past are a key to interpret current observation and show the way for new analysis.

# Chapter 3

## Large-Sized Telescope LST1 and lower frequencies telescopes

LST1, in figure 3.1, is the first Large-Sized Telescope of CTA [45]. It is situated at Roque de los Muchachos Observatory (ORM) at an altitude above the sea level of 2200 m, in La Palma (Canary Islands, Spain). The site's geographic coordinate are (28°N, 18°W). The ORM is the location site of CTA-North and it also hosts MAGIC I-II Cherenkov telescopes.

The LST collaboration, consisting on more than 300 scientists and engineers from about 30 institutes all over the world, started the design of LST1 in 2006 [45]. LST1 was built from 2016 to 2018 (inaguration date October 2018) as a CTA prototype telescope. The first observation took place in December 2018 and it is quite regularly observing the sky since December 2019. In 2020 the pandemic situation produced some slowdowns in the data acquisition; as well as in 2021 (from mid-September to mid-December) the eruption of Cumbre Vieja volcano in La Palma caused the stop of observations from September 2021 to January 2022. The collaboration resumed the operations after concluding that the eruption did not affect significantly the instrument's performance.

### 3.1 LST1 characteristics

LST1 has been designed in order to satisfy two main performance requirements: a fast repositioning to react to transient phenomena and a high sensitivity at energies below 300 GeV. The former desired performance is useful for Gamma Ray Bursts observation.

To accomplish the declared scopes, the total moving weight of the telescope is around 100 tons (rail excluded) and the fast-rotating power system is based on 2x300kW VYCON FlyWheels. The parabolic reflecting dish is supported by a structure of carbon fiber and steel tubes [45]. The total surface is about 400  $m^2$ , made up of 198 mirrors, with an independent Active Mirror Control system. These systems are important to compensate for small dish deformations at different zenith angles.

Cherenkov photons collected by the dish are focused into the Camera (showed in figure 3.2) that has 1855 photo-sensors. Each photo-sensor converts light in electric signal, which in turn is processed by the dedicated readout electronics.

The field of view of the LST1 camera is of 4.5°; it has pixeles which incorporate the light guides, photo-sensors and the readout electronics<sup>1</sup>.

The Camera has a trigger based on the shower topology and the temporal development of the Cherenkov signal. A dedicated algorithm processes the signal in order to find light flashes of  $\sim$ ns duration [45]. In addition, LST Cameras have an on-line trigger connection among the

---

<sup>1</sup>Electronic that relies on DRS (Domino Ring Sampler) chip, the same used in MAGIC telescopes [12].



Figure 3.1: Large-Sized Telescope LST1 in ORM. In the background (*right*), MAGIC-II Cherenkov telescope.



Figure 3.2: In the foreground, LST1 Camera [28].

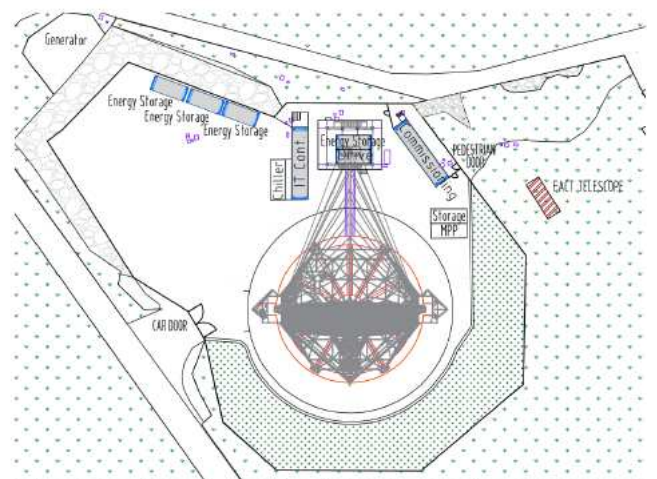


Figure 3.3: LST1 and the nearby infrastructure in Roque de Los Muchachos Observatory [45].

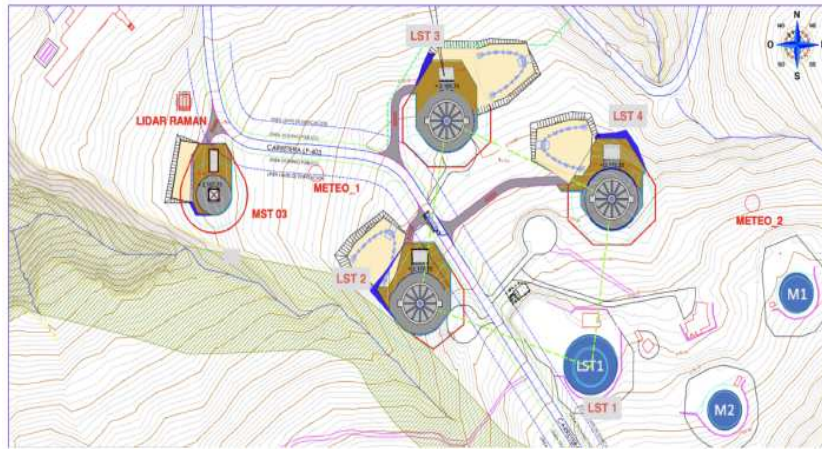


Figure 3.4: CTA North site maps: in red the telescopes that will be built in the next years [45].

telescopes to operate stereoscopically at hardware level, improving the rejection of accidental triggers by a factor close to 100.

**LST1 infrastructures and data network** LST1 exploits the existing infrastructure of ORM (roads, electricity, connection, residence, ...).

Moreover, a CTA installation in ORM is the data center, IT Cluster<sup>2</sup>. It has 2000 cores, 3.4 PB of disk storage space and a SLURM batch job system. This IT cluster is used by LST members to run data processing pipelines and implement analysis methods, exploiting the data acquired by the telescope and Monte Carlo (MC) simulations. Data are also copied to PIC in Barcelona and CNAF in Bologna as backup.

A container was installed for the telescope onsite commissioning<sup>3</sup> and technical interventions, together with two foot storage containers (in figure 3.3).

Three energy storage containers have already been placed in the nearby of LST1: they will be used for the next LST2-4 telescopes.

## 3.2 Cherenkov Telescope Array North perspectives

The funding for LST2-4 constructions in CTA North site have already been allocated. The scheme depicting the positions of the four Large-Sized telescopes is in figure 3.4. The north hemisphere array will focus on low-/mid- energy ranges 20-5000 GeV, implying a stronger emphasis in extragalactic sources observation. Indeed, 9 further Medium-size telescopes (MSTs) are planned to be installed (see figure 3.5).

Each MST has a primary reflecting mirror with diameter of 12 m (collecting surface, including shadowing,  $88 m^2$ ) and a focal length of 16 m [28]. MSTs achieve their full sensitivity performance in the range between 150 GeV and 5 TeV, but it can detect  $\gamma$ -rays both at lower and higher energies. The Camera collecting photons is a NectarCAM, composed of 256 modules, each one containing seven photo-detectors. MSTs have  $7/8$  degrees field of view. The area covered by the CTA Observatory Northern Array is of about  $\sim 0.25 km^2$  in the chosen "Alpha Configuration"<sup>4</sup>.

To show the scientific payload of CTA Northern Observatory, in the plot 3.6 the sensitivity curves of CTA North site, 50 and 5 hours of exposure. MAGIC sensitivity curves are also

<sup>2</sup>It has been installed and it is operative thanks to University of Tokyo.

<sup>3</sup>During COVID-19 pandemic in 2020 several remote operation locations have been installed.

<sup>4</sup>It is the approved layout defining the geographical position of the telescopes, calibration systems and devices that characterize the atmospheric conditions. This layout has been to achieve the best observations performances [28].

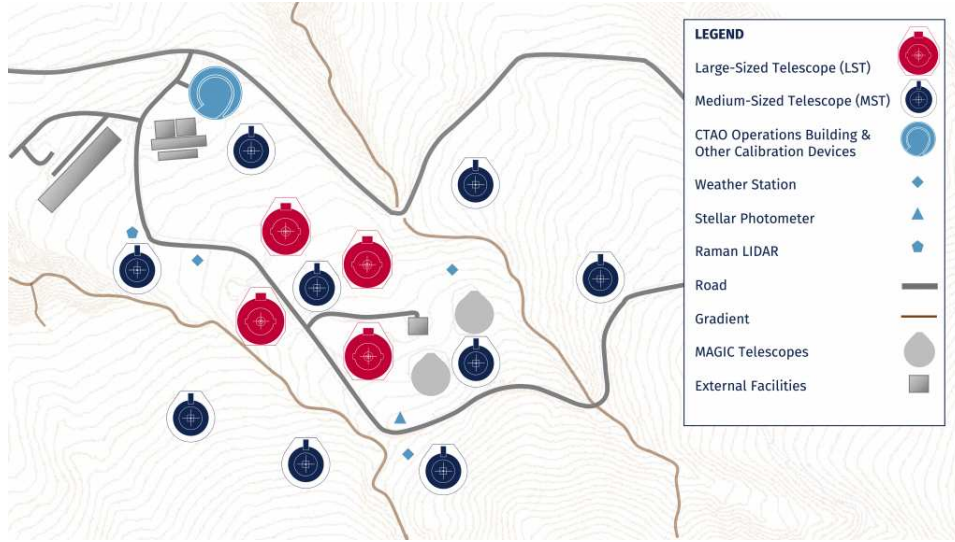


Figure 3.5: Northern CTA Observatory array project in "Alpha Configuration" [28].

shown for comparison. The extrapolated spectrum from Fermi-LAT observations' analysis of 1ES1959+650 is superimposed.

### 3.3 Overview on other instruments

During the thesis document the reader will come across observations of 1ES1959+650 performed by instruments that detect lower energies photons than LST1. In this section a brief overview on them is provided.

#### 3.3.1 Fermi-LAT in $\gamma$ -rays

The Fermi Gamma-ray Space Telescope (in figure 3.7) is an international space mission studying the sky in the energy band from 10 keV to 300 GeV [47]. Its main instrument is the Large Area Telescope: it exploits the phenomenon of pair conversion. The interaction of the primary photon - in the energy range between 20 MeV and 300 GeV - with the instrument produces a  $e^-e^+$  pair: the energy and trajectory of the collected pair determines the reconstructed energy and direction of the incident  $\gamma$ -ray. The modular LAT baseline is made up of  $4 \times 4$  array of identical towers, each consisting of a tracker, a calorimeter and a data acquisition module.

The incident photons pass through an anticoincidence shield (it detects charged cosmic rays) and then through the conversion foils - thin layers of high-Z materials, as showed in the scheme 3.8. Once converted in pairs, the trajectories are measured by trackers (18 layers of silicon strip detectors) and the energy of the pairs measured in a calorimeter (8 layers of 12 CsI bars). A  $\gamma$ -ray signature can be discerned if there is no signal in the shield, if there are more tracks starting from the same position in the tracker volume and if there is an electromagnetic shower in the calorimeter.

Fermi-LAT explores the most extreme environments in the Universe; it also plays a determinant role in the AGNs studies and the observations of their High Energy (HE)  $\gamma$ -ray emission. LAT observes  $\gamma$ -rays from 20 MeV to 300 GeV: the 57% of all sources detected by Fermi-LAT are blazars. The fourth LAT AGN catalog contains more than 3200 sources emitting  $\gamma$ -rays associated to AGNs [10]. Angular resolution of Fermi-LAT is comparatively worse than optical, X-ray or radio catalogs, but the majority of those  $\gamma$ -ray sources are associated with high confidence to an AGN.

Thanks to the fact that Fermi scans continuously the sky, it is very useful to monitor the

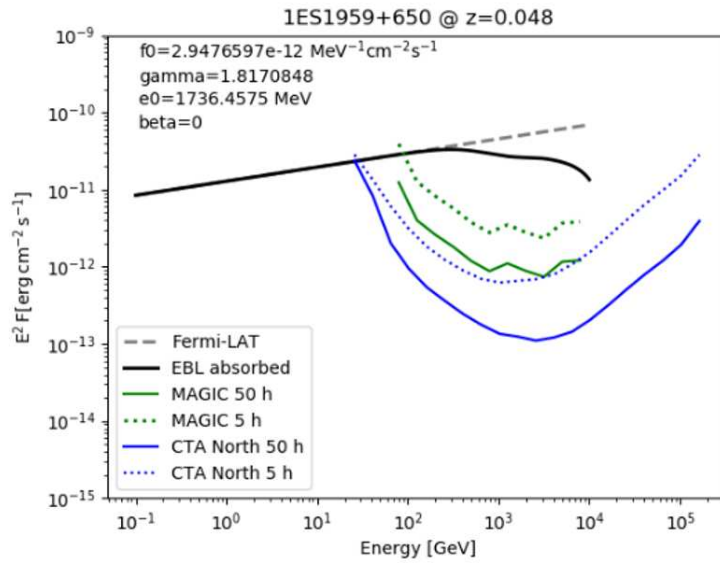


Figure 3.6: MAGIC and CTA North sensitivity curves and the extrapolated 1ES1959+650 spectral flux from parameters inferred by Fermi-LAT analysis (*on the top*), taking into account Extra-Galactic Background Light absorption (*black line*).

(*The graphic has been produced during the classes held by Prof. Josefa Becerra González of the course Astrofísica de Altas Energías y Astropartículas, ULL, Tenerife, Spain.*)



Figure 3.7: Fermi mission pictorial image [47].

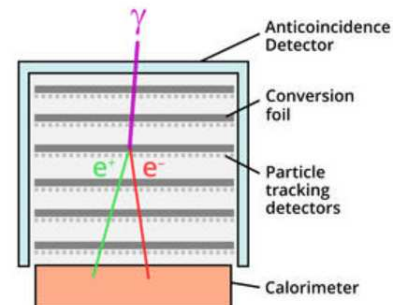
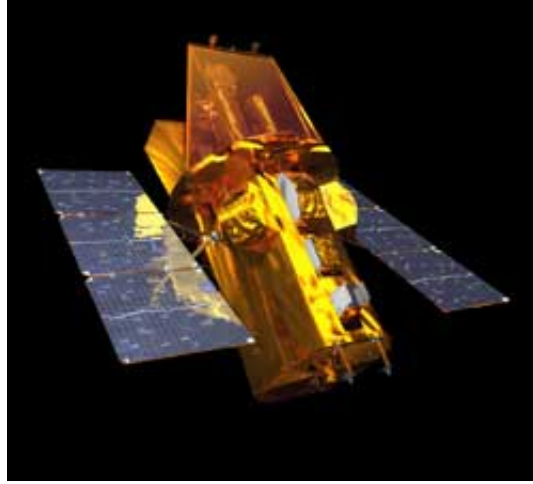


Figure 3.8: Transverse section of LAT. *Credits: NASA's Goddard Space Flight Center*

Figure 3.9: *Swift* observatory [48].

variability of AGNs<sup>5</sup>.

### 3.3.2 *Swift*-XRT in X-rays

*Swift* is a multiwavelength space observatory (look at figure 3.9) mainly dedicated to the observation and investigation of Gamma-Ray Bursts [48]. The three instruments are the Burst Alert Telescope (BAT, 15 - 150 keV), X-ray Telescope (XRT, 0.3 - 10 keV) and UV/Optical Telescope (UVOT, 170 - 600 nm).

XRT has an effective area of  $110 \text{ cm}^2$ , a  $23.6 \times 23.6$  arcmin FoV and 18 arcsec resolution. It is designed to focus X-rays with a grazing incidence Wolter 1 telescope onto state of art CCDs. The latter has an image area of  $600 \times 602$  pixels, the same size of the storage region.

The instrument is provided of three readout systems: Imaging Mode, Photon-counting Mode (for dim sources) and Windowed Timing Mode (for bright sources) [48]. The former produces an image obtained by the integration of the total energy deposited in each pixel: it is used to infer the position of the sources. The latter permits spectral and spatial measurements. The obtained fluxes from the source range from  $2 \cdot 10^{-14}$  to  $9 \cdot 10^{-10} \text{ erg} \cdot \text{cm}^{-2} \text{ s}^{-1}$  (sensitivity limits).

### 3.3.3 TELAMON program in radio

Radio observations showed in the last box of figure 6.39 were performed by the Effelsberg 100-m telescope (located in Effelsberg, Germany, operated by Max-Planck Institute for Radio Astronomy in Bonn, see picture 3.10). It is used to observe radio emission from 3.5 mm (90 GHz) to 90 cm (300 MHz) with a good angular resolution, high sensitivity and several receivers in the two focus [34].

The data provided in this thesis, are part of TELAMON (TeV Effelsberg Long-Term AGN Monitoring) program. TELAMON's aim is to monitor TeV-blazars and candidate neutrino emitter AGNs in the radio band with the Effelsberg telescope since August 2020. Since bright low-peaked blazars are also included, the program selection criteria is to include all-sources that have a low-state flux density below 500 mJy. The 14 mm and 20 mm receivers are used in continuum observing mode. The latter receiver was added only in spring 2021. To obtain the flux points, data has been fitted by a powerlaw with specific constraints on the spectral index [24]. The average flux density is computed as:

$$\bar{S} = \frac{\int_{\nu_1}^{\nu_2} S(\nu) d\nu}{\nu_2 - \nu_1} \quad (3.1)$$

<sup>5</sup>Since the instantaneous variability is limited variability can be measurable with high confidence level either in long integrations or for bright blazars.

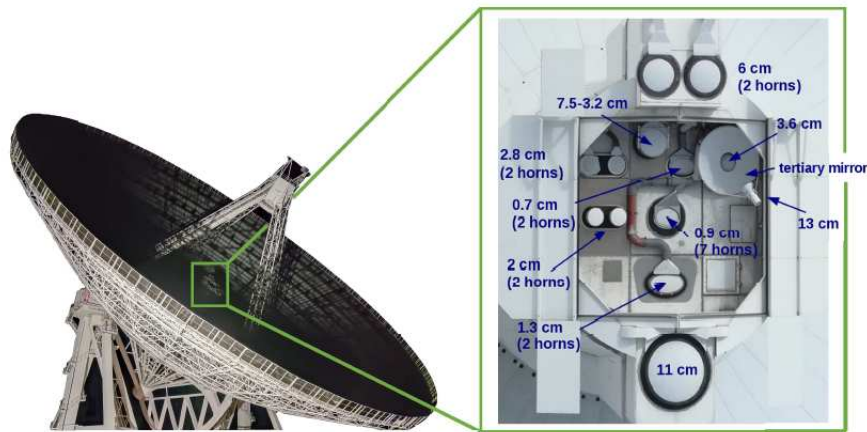


Figure 3.10: (left) Effelsberg 100-m telescope (Germany). (right) Zoom on the secondary receiver cabin. For example, the receiver at 14 mm is 1.3 cm in the picture [34]

For the 14 mm average points the boundary frequencies are  $\nu_1 = 19$  GHz and  $\nu_2 = 25$  GHz, whereas for the 20 mm the range is from 13 GHz to 18 GHz. In the averaged light curve representation, it is much easier to examine the source variability and identify flares.

As reported in [24], one of the approaches to the variability studies is the Likelihood computation to the Intrinsic Modulation Index (the ratio between the intrinsic standard deviation and the intrinsic mean flux density of the source).

# Chapter 4

## LST1 data analysis pipeline

The aim of this chapter is to introduce the reader to the LST1 data analysis procedures, methodologies and data flow, starting from the low analysis steps (trace integration, image cleaning, shower parametrization etc.) up to to the high level analysis (source detection, flux estimation etc.). A strong emphasize will be addressed to the Higher Analysis stages, the main goal of this paper, the ones in which scientific speculation and results are produced<sup>1</sup>. The full list of LST1 data levels is:

- R0: raw data written to the disk consisting of two gain channels and only roughly pre-calibrated for the DRS4 baseline offsets.
- R1: once applied all the specific calibration steps, with a single time series for each pixel and in photo electrons units.
- DL0: same as R1 but with a data volume reduction, namely without pixels that do not contain Cherenkov signal.
- DL1a: "Image Level", it is obtained by integrating pixel traces and measuring the mean arrival time for each pixel.
- DL1b: parametrization of DL1a image of Cherenkov shower image, to estimate the properties of the events.
- DL2: the arrival direction is determined and energy of the event is estimated using machine learning (ML) methods. It is also estimated the *gammaness*, a quantity that defines the likelihoodness of the event being a  $\gamma$ -ray shower.
- DL3: Instrument Response Functions (IRFs), coming from MC simulated showers are incorporated to data.
- post-DL3: scientific results are produced, such as fluxes, spectra, light curves.

### 4.1 Tools and Software

**ctape & lstchain framework** The analysis library employed for the LST1 data (observed and simulated) in the low level stage is `cta-lstchain` [7], strongly based on `ctape` [6]. It contains all the tools for data processing from R0 up to DL3 stage.

`ctape_io_lst` is the plugin used to read LST data and convert it to a format compatible to `ctape` itself.

---

<sup>1</sup>Most of the information contained in this chapter has been explained during the LST data analysis on-line School of January 2022 [46]. It was held by many researchers involved in the development of the LST1 data analysis software.

`ctapipe` is a framework for prototyping the low-level data processing algorithms for CTA. It is made up of various scientific `Python` components and libraries (`Gammapy`, `Astropy`, `Scipy`, `Numpy`, `Matplotlib`, ...) and it provides common Application Programming Interface (API) and user packaging. Its algorithms, functions and classes are mainly written in `Python`; however, they can also be in `C` or `C++` (then they are read by `ctapipe` through dedicated wrappers).

The pipeline tools developed to analyze LST data are, then, performed in some releases and deployments in `conda` virtual environment and package. In this location, all the dependencies and compilers/interpreters are contained.

Inside `ctapipe` there are specific functions that:

- Read simulation files: each telescope has its wrapper to read the data in this framework
- Perform calibration, cleaning and properties extraction
- Plot of Camera and Array
- Define and transform coordinate frames
- Stereo reconstruction <sup>2</sup>

`cta-lstchain` is an Open Source Software (under the MIT licence). It is a wrapper, i.e. collection of code/classes/methods, to allow for monoscopic data reconstruction with LST1. The LST workflow exploits the following `lstchain` scripts to pass from one stage to another.

- From R0 to DL1
  - `lstchain_data_r0_to_dl1`
  - `lstchain_mc_r0_to_dl1`
- From DL1 to DL2
  - `lstchain_dl1_to_dl2`
- From DL2 to DL3
  - `lstchain_create_dl3_file`
  - `lstchain_create_dl3_index_files`
  - `lstchain_create_irf_files`

`lstchain` contains further tools and functions specific for the LST1 analysis. In particular, they are for:

- Low and high calibration
- PSF smearing
- NSB tuner
- Dynamic cleaning
- DL1 datacheck
- Source-dependent analysis

In addition other dedicated scripts for the file merging, computation of sensitivity and visualization methods are provided.

---

<sup>2</sup>In the case of LST1 analysis it is developed a single telescope reconstruction in `cta-lstchain`, since so far in ORM only one LST telescope has been built.

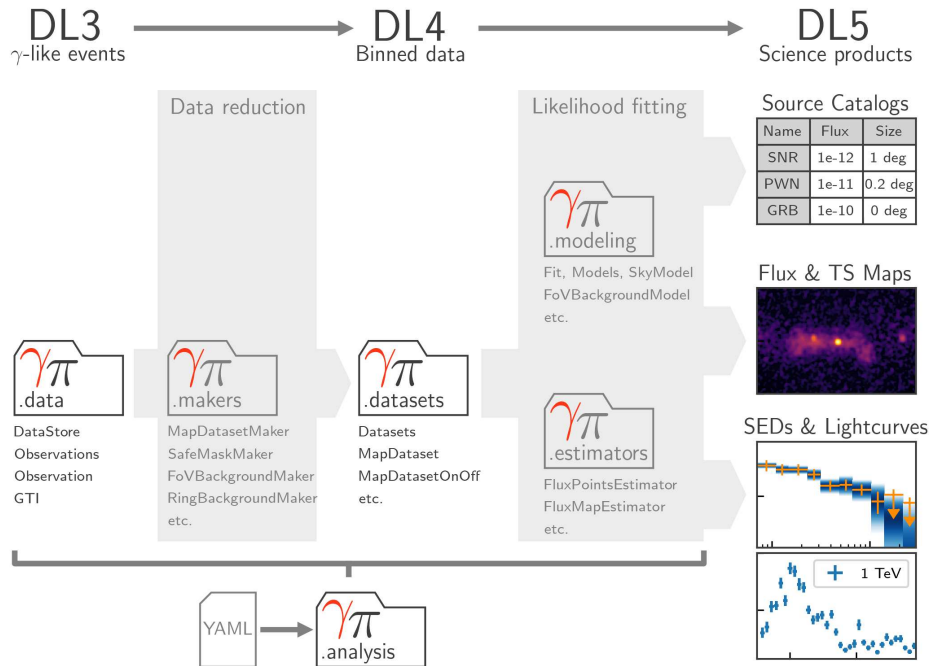


Figure 4.1: Scheme on the higher level analysis workflow [23].

**Gammapy Tools** For the higher level analysis, whose aim is to make scientific products (Light Curves, Spectral Energy Distribution, etc.), Gammapy package [19] [23] is used. It is an open-source Python library built on Numpy, Scipy and Astropy. It is devoted to gamma-ray astronomy analysis and it is the core and official Tools library of CTA, largely used in MAGIC, VERITAS and HAWC and recommended by the H.E.S.S. collaboration as the package for science publication. The latest version is Gammapy v0.20.1.

Gammapy data flow for IACT telescopes starts from the DL3 files, which include a list of events and a full description of the IRFs. DL3 files can be binned, resulting in DL4 products. Finally DL5 science products are obtained by performing a Likelihood fit on the DL4 binned data. The mentioned flow is illustrated with the Gammapy sub-packages in figure 4.1. How the sub-packages work and the data reduction steps are explained in section 4.5. Figure 4.1 gives a general idea of the Gammapy structure. In general, Gammapy can be used with the configuration high level analysis API or as a standard Python library.

## 4.2 From waveforms to direction and energy reconstruction

**Pixel calibration** Camera PMTs' signals are digitized waveforms: these constitute for each pixel the raw data (R0) from the LST camera. One R0 data stream corresponds to 40 samples of 1 ns duration per channel (it is connected to the frequency reading). The signals are amplified in two gain channels, in which the higher channel is  $\times 17$  the lower one (see figure 4.2) [46]. The amplified signals are stored in  $\sim 4000$  capacitors (4 DRS4 rings of 1024 capacitors) acting as buffers. They are sampled at a frequency of  $\sim 1$  GHz, one signal is composed of 40 capacitors per pixel, per trigger, per channel. The LST R0 data is stored as a `zfits` file [27].

DRS4's systematic effects have to be taken into account, especially during pixel calibration. They are based on **Flat-field events** (FF), events recorded when the Camera is illuminated by Calibox<sup>3</sup>. FF events are used to correct for pixel-to-pixel gain differences, so that the signal

<sup>3</sup>It uniformly illuminates the Camera with the diffuse laser light ( $\lambda = 355\text{nm}$ ) provided by two filters to modulate the signal.

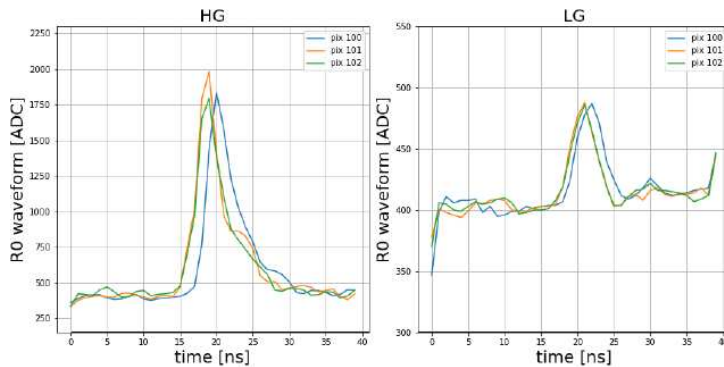


Figure 4.2: High (*right*) and low gain waveform signals (*left*) [46].

recorded by each PMT is offsetted<sup>4</sup>. **Pedestal events** are obtained during random triggers of the Camera without external illumination. Through them, pedestal charges in each pixel are evaluated.

Data useful for the calibration are taken with dark pedestal run, FF combined with pedestal runs (containing the Night Sky Background, NSB), FF and pedestal interleaved events, FF intensity scans.

Further corrections on the readout of the DRS4 are obtained by:

1. Discarding the border samples, so  $R1\_waveform = R0\_waveform[1 : 37]$
2. Correcting the different baseline value of each capacitor
3. Subtracting the delay from the last reading of each capacitor.
4. Subtracting the predictable spikes estimated in the dark pedestal run.
5. Correcting the arrival time of the pulse, with estimation coming from FF events (time delays in optical fibers and the pulse reading).

A fundamental step to pass to the R1 data is the pixel calibration [46]. It is the procedure to translate the waveforms from ADC counts to flat-field photon-electron units. As a matter of fact:

$$R1\_waveform\_in\_pe = (waveform(ADC) - pedestal(ADC)) \cdot gain$$

The pulse time is corrected as:

$$R1\_pulse\_time = peak\_charge\_time - FF\_time\_correction$$

Two level of calibration are executed. The real time one (level A) is computed processing a dedicated pedestal calibration (pedcal) run at the beginning of the night<sup>5</sup>. To remark is the fact that in the FF signal one has to take into account the gain of the detector and a quadratic noise term<sup>6</sup>. The Offline calibration (level B) is estimated through interleaved pedestal and FF events, acquired during the data taking.

Lastly, to extract the time and pointing information the `lstchain` functions *EventTimeCalculator* and *PointingSource* are used [46].

<sup>4</sup>It is also to avoid negative fluctuations during readout.

<sup>5</sup>To produce level A calibration coefficients, calibration onsite scripts are exploited. The latter are based on `ctapipe Tools` and on calibration data tree; they also have some arguments, some of them mandatory. For instance, `onsite_create_drs4_pedestal_file` and `onsite_create_drs4_time_file` produce daily respectively the baseline and time corrections. `onsite_create_calibration_file` produces daily the waveform calibration and flatfielding.

<sup>6</sup>It contains laser fluctuation and not uniform DRS4 sampling. It is produced by `onsite_create_ffactor_systematic_file` performing the fit of the filter scan data acquired each month.

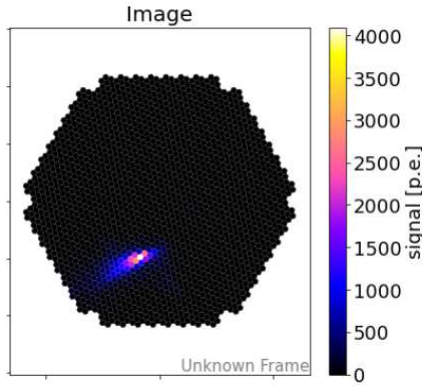


Figure 4.3: Cleaned camera image: only pixels passing cleaning cuts survive [46].

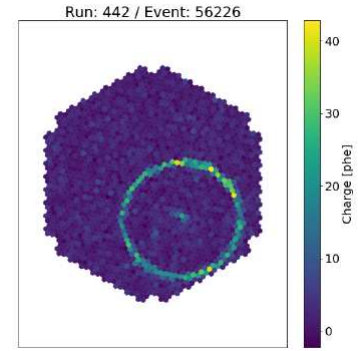


Figure 4.4: Ring produced in the Camera by the Cherenkov light emitted by a muon [46].

**R0 to DL1a** In order to obtain the DL1a data, the waveforms are integrated around the peak and the *peak time* has to be determined. To achieve the two purposes, the *LocalPeakWindowSum* *ctapipe* function is utilized [46].

**DL1a to DL1b** In this phase, the aim is to keep only the pixels containing the signal of the cosmic shower. To clean the image two functions are imported from `ctapipe.image.cleaning`: `tailcut_clean` and `apply_time_delta_cleaning` [46]. The former is a charge cleaning by selecting the pixels of interests. Two thresholds depending on the amount of photo electron signal are set: one for the core picture and the other for the boundary pixels<sup>7</sup>.

The latter function removes pixels that have less than a determined number of neighbors that arrive within a given time<sup>8</sup>.

However it is possible that bright *fake islands* in the camera picture are still *alive*, spoiling image parametrization and arising issues in the agreement between MC and real data. They are consequent to either fluctuations of NSB or secondary part of the image in hadronic showers or misaligned mirrors in the parabolic dish. To face those systematics in the camera image a **dynamic cleaning** is applied. As the name suggests, it is not a fixed cut, but it removes all the pixels below a certain fraction of the brightest pixel of the image: it is shown in figure 4.3. The reference maximum charge value is usually taken as the average of the three brightest pixels. It is a useful cut only for bright events, for the dimmer ones the dynamic cleaning does not affect the image.

**Muon analysis** An important branch of the low level analysis deals with the study of muon events collected by the camera.

This analysis is extremely useful since it gives an evaluation of the optical throughput of the telescope (mirror reflectivity evolution, pixel gain variations...). By knowing the expected amount of light and the trajectory properties of muons a simulation of the system response can be performed and, then, compared to the observed muon traces. The radius of muons' image in the Camera and the size<sup>9</sup> are proportional. Therefore, changes in this proportionality can determine variation in throughput.

Because of the muon intrinsic properties, what is seen is a ring, as shown in figure 4.4. As for the regular steps till DL1a, muon events have to be integrated and converted to p.e. The

<sup>7</sup>Further conditions based on the pedestal mean and standard deviation are usually applied in the noisiest pixels, e.g. the ones corresponding to stars' location.

<sup>8</sup>This time is around the pixel peakttime. A common used time threshold is 2 ns, because of Cherenkov light properties.

<sup>9</sup>In this context, size is understood as the total amount of light emitted by the muon.

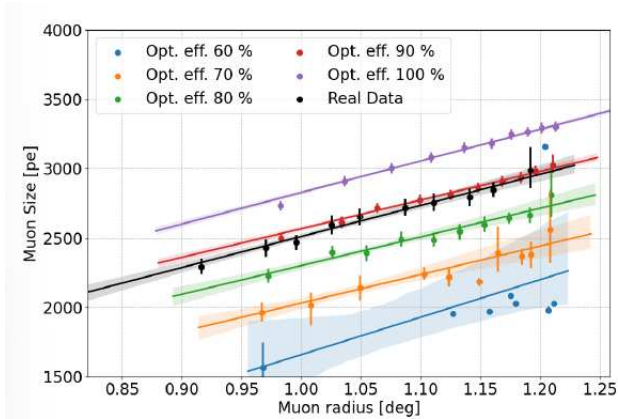


Figure 4.5: Data/MC intensity comparison. Thousands of muons are divided according to the radius and average intensity is taken for different optical efficiencies - steps of ten percent apart from the 60% optical efficiency. Real data of 2020 at 1.1 deg are also shown in the black [46].

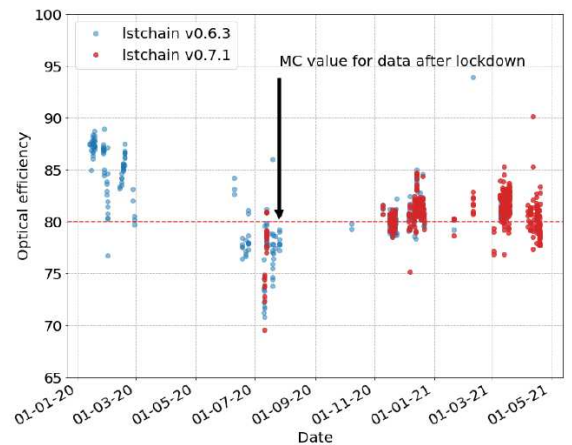


Figure 4.6: Optical efficiency *light curve* with two different `l1stchain` versions, no relevant changes in v0.8x [46].

unbiased<sup>10</sup> charge integrator is *GlobalPeak*.

The brightest and clearest events are selected and fitted: the main extracted parameters are ring intensity (total ring charge) and width, impact parameter, coordinates of the center. The intensity is computed by integrating over a larger ring region in order to rule out issues with PSF or mispointing.

**LST1 efficiency evolution** Interesting is to see the comparison between real and MC data as shown in plot 4.5. It concerns the efficiency before February 2020 [46]. The optical efficiency of the telescope is determined by comparing the various MC simulations with real muon data. After the Covid lockdown the efficiency is visibly degraded as shown in figure 4.6. The optical efficiency after the lockdown fell down up to a 20% loss. In the next steps, MC simulations of  $\gamma$ -rays, protons and electrons are run with the derived optical efficiency values.

To get the muon images the command `l1stchain_dl1_muon_analysis` on DL1 data can be used.

The before mentioned command line tool `l1stchain_data_r0_to_dl1` performs in both DL1a and DL1b steps, plus the muon extraction and analysis.

**DL1 Data selection** Once generated the DL1 data it is necessary to determine the data quality and try to behold issues in the telescope performance.

At the end of the night, LST On-site Analysis<sup>11</sup> runs two scripts (`l1stchain_check_dl1.py` and `longterm_dl1_check.py`) to produce a night-wise output in the formats `.html`, `.h5` and `.log`. Those output files contain useful quantities that, in most of the cases, depend on some observational and structural characteristics (zenith angle, pixel position, NSB level, trigger options, presence of stars<sup>12</sup>). Those files are contained in the IT Cluster [46].

The `.log` files contain written information about pixels' anomalies. LST1 collaboration has produced Jupyter notebooks to loops over the properties stored in the datacheck `.hdf5` files and that allow for data selection.

The data quality check is essential to select a "good" and "ponderate" set of data that are

<sup>10</sup>Essential in order to not introduce further differences between real and MC muon data, for instance due to a noisy night or FoV. A bias integrator is the one introduced in section 4.2, *LocalPeakWindowSum*.

<sup>11</sup>This procedure is not entirely automatic, it requires *shifters* that give a look at the night datachecks.

<sup>12</sup>The effect of stars on pixels has still to be implemented properly.

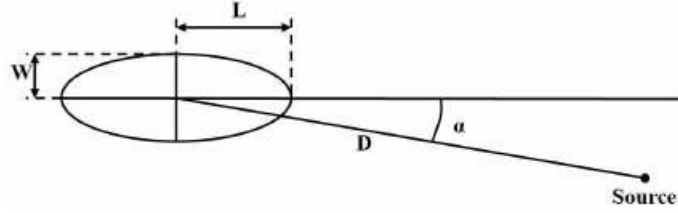


Figure 4.7: A scheme of the ellipse resulting in the Camera of Cherenkov telescopes. It is characterized according to the Hillas parametrization. [37]

worthy to analyse till the Higher Level stage. The selection is performed by mean of the `lstchain` notebook `data_selection.ipynb`: it scans over all the `DL1_datacheck_YYYYMMDD.h5` files and finds the runs of interest depending on some properties and cuts [46].

The observational characteristics are, for instance, observation mode, night conditions, sky pointing, zenith angle range, source name or coordinates, muon ring data.

The quality cuts, essential to rule out outliers, depends on the chosen source: each zenith-angle has its specific noise levels and rates.

**DL1b to DL2** From the parametrized shower images, the files having the reconstructed parameters of the primary particle (being it a gamma or cosmic ray) are derived [46].

The DL1b data contains the Hillas [33] (see figure 4.7) and time parameters of the shower images: those are used to estimate the primary particle reconstructed Energy, Direction (in  $(x, y)$ ,  $AltAz$ ) and type (gamma or proton) and its Gammaness.

The steps to achieve those results are:

1. Training/testing MC datasets (have a look at the next section 4.3.1) random separation: the ratio is usually set to 80/20 and it is important for the next stages
2. Merging of MC DL1 subruns dataset into a single `.hdf5` file.
3. Training of Random Forest models: the classical ML algorithms (Random Forest Regressor and classifier) are trained with DL1 data<sup>13</sup>
4. Applying the trained models to DL1 data (gamma, diffuse, proton, electron) to generate DL2 products: exactly what is done by `lstchain_dl1_to_dl2`.

What can be inferred from DL2 data are some relevant results such as the source detection significance and the related plot (only for the source independent analysis) and *gammaness* separation, and sky maps (in camera and sky coordinates: the observation mode is clearly visible from this one).

The significance is computed through the Li&Ma formula [39] (see formula C.1 in appendix C.1) as usually done in particle physics.

### 4.3 Final data reduction stages

DL3 data level is the point at which data is available for being used in the higher analysis. It is made up of gamma-like events, reconstructed from the air-shower, Instrument Response Functions (**IRFs**) of the telescope and some related monitoring parameters. Mathematically, the rate of the expected detected photons, with a reconstructed energy  $E$  and solid angle  $\Omega$ , can be in general expressed as:

$$\frac{dN_{\gamma}}{dt}(E, \Omega) = \int_E \int_{\Omega} IRF(E, \Omega | E_{true}, \Omega_{true}) \circ \Phi(E_{true}, \Omega_{true}) \quad (4.1)$$

<sup>13</sup>The set of parameters to train are specified in the configuration file.

where  $\Phi(E_{true}, \Omega_{true})$  is the sky flux model in terms of the *true* energies and positions. The IRF form is:

$$IRF(E, \Omega | E_{true}, \Omega_{true}) = A_{eff}(E_{true}, \Omega_{true}) p_{PSF}(\Omega | E_{true}, \Omega_{true}) p_{energy}(E | E_{true}, \Omega_{true}) \quad (4.2)$$

$A_{eff}$  is the effective area (in  $m^2$ ), the  $\gamma$ -ray detection efficiency,  $p_{PSF}$  is the angular resolution (in  $sr^{-1}$ ) and  $p_{energy}$  is the energy dispersion (in  $TeV^{-1}$ ). The last two probabilities are the ones that the events  $(E_{true}, \Omega_{true})$  migrates to  $(E, \Omega)$ . The IRF is usually in  $m^2 TeV^{-1} sr^{-1}$  units.

As the high-level data format regards, Gamma-Astro-Data-Format (**GADF**)<sup>14</sup> [5] is used for CTA telescopes, such that it has a open community access. Astropy package is employed to write DL3 data in FITS format. Each HDU within DL3 FITS files is classified in a hierarchical way. The HDU tables are:

- EVENTS: events list
- GTI: Good Time Intervals
- POINTING: pointing directions of the telescope for some time stamps
- RESPONSE: different IRF components. It has different sub-classes, such as EFF\_AREA, BKG, EDISP or RPSF or, furthermore, how the IRF has been produced (POINT-LIKE or FULL-ENCLOSURE). Lastly, the last sub-class refers to the name of the specific format.
- INDEX: observation index and HDU

The three main tools to produce DL3 data have already been mentioned in the introduction 4.1. Detailed descriptions follow in the next paragraphs.

### 4.3.1 The simulated instrument response

**MC production** Monte Carlo simulated data are generated with Corsika [31] and `sim.telarray` [15]. The former develops the extensive air shower and the emission of Cherenkov light by the shower particles (have a look at figure 4.8), including specific atmospheric and geomagnetic properties for ORM location [21]. The latter concerns the signal recording by the instrument<sup>15</sup>.

**New all-sky MC** Until May 2022, LST analysers could only rely on two zenith angle MC simulations: 20° and 40° for south telescope pointings. This severe limitation caused potential biases in the reconstruction of fluxes and spectra [46].

Currently, all-sky MC simulation has been developed, allowing a better results' accuracy. For instance, the geomagnetic parameters are by far more precise than before.

Simulations are produced for many combinations of zenith and azimuthal angles. As a matter of fact, from those simulations, the analyser should produce all the IRFs using his own configuration file for the events selection and binning. The IRFs files have to be stored in the same location so that in the step for creating the DL3s a single nearest or an interpolated IRF can be chosen by adding the flags `--irf-file-pattern`, to provide the directory, and `--use-nearest-irf-node`, the function to take the position of the closest IRF to the input DL2.

The simulated MCs are represented in a grid, following the Delaunay triangle method, in

<sup>14</sup>It is an unofficial effort to cover all high-level data from gamma-ray telescopes, being them pointing (IACT) or slewing (Fermi-LAT, HAWC). A further development in the future is to include astroparticle data too [49].

<sup>15</sup>It includes optical-ray tracing of the photons, their recording by PMTs, different discriminators at the pixel level and at the telescope trigger level and digitization of the resulting signal [15].

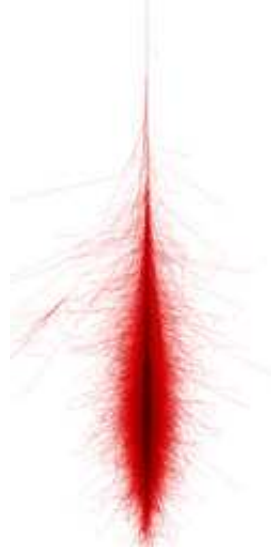


Figure 4.8: Corsika simulated air extensive shower of a 1 TeV  $\gamma$ -ray incident with a zenith angle of  $0^\circ$  [4].

terms of the interpolation parameters:  $\cos(\text{zenith})$  vs  $\sin\delta$ , where  $\delta$  is  $B_{\text{perp}}/B_{\text{total}}$ <sup>16</sup> as shown in 4.9. The boolean parameter to check the position in the grid are provided by the function

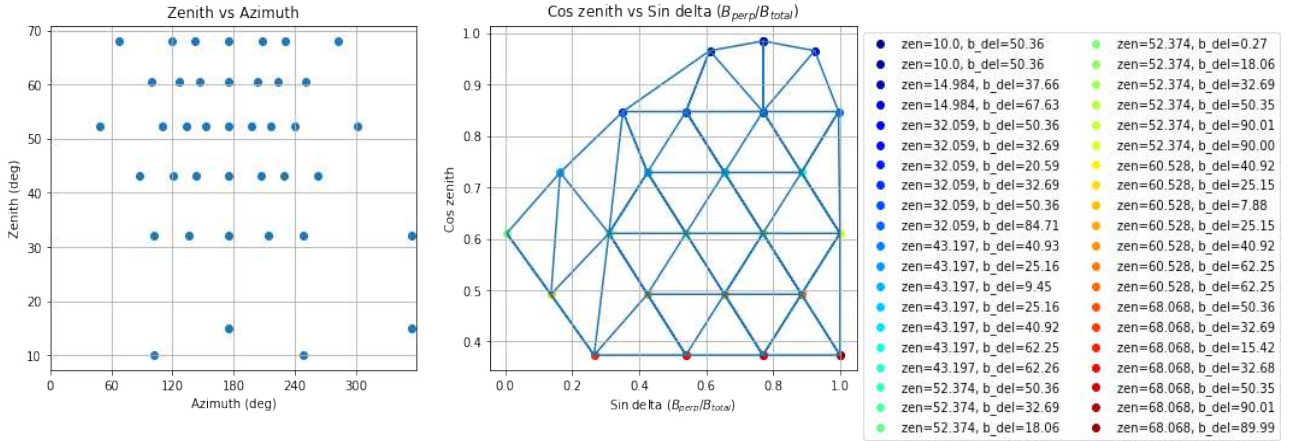


Figure 4.9: (left) Nodes of the 40 produced MC simulations depending on Zenith and Azimuth angles. (right) Delaunay triangles produced from the nodes specified in the legend. These ones depend on the Zenith angle and the parameter  $\delta$ , defined as  $\delta = \cos^{-1}[\sin(B_{\text{inc}})\cos(\text{zen}) - \cos(B_{\text{inc}})\sin(\text{zen})\cos(\text{az} - B_{\text{dec}})]$ . Thanks Dr. Chaitanya Priyadarshi for the plot.

`check_in_delaunay_triangle`, a `lstchain.high_level.interpolate` function. It returns a list the three closest nodes in the grid surrounding the target. If the IRF is contained within a grid triangle one can get the interpolated IRF: the data of the three are stacked using `load_irf_grid` and the final IRF is obtained exploiting the `pyirf` interpolation functions. If the target node is outside any possible Delaunay triangle or the flag `--use-nearest-irf-node` is used, the closest IRF node is returned back as the Final IRF.

**Generation of IRFs** To generate IRFs and sensitivities of CTA telescopes, `pyirf` Python2-based library is used<sup>17</sup> [46]. It allows to produce the usual IRFs components:

<sup>16</sup> $\delta$  is the geomagnetic angle; it can be traced back from the mean zenith and azimuth pointing of the observation (they can be read by mean of the function `read_data_d12.to.QTable`) thanks to the function `get_geomagnetic_delta` from `lstchain.reco.utils`.

<sup>17</sup>Potentially it can be used also to process data from other IACTs.

- Effective area: proportional to detection gamma-ray efficiency and computed as function of the true energy.
- Energy migration: it is built from the dispersion energy matrix<sup>18</sup>.
- Point spread function: probability of measuring a gamma-ray of a certain true energy and position at a reconstructed position.

In LST1 context, two types of IRFs are produced. IRFs is for the best sensitivity of the instrument and analysis pipeline from MC data; it also includes the cuts optimizations, for instance gamma-hadron score in each energy bin of the reconstructed energy. The other IRFs, that are in the interests of this work, is for the real data analysis. Each analysis has its own specific cuts and IRF.

IRFs of `1stchain` are produced from the testing MC data (quoted in 4.2): they employ the DL2 testing files of protons, electrons and gammas (point-like or diffuse) produced thanks to `1stMCpipe` tools<sup>19</sup>. At each new `1stchain` release, `1stMCpipe` is run and the resulting models are stored in the IT Cluster. An entire production is configurable from a single given configuration file, containing the information on `1stchain` version, zenith angle and pointing, particle type and the `1stchain` stage.

Lastly, the sensitivity curves can be compared and analysed thanks to the line command `1stmcpipe_compare_irfs`.

`1stchain_create_irf_files` The aim of this tool is the combination of MC simulations with a specific configuration file to produce the IRF. The inputs are the resulting files of the previous paragraph 4.3.1 of the different particle types<sup>20</sup> and the configuration file in `.json` format.

The latter contains some parameters on data filters, cuts and binning methods:

- "EventSelector": "filters" options select the event with the Hillas parameters in a given range. In addition, the event's types are selected (for instance, it is usually set "event\_type": [32, 32], referring to the cosmic ray events).
- "DL3FixedCuts": energy and angle independent cuts are set for the gamma/hadron index and the  $\theta$ , to define the ON region.
- "DataBinning": it contains information on the binning methods of the true, reconstructed and migration energies, and also on the allowed offsets of the FoV, background and source.

In the command line a flag `--point-like` or `--diffuse` has to be specified depending on the case of interest.

**Energy-dependent *gammaness* cuts** As the  $\gamma$ /hadron distinction regards, it could be also applied an energy-dependent cut [46]. The reason why to perform such a sophisticated cut on the  $\gamma$ -hadron parameter is inside the distributions of the shower events: they are dependent on the energy of the primary particle. It can be seen that the *gammaness* distribution varies along the full reconstructed energy range.

It is needed a fixed efficiency in selecting events in each energy bin range. Efficiency that could be either constant along all the covered reconstructed energy bins or dependent on the varying instrument's sensitivity. The former can be easily introduced in the configuration file by including the "gh-efficiency" parameter and consequently running the IRF tool with the extra flag `--energy-dependent-gh`. The higher is the efficiency, the harder is the cut, so an

<sup>18</sup>Ratio of the reconstructed energy over the true energy as a function of the true energy

<sup>19</sup>`1stMCpipe` contains scripts to ease the reduction of MC data. They also allow the analysis/creation of data from R1 to DL2 and of the IRFs.

<sup>20</sup>A particular attention has to be paid in taking the MC results coming from the same `1stchain` version as the one used for the DL2 data that are going to be analysed

increasing probability of losing some  $\gamma$ -ray events. In the latter mentioned energy-dependent case, the cut is the lowest one needed to get a 5 sigma detection, in a specific energy bin, having 50 hours of simulating data (so the best instrument's sensitivity). The same discussion is done in the case of energy-dependent  $\theta$  cuts in selecting the source region.

### 4.3.2 Generation of the event files

`lstchain_create_dl3_file` It takes as input the DL2 file, the produced IRF and the same configuration file to create the DL3 ones. Through this command line the selection criteria, binnings and cuts of 4.3.1 are applied to DL2 data. The sizes of the DL2 events tables visibly decrease after these filters and cuts.

In addition, the source name and coordinates are introduced by the appropriate tags.

`lstchain_create_dl3_index_files` Once the DL3 files are sorted in a list-object, the HDU table is generated through the Python function `create_hdu_index_hdu` and `create_obs_index_hdu` contained in the package `lstchain.irf.hdu_table`.

The *obs* file of the two contains explicitly all the observation information: ID, date, time elapsed, livetime, zenith pointing and so on. Various metadata, including Provenance data<sup>21</sup>, are added as header values.

On the other hand, the *hdu* file tabulates the file-based information of all HDUs contained in the DL3.

It is important to update the index files every time a DL3 file is added, removed or modified. The index files include information about the data production that is available during the analysis.

The DL3 production depends on the scientific purposes of the higher analysis. For example, the IRFs type could be either *Full-containment* or *Point-like* (the former obtained by integrating the PSF on the ON region, the latter has a directional cut around the assumed source position, without the PSF component).

The specific event selection and binning are also chosen in the configuration file. The choice of production both for DL3 and IRF files are concerns of this stage too. So the IRFs and DL3 files have to be produced again every time the analyser changes the analysis purposes and specific cases.

## 4.4 Source dependent and source independent analysis

The analysis of a source could also be accomplished by assuming the real position of the source for the data reconstruction and the higher analysis [46]. It is an efficient method of approaching to the source reconstruction since the energy resolution around the peak improves and it achieves better performances with the point-like gamma MC (it is shown in plot 4.10). As it can be inferred, the source dependent analysis has a better flux sensitivity below 100 GeV compared to the independent approach. Moreover, in figures 4.12 ( $\gamma$ /hadron separation in source independent analysis) and 4.11 (source dependent one) can be seen that gamma and proton histograms are *less overlapped* in the source dependent case. In addition, both shown that the performance of the  $\gamma$ /hadron separation is energy-dependent, being it much better at higher energies.

Another improvement in the source dependent analysis concerns the migration energy plot 4.13 and in the correlation plot "dist vs impact parameter" 4.14. The former shows that,

---

<sup>21</sup>Provenance data contains information about all the processes occurring on the data, including which software produced it and all the steps that have modified that data. It is essential for the data products traceability and reproducibility.

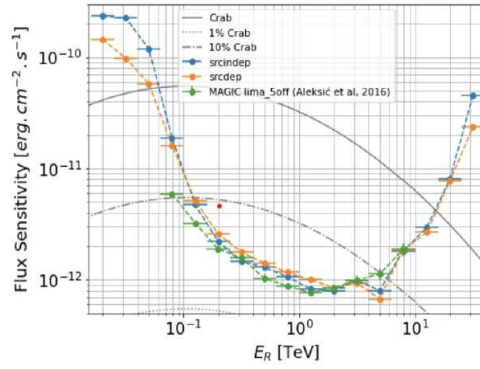


Figure 4.10: Flux sensitivities for the source independent (*blue*) and dependent (*orange*) [46].

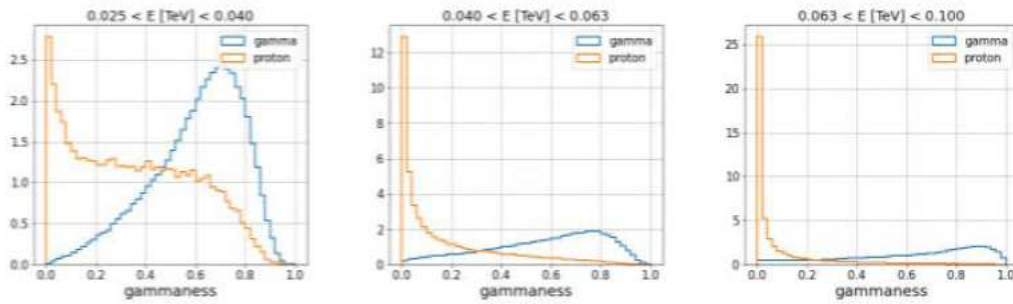


Figure 4.11:  $\gamma$ /hadron separation in three energy bands for the source dependent analysis [46].

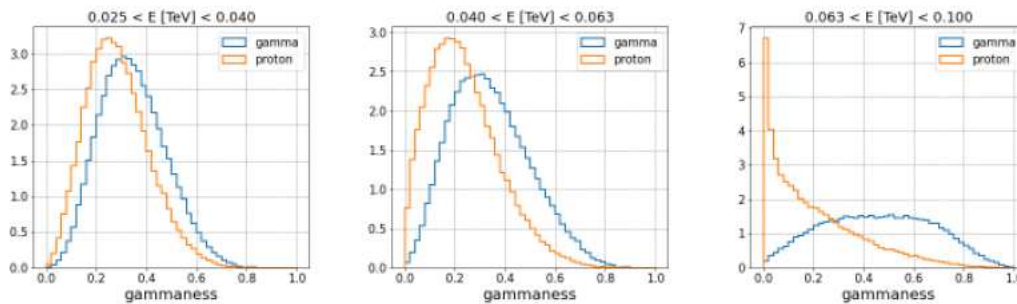


Figure 4.12: *Gammaness* plot in the source independent approach in three energy ranges [46].

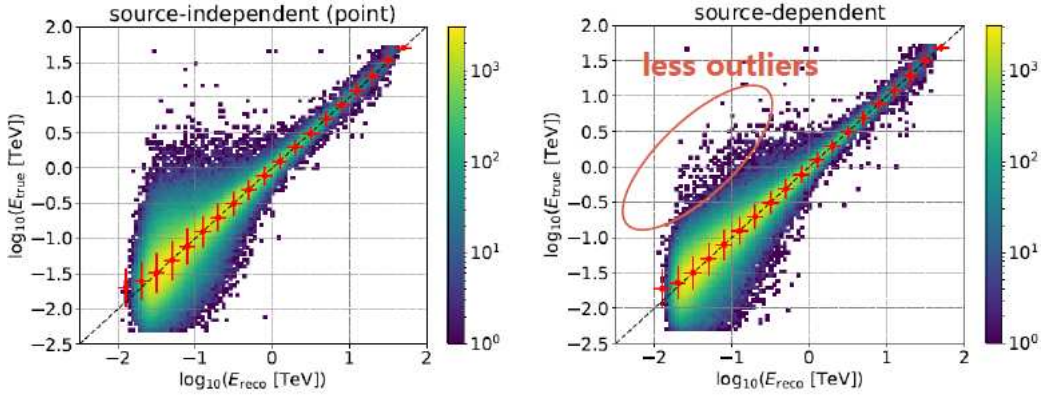


Figure 4.13: Energy migration histogram for the source-independent and -dependent analyses, representing the true energy of the MC events as a function of their reconstructed events [46].

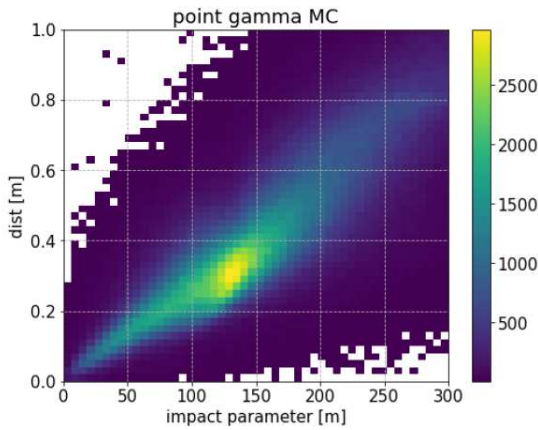


Figure 4.14: Correlation plot between **dist** and **impact** parameters [46].

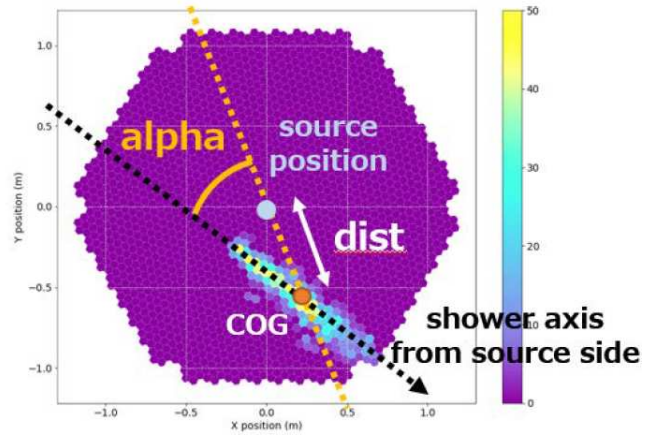


Figure 4.15: Parameters introduced in the source dependent analysis [46].

in the source dependent case, at low energies, the outliers' number decreases. The latter exhibit a defined correlation between the two parameters, always in the energy band below 100 GeV. New parameters depending on the known source position (assumed as a point-like target) are employed in the RF models and in the higher analysis' stages. Those new ones are in particular: alpha, dist, time gradient, skewness [46] (4.15 is a sketch of these parameters in the camera). Those are introduced in the DL1 stage through the `lstchain` tool `lstchain_add_source_dependent_parameters`: in this context other specific dependent configuration files have to be used, also to train new RFs for both gamma and proton. Moreover, to pass from the DL2 to the DL3 the flag `--source-dep` has to be added to the tools `lstchain_create_irf_files` and `lstchain_create_dl3_file`. In the source dependent approach the theta cut is replaced by the **alpha cut**, referring to the new parameters introduced at the DL1 stage.

The source position is defined in such configuration file; in addition, the mode of observation has to be specified. It could be 'on' or 'wobble' - in this latter case the off regions' number has to be declared.

For a single event in the Wobble mode the parameters are computed for the source position and the off ones.

Lastly, in the source dependent configuration file the MC data for gamma comes from the real source position, whereas the MC proton data from a nominal position declared as:

```
"source_dependent": true,
"mc_nominal_source_x_deg": 0.4,
```

```
"mc_nominal_source_y_deg":0.0,
```

In the step to pass from DL1 to DL2, in addition to the proper dependent configuration file<sup>22</sup>, the source dependent trained RF has to be inserted.

## 4.5 Scientific products

As introduced in 4.1, the High level data are divided into three categories:

- DL4: DL3 data binned in Data Cubes and Maps
- DL5: DL3 and DL4 data combined over a specific spatial, temporal and spectral region.
- DL6: catalogued DL5 data.

Two different analyses can be performed at this stage: the 3D analysis consists in considering a field of view containing overlapping gamma-ray sources. On the other hand, if one considers all the binned in energy events inside a source, by defining an ON region, a 1D analyses might be performed. For the concerns of this work, only the 1D analysis will be presented for LST1 [19].

A background model, necessary to produce skymaps<sup>23</sup> and to perform 3D analysis, is not needed for the 1D analysis case, and therefore it is not considered in this work. To estimate the background, the events' number in OFF regions are measured. The OFF events are from regions of the FoV that does not contain gamma-ray sources. The background rate is assumed to be the same to the one in the source region.

For the ON-OFF measurements, the *wstat* fit statistics without background model is used. *wstat* is the statistic function contained in `gammapy.stats.fit_statistics` that uses a background estimate number  $n_{bkg}$  taken from OFF measurements (the variable names of the analysis are the same used in equation C.1).

The first step is the observation selection [19]. A list of DL3 files is stored in a **DataStore** object. A check on observation metadata or HDU information for each DL3 file is done according to the needs of the analysis. For instance, the selection could depend on the zenith pointing angle, total livetime, observation mode, object name.

The selected list contains the **Observations**, in its turn containing events and IRF information from the selected DL3 data.

The next procedure consists in creating the base geometry of the ON region and the spatial grid where to bin the events. The Signal Extraction Region is usually created through a **CircleSkyRegion** object, whose center is on the source position and the radius is the one set in the configuration file for the  $\theta$ -cut (only for point-like IRFs).

To create the spatial grid where the event reconstructed position are binned, **RegionGeom** is exploited by specifying the ON region, just created, and the reconstructed energy axes. These axes have been created in advance by the tool **MapAxis** in which the units, boundary values and binning can be chosen.

Two primary pixelization formats for the sky maps are: the World Coordinate System (**WCS**) and the Hierarchical Equal Area isoLatitude Pixelization of a sphere (**HEALPix**) [19].

A mask on the nearby gamma-ray sources<sup>24</sup> or any other regions can be applied to exclude the events with a reconstructed direction from that sky zone.

Once created the geometry, the Data reduction procedures have to be performed to create

---

<sup>22</sup>It also contains the source dependent parameters (*dist*, *skewness\_from\_source*, ...) for the energy estimation and the gamma/hadron cut. From these DL2 parameters (*reco energy*, *gammaness*) are obtained for each region

<sup>23</sup>A proper Background model Skymap, to be subtracted, is currently unavailable for LST1 analysis.

<sup>24</sup>It is used to check on catalogues like <http://gamma-sky.net/> if some gamma-ray emitters are in the FoV.

Dataset and Data Reduction Makers. They prepare the data for modelling and fitting processes, so the aim is to bin events into counts maps.

Two types of maps depending on the specific usage are available: either a **SpectrumDataset** or a **MapDataset**. In LST1 analysis the former is used: it is needed to provide the geometry (in terms of reconstructed energy and position) and the true energy axis for the IRFs map.

The object that creates such a SpectrumDataset is the **SpectrumDatasetMaker**: in this case the maps produced are the counts, exposure and energy dispersion ones, not for the background.

Among different techniques to estimate the background, **ReflectiveRegionsBackgroundMaker** object is commonly used. Many parameters can be handled: the minimum distance of the OFF regions from the source position, the maximum number of OFF regions, the excluded zones and so on.

To take only safe energy ranges, so to rule out those associated with high systematics on IRFs, a **SafeMaskMaker** is exploited. For instance, a mask with a maximum effective area or offset angle.

At this point the spectrum Dataset can be generated by inserting all the observations in an empty one. In this phase, SpectrumDatasetOnOff object can also be used in place of the Background maker. Actually all the **SpectrumDatasets** objects are loaded in a **Datasets** one.

It is a good habit to produce some plots to check, for example, the relation between significance and livetime of the observation, the exposure and the energy dispersion. It is important to spot some anomalies in data.

The Datasets object is usually saved in OGIP files [3]. The files are of four types:

- **PHA**: it contains the spectrum data
- **BKG**: it brings the Background scaling factor, so the exposure ratio between signal and background counts.
- **ARF**: incorporating the effective area
- **RMF**: it has information about Energy Dispersion.

These files can be read back to produce the Light Curves and SEDs. The OGIP files are read through a function applied to a SpectrumDataset object `.from_ogip_files`.

**Modeling and fitting data** The functionalities to model and fit the data contained in a Datasets object are in `gammapy.modeling` package [19].

The general first step is to define a list of **Skymodel** objects. Each of these ones is a factorized model with three components: **SpectralModel**, **SpatialModel** and **TemporalModel**. Only the spectral model is mandatory, the other two are optional. In particular, the spatial models are necessary for a 3D analysis.

As the Light Curve estimation regards, the object **LightCurveEstimator** is employed by providing the source name, energy edges or time intervals, indeed the specific binning.

The fit is performed by applying the **Fit** function to the Datasets object. The selected global model created are fitted to the Datasets. Many fitting methods and optimizations are available: the default is the *minuit* global backend. The others available are *sherpa* and *scipy*. Each backend has its own optional optimizing arguments.

Two kinds of Likelihood fits can be done. A **Joint analysis** is when the Fit function is run on each individual dataset specified. Then the flux points are estimated by joining the spectral fit results from all datasets.

On the contrary, the **Stacked analysis** consists in stacking all the datasets into a single one: the Fit and the consequent estimation of flux points are applied to such a stacked dataset object. Stacking implies that counts, background and reduced IRFs from all the runs are binned together to build a unique dataset; its Likelihood is computed during the fit. The

total fit statistic of a stacked dataset is not equal to the one obtained in a joint analysis: the latter is the sum of the fit statistic of each dataset. Running a fit on a stacked dataset is less computationally intensive than a joint fit.

The flux points are estimated through **FluxPointsEstimator** in which the energy bins have to be specified as well as the datasets. In addition, many others parameters can be specified, as the  $\sigma$  number for upper limit computation or the additional quantities to estimate (asymmetric errors on flux or fit statistic profiles).

Checks on the produced flux points can be performed, like on the likelihood profile and the model parameters obtained. Moreover the Flux Points and the final model can be stored into a **FluxPointDataset** or in `.fits` or `.dat` files. From this one is ready to draw the scientific relevant products, SEDs, Light Curves and Differential fluxes.

# Chapter 5

## Data reduction of 1ES1959+650 LST1 observations

### 5.1 Data selection

The data selection has been performed on the DL1 files in order to find out the runs where the telescope was pointing towards 1ES1959+650, being under some optimal observational conditions. 56 runs of the source of interest have been selected, for a total observation time is of **13.95 hours**. Not all of them are precisely Wobble [14] observations. Those non-Wobble will be discarded in the higher level analysis.

The Wobble observation technique is important since source and background regions are taken simultaneously, so under the same observational conditions, and they are in a symmetrical offset with respect to the centre of the Camera.

The output list of the runs is in A appendix.

The cuts applied during data selected are:

- A mask on the runs whose pedestal are *infinite*, i.e. the `numpy` function `isinf` is used.
- Angular distance of the source from the centre of the camera:  $[0.25^\circ; 0.55^\circ]$ , as shown in 5.1. The current standard LST1 offset is set to  $0.4^\circ$  to match that if the MAGIC telescope.
- Zenith and azimuth mean angles: the all wide range is taken, since the simulations cover the sky up to a zenith angle of  $68^\circ$  (figure 5.2).
- The maximum pedestal standard deviation is set at  $1.9 \sigma$ . It is affected by the Sun and Moon elevations<sup>1</sup>.
- On the too low or high cosmic ray rates: outliers are filtered using the median and the interquartile range (32 to 68,  $1 \sigma$  in Gaussian distribution) since the mean could be affected by outliers 5.3 and A.1. The number of maximum standard deviations from the median to reject a run is  $3 \sigma$ . There are also hard cuts, indeed the rate have to be in the range  $[2 \cdot 10^3; 2 \cdot 10^4]$ .
- A mask on the pixel rate: the cosmic fraction pulses above 10 and 30 p.e. are taken and the same filters of the previous point are applied (see figure A.2).

---

<sup>1</sup>Some plots can be produced to evaluate night by night Moon and Sun positions related to the pedestals' values.

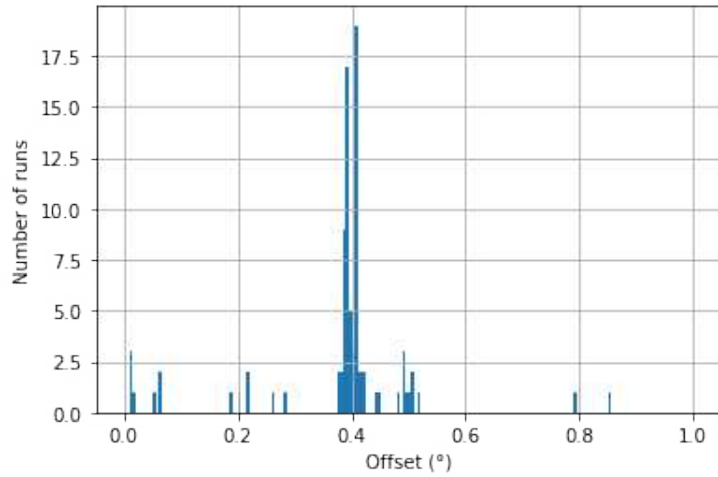


Figure 5.1: Histogram of the offset of 1ES1959+650 LST1 observations. The offset is the angle between the camera centre and 1ES1959+650 position.

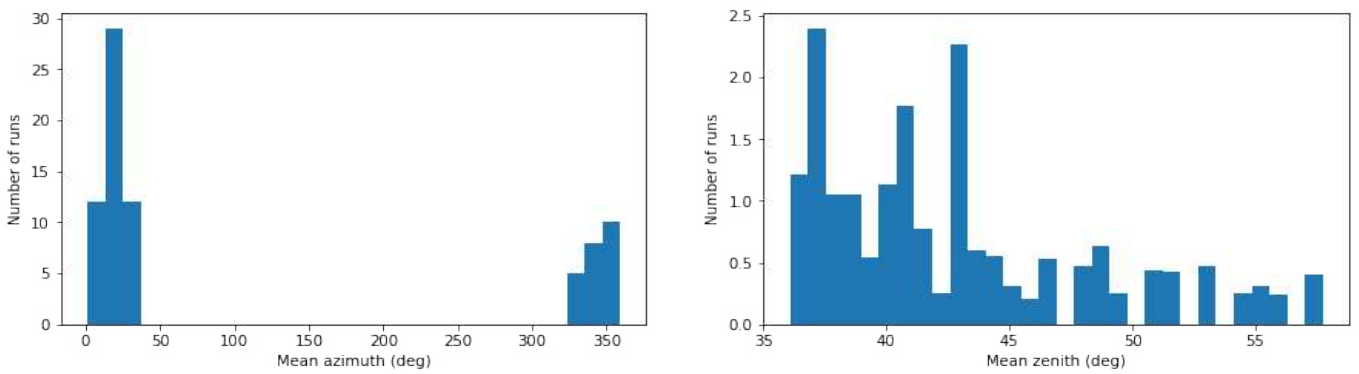


Figure 5.2: Runs mean azimuth (*left*) and zenith (*right*) angles of observation.

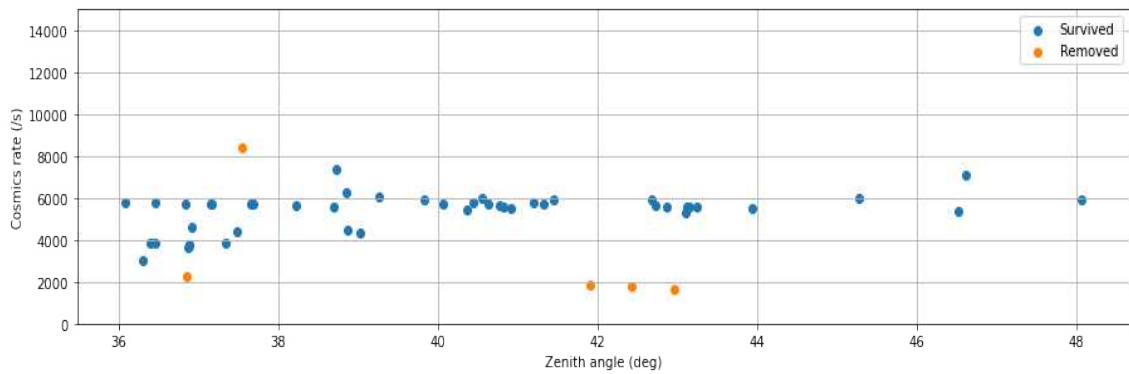


Figure 5.3: Variation of cosmic rate with the zenith angle (in *orange* discarded runs).

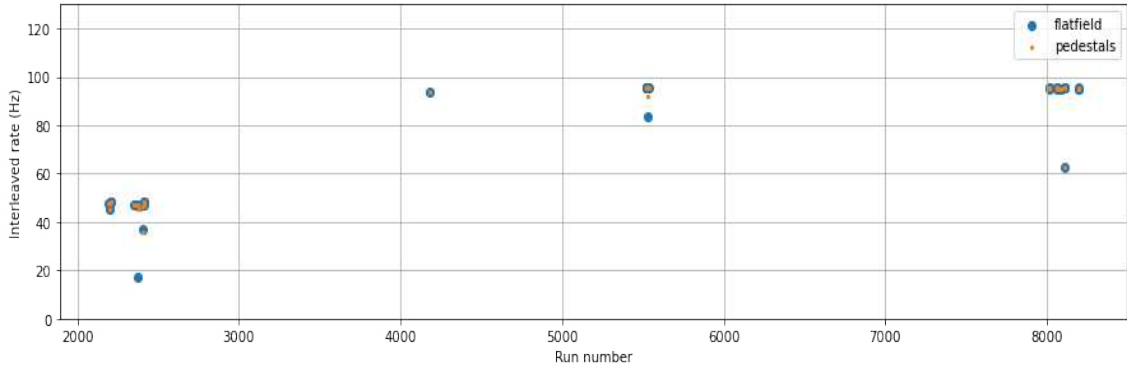


Figure 5.4: The interleaved event rates are catalogued per runs: the flatfield (*blue points*) and pedestal (*orange*) are shown (most of the times they coincide).

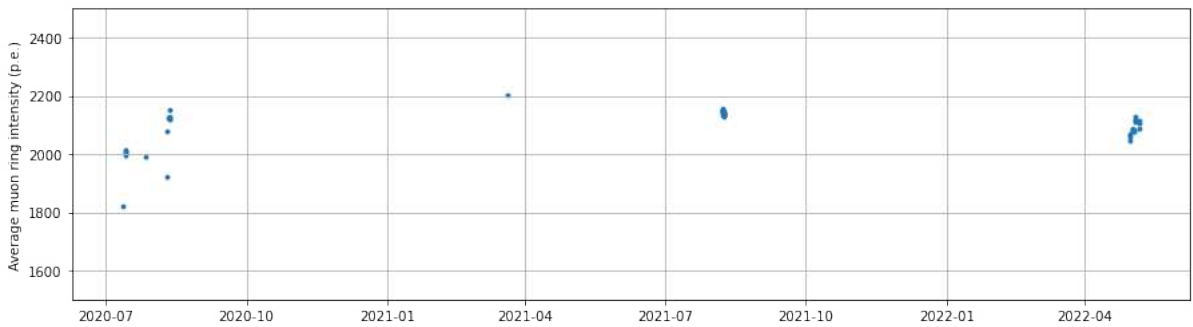


Figure 5.5: Mean intensity of muon rings in photo-electron units for each run.

A check on the interleaved is in the plot 5.4: it should be  $\sim 100$  Hz,  $\sim 50$  Hz for the oldest LST1 data. If it is not it can be due to a dead time. However, from the figure two very low rate points are quite evident, the first is among 2020 runs, the other among 2022 ones.

The rates of muon rings and their intensities have to be checked too: they are reported in figures 5.5 and A.3. A slowly negative slope of the contained muon rate is visible in dependence of the zenith angle. It seems reasonable since at high zenith angles the particles produced have to pass through more atmospheric depth. As written in section 4.2, it is important also to show the trend of the muon detection efficiency through the selected runs, as shown in figure 5.5, in order to infer the telescope optical efficiency stability. It can be seen how it is stable, especially in the *cluster* of the latest runs. The high intensity value of the March 2021 run is likely due to a recovery of a group of mirrors.

The time resolution is accessible from the standard deviation of the pixel time measured in FF events. From 5.6 plot, the time resolution, in most of the case, is close to the typical value of  $\sim 4$  ns.

Apart from the same suspiciously too low value of one of the latest runs, neither the FF charges spot particular problems (figure A.4).

At this stage also the subrun-wise information can be accessed, for instance the cosmic rate pulses for p.e.  $> 10$  and  $> 30$  as in figure A.5, where the subruns have been tidily indexed.

Lastly, a further cut on the standard deviation of the pulses  $> 30$  p.e. rate is performed at a value of 0.2: this could be due to anomalies in the observation (car flashes, MAGIC LIDAR, ...). A.6 is the distribution before the cut. After applying the cuts and thresholds on noise parameters and observational conditions, the list showed at the beginning of the appendix A is produced.

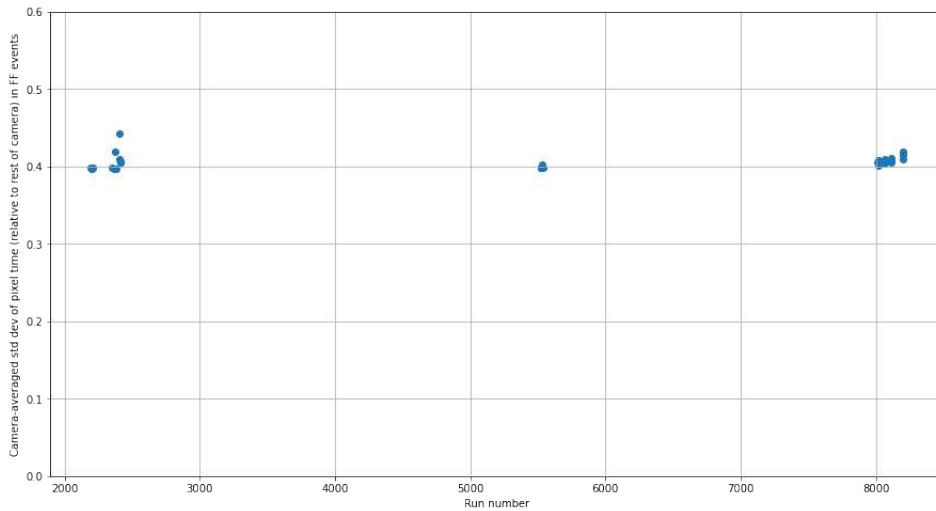


Figure 5.6: Time resolution averaged over all the camera pixels.

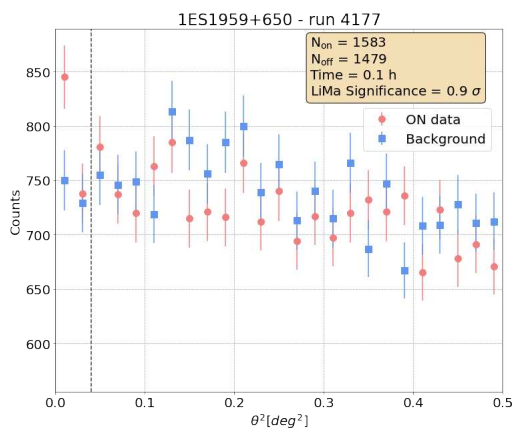
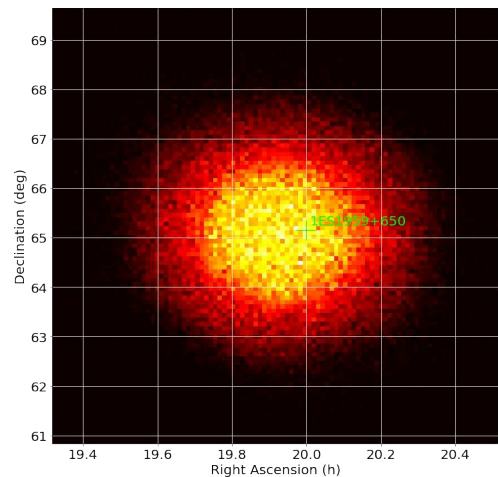
Figure 5.7: DL2  $\theta^2$  plot of the run 4177. In the legend the counts of the source and background regions, the observation time and the Li&Ma significance. The  $\theta^2$  cut is at  $0.04 \text{ deg}^2$ .

Figure 5.8: 2D Histogram plot in Galactic coordinate of the run 4177.

## 5.2 Detection plots

The most largely used way to quantitatively estimate the detection significance of the source in the source independent approach is the  $\theta^2$  plot production [46] and the Li&Ma significance (formula C.1) computation [39].

The graphic can be made either with DL2 data or DL3 one: it is based on the  $\theta$  parameter, the angular distance between the reconstructed position and the position of the observed source. For instance, at the DL2 stage a single-run  $\theta^2$  histogram can be depicted as in 5.7. The related 2D histogram (run 4177) is in figure 5.8.

For Wobble observations, the ON region  $\theta^2$  profile is computed by mean of the *on\_position* distribution. On the other hand, the OFF profile is extracted by a mirror position radially symmetric to the ON position in the FoV. ON and OFF position are assumed of the same size, so that the normalization factor is fixed to 1.

To produce the `astropy.table.Table` containing ON and OFF counts and acceptances,  $\alpha$  and the statistic for each bin, the objects are:

- An observations' list
- $\theta^2$  and reconstructed energy binnings to compute the distribution

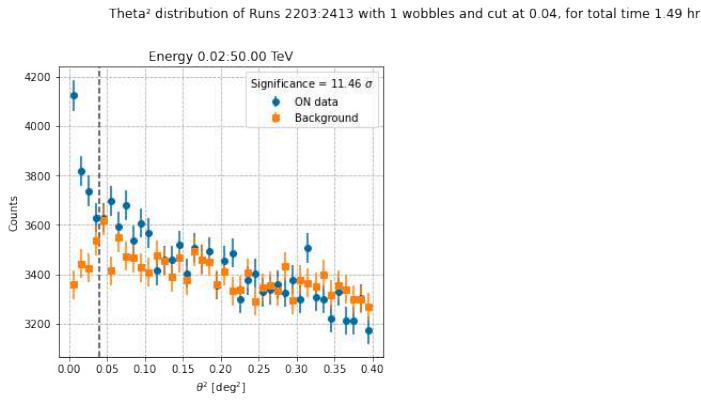


Figure 5.9:  $\theta^2$  plot and significance for 2020 dataset.

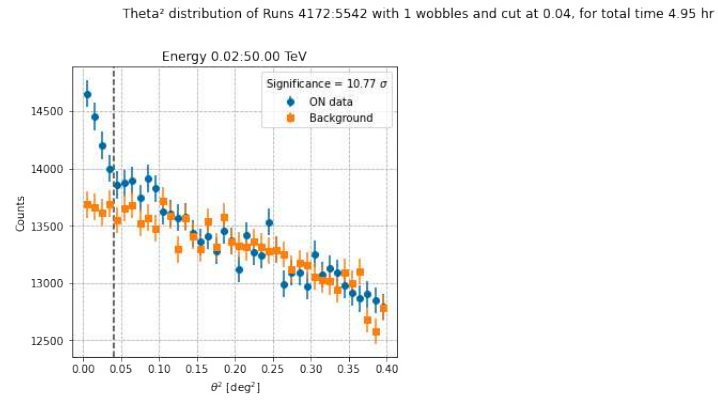


Figure 5.10:  $\theta^2$  plot and significance for 2021 dataset.

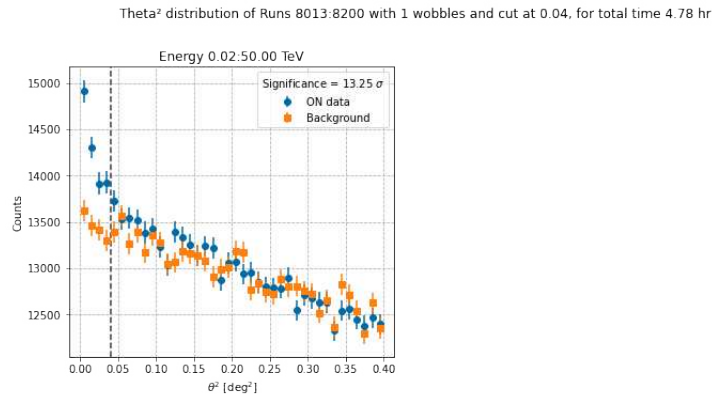


Figure 5.11:  $\theta^2$  plot and significance for 2022 dataset.

- Minimum and Maximum  $\theta^2$  normalization factor
- ON and OFF positions
- Wobble positions to consider for the OFF ( $90^\circ$ ,  $180^\circ$ ,  $270^\circ$ ) and maximum positions number

$\alpha$  is the acceptance divided by the OFF one, given the fact that ON and OFF have the same size and exposure time<sup>2</sup>.

This table is then used to plot the distribution of ON, OFF counts, excess and significance. To compute the Li&Ma significance the  $\theta^2$  cut has to be specified too.

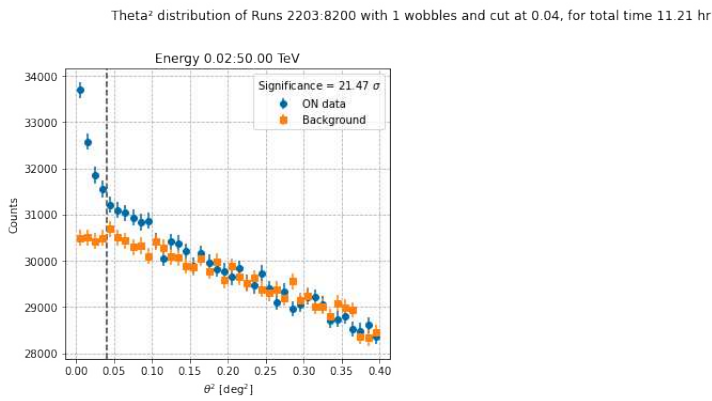
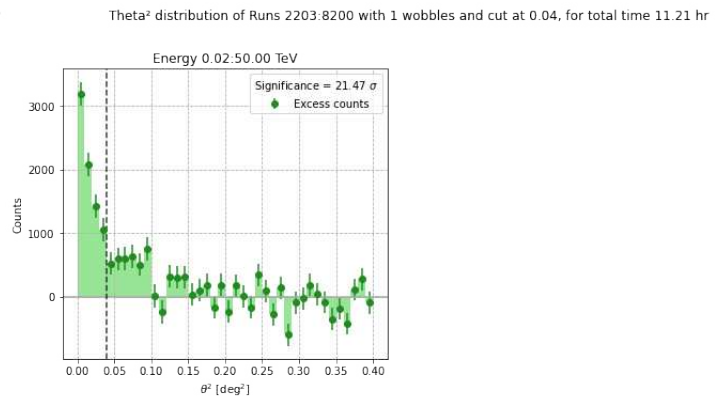
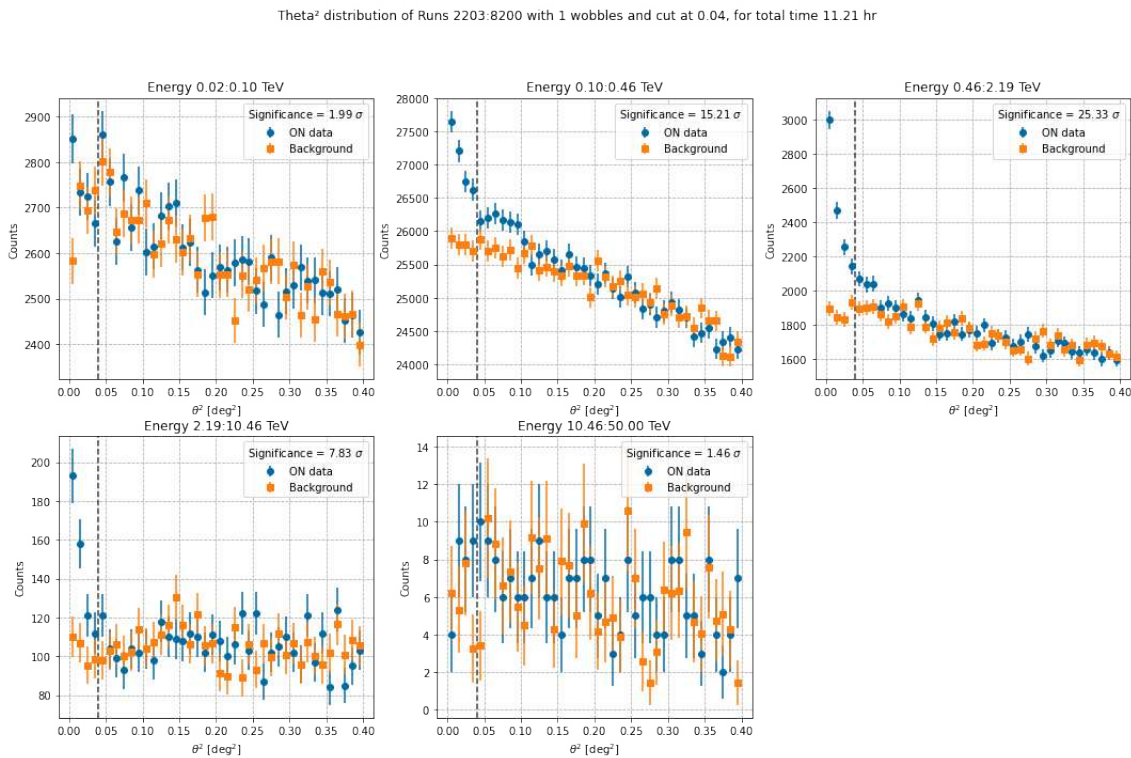
The  $\theta^2$  plots for the selected runs are showed in the following. They are grouped in three sets according to the year (2020 in 5.9, 2021 in 5.10 and 2022 in 5.11 datasets). Then, an overall plot - stacking the three datasets together - has been produced in 5.12. The related excess graphic is in 5.13. All the plots contain the Li&Ma significance, considering a  $\theta^2$  cut of  $0.04^3$ , and they have been made taking into account the counts within the broad energy range 0.02-50 TeV.

From the  $\theta^2$  plots, high detection significance is obtained for all the datasets analysed. The lowest significance value is of  $\sim 11 \sigma$  in the 2021 dataset - it contains only two intense nights of observation, for a total effective time of almost 5 hours. Also for the 2020 dataset, although a quite short exposure of  $\sim 1.5$  hours, exhibit a large detection significance in correspondence of the source position.

The source behaviour in different energy bands is evaluated by calculating  $\theta^2$  plots for each

<sup>2</sup> $\alpha$  corresponds to  $n$  in equation C.1.

<sup>3</sup>In all the  $\theta^2$  plot such cut is bordered by the vertical dashed line.

Figure 5.12: Total dataset  $\theta^2$  plot.Figure 5.13: Excess  $\theta^2$  plot of the total dataset.Figure 5.14:  $\theta^2$  plots of the total dataset in three different energy ranges.

band.. Total dataset plots in 5 energy ranges is shown 5.14. The main contribution to the total significance is constituted by the detected emission from  $\sim 450$  GeV to  $\sim 2.2$  TeV. Both the first and the last plots of 5.14 present a poor detection significance - less than  $2 \sigma$  - and not a clear excess of the source counts at angles close to 1ES1959+650 position.

The low significance in the lowest energy bin is likely due to the observation difficulties of detecting low energy  $\gamma$ -ray at high zenith angles.

As the band from  $\sim 10$  to  $50$  TeV concerns, the source has been detected with a confidence of  $\sim 1.5 \sigma$  because of a combination of the limited LST1 sensitivity and the low VHE  $\gamma$ -ray flux from extra-galactic sources. Indeed, the Extra-galactic Background light extinction becomes larger as the source distance from us and the  $\gamma$ -ray energy increase.

## 5.3 Applied Instrument Response Functions

The IRFs of this analysis has been produced thanks to the new All-sky MC data and the techniques treated in 4.3.1. To approach the source analysis the flag `--point-like` is added

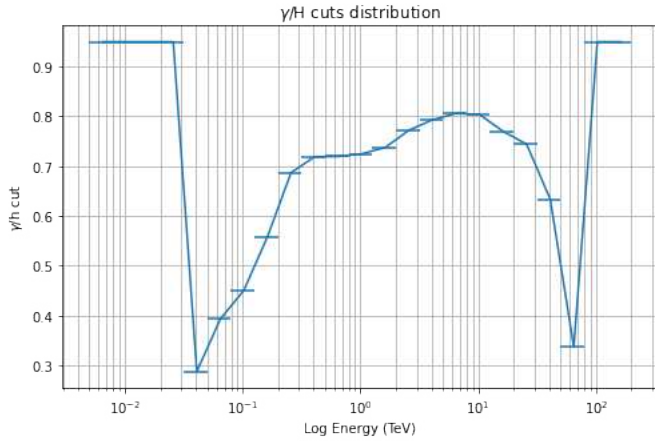


Figure 5.15: Energy dependent  $\gamma$ /hadron cut with 80% efficiency of the All-sky MC node (zenith  $32.059^\circ$ , azimuth  $102.217^\circ$ ).

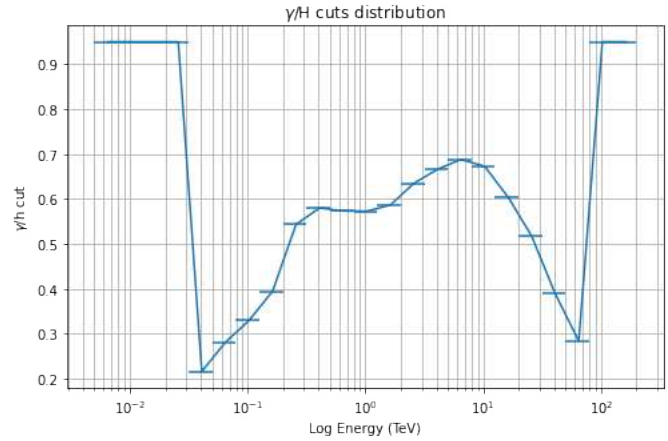


Figure 5.16: Energy dependent  $\gamma$ /hadron cut: *gammaness* as a function of energy for a  $\gamma$ -ray selection efficiency of 90% (zenith  $32.059^\circ$ , azimuth  $102.217^\circ$ ).

to `lstchain_create_irf_file`.

The  $\theta$  cut has been always fixed to **0.2 degree** (global cut). On the other hand, two different analyses have been carried on: global cut on  $\gamma$ /hadron of 0.7 and energy-dependent *gammaness* cut.

The latter (explained in 4.3.1) has been performed with a  $\gamma$ /hadron efficiency of 0.90, a minimum cut of 0.1 and a maximum one of 0.95.

A comparison between the  $\gamma$ /hadron energy dependent cut IRFs with 80% and 90% is showed in the 5.15 and 5.16 plots. It is reasonable to see harder cuts for the 90% IRFs for intermediate energies.

Fixing the efficiency to 0.90 in figure 5.18 some of the produced IRFs in the 1ES1959+650 analysis (it is observed mainly at high zenith angles, as shown in figure 5.2) are drawn together. From the plot different shapes of the zenith angles couples ( $32^\circ$ ,  $42^\circ$ ) and ( $53^\circ$ ,  $60^\circ$ ) are visible. It is an expected behaviour, as a matter of fact, the high-zenith angle observations are exploited to observe at higher energies.

This peculiar property is confirmed also by the effective area plot in dependence of the zenith angle 5.17: the higher is the zenith, the higher effective area, so the higher performances in detecting higher energy  $\gamma$ -rays. Consequently, at high zenith, the lower energy events have a worse resolution: the primary  $\gamma$  or cosmic ray interacts farther from the telescope and the particles produced and the Cherenkov light emitted traverse more atmospheric depth.

By interpolating or simply using the nearest IRF (it depends on the coordinates in 4.9 grid), one creates the DL3 files. The directory containing IRF files in FITS format has to be specified, such as the configuration file in which *EventSelector* acts by applying some conditions on DL2 Hillas parameters. In this analysis, for instance, the filters are on *intensity*, *width* and *length*, that have to be positive, on the event type, cosmic ray. After that the DL3 files are grouped as before per year and the HDU and observation files are created, ready for the higher analysis stages.

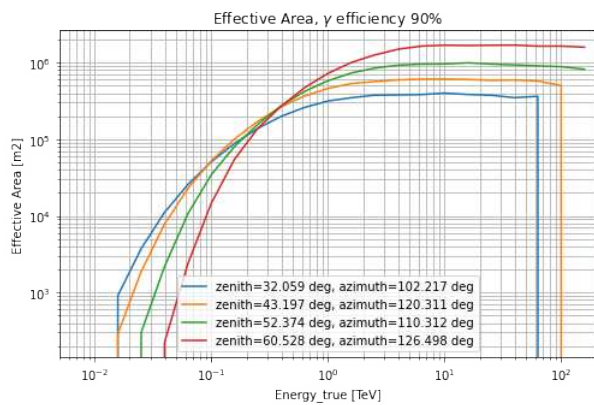


Figure 5.17: For the energy-dependent *gammaness* cut, the effective area in dependence on the energy for 4 different nodes.

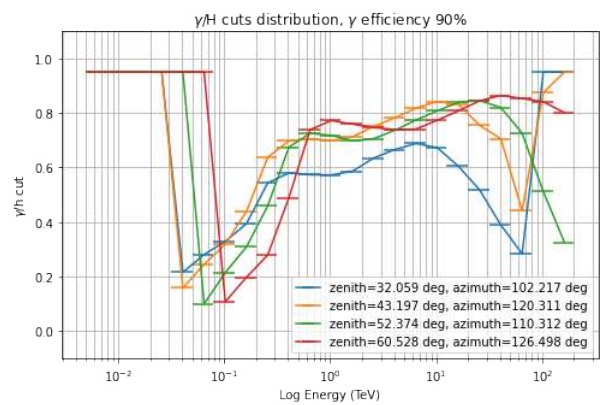


Figure 5.18: Energy-dependent  $\gamma$ /hadron cuts for different combination of zenith and azimuth angle. The minimum and maximum true energies are respectively 0.005 and 200 TeV and 5 bins per decade.

# Chapter 6

## Results of 1ES1959+650 analysis

This section covers the reconstruction of the VHE spectrum and light curve from 1ES1959+650, as measured by LST1. The steps examined in 4.5 have been followed to organize and analyse DL3 data. As already written in the previous sections, a first analysis is performed on data grouped per year. Then, the total observation dataset is analysed.

Before that, a selection on the runs reported in appendix A is applied: it is based on the observation mode, maximum zenith angle, minimum livetime and source name. The first constraint is placed to Wobble mode: for instance, some of the 2020 data are in ON/OFF mode and so they have been ruled out.

From the legends of figures 6.1, 6.2 and 6.3, showing the source regions and the background ones, the survived runs respectively of 2020, 2021 and 2022 can be seen.

The background regions are chosen as the standard Wobble position: each run has its own OFF circle in one of the four Wobble typical location. The ON region is of 0.2 deg as specified in section 5.3. ON and OFF regions have the **same** size and shape. No masks are applied since there are not disturbing  $\gamma$ -ray sources in the nearby of 1ES1959.

### 6.1 Spectral modeling and fit of high level data

Before all, the energy bins and the proper MapAxis objects for the true and reconstructed energies are created. The energy edges of this analysis are in the range 0.01-40 TeV, with a number of bins per decade of 5. The true energy bins have a minimum value of 0.01 TeV and a maximum of 100 TeV, 10 bins per decade.

The calculation of spectrum flux points requires as basic ingredients a measurement of the distribution of excess events as a function of energy, the exposure (product of the effective observation time and effective area of the instrument<sup>1</sup>) and the estimate of the migration of events from their true energies to their reconstructed ones. A check on each run is made through the **excess**, **exposure** and **energy migration plots**. The plots related to 2380 run (contained in 2020 dataset) are reported just as an example in figure 6.4. This run has a livetime of 469.9 s. From such graphics, one can infer that a high exposure is achieved in the range 100 GeV-50 TeV. Moreover, reconstructed and true energies are in a quite well-defined linear relation, although a slight fuzzy feature is visible at low energies.

The run excesses are between 150 GeV and 5 TeV: to notice is the fact that no excess counts with respect to the background are observed between 2 and 3 TeV.

The behaviors of **excesses** and **TS values** for the 3 datasets in dependence on the effective observation time are shown in the cumulative plots 6.5, 6.6 and 6.7. The larger the livetime, the larger excess and TS trend can be seen from almost all the plots. Exceptions are spotted in

---

<sup>1</sup>As shown in figure 5.17, the effective area depends on the energy.

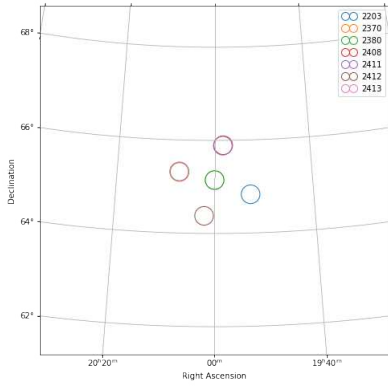


Figure 6.1: At the centre the source region: surrounded by the four Wobble background regions [14]. In legend the selected runs: the total livetime of Wobble observations is of 1.452 hours (the livetime of all observations selected in 5.1 was of 3.265 hours).

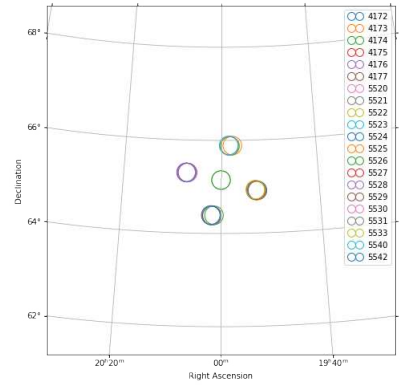


Figure 6.2: Wobble mode regions of 2021 data. The ON region at the centre, surrounded by the OFF ones. Total livetime: 4.94 hours.

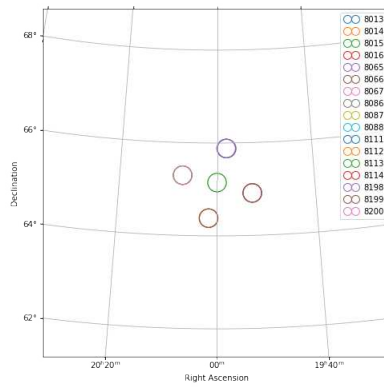


Figure 6.3: Total livetime of 2022 data is 4.78 hours. Wobble canonical positions (source position at the centre and the four OFF regions are surrounding it).

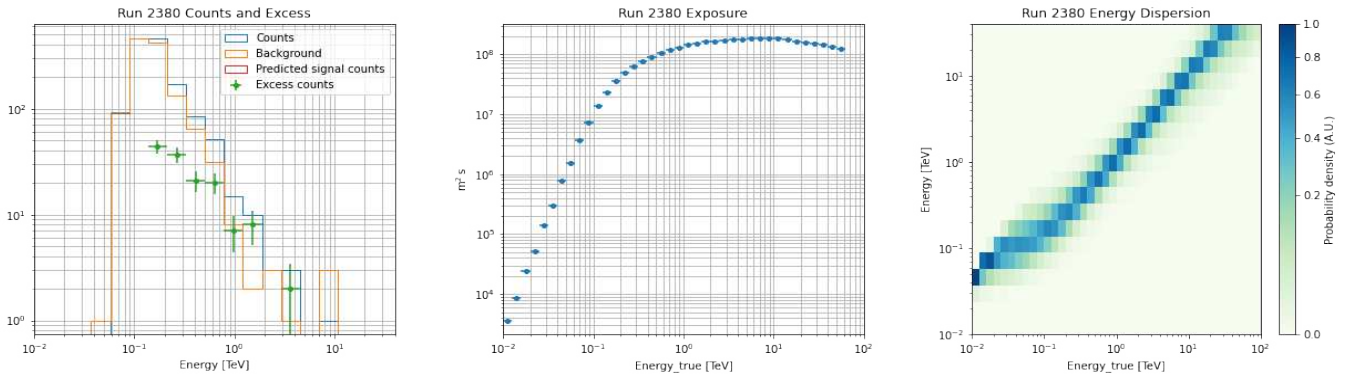


Figure 6.4: (left) Excess plot of run 2380. The counts and the background are computed for each energy bin; from them the excess are computed with the related uncertainties. The predicted signal has not been computed. (middle) Exposure related to the true energy. (right) Energy migration plot, reconstructed energy vs true one.

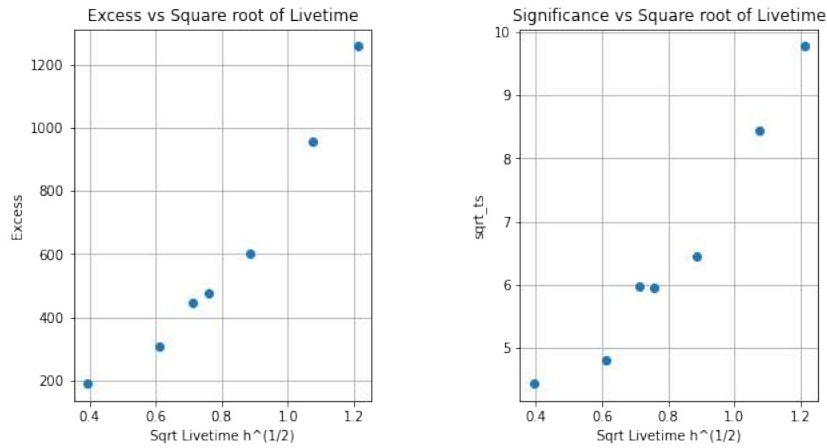


Figure 6.5: (*left*) Cumulative number of excess events as a function of the square root of the livetime for the 2020 dataset. (*right*) Cumulative significance detection of 2020 runs *vs* square-rooted livetime.

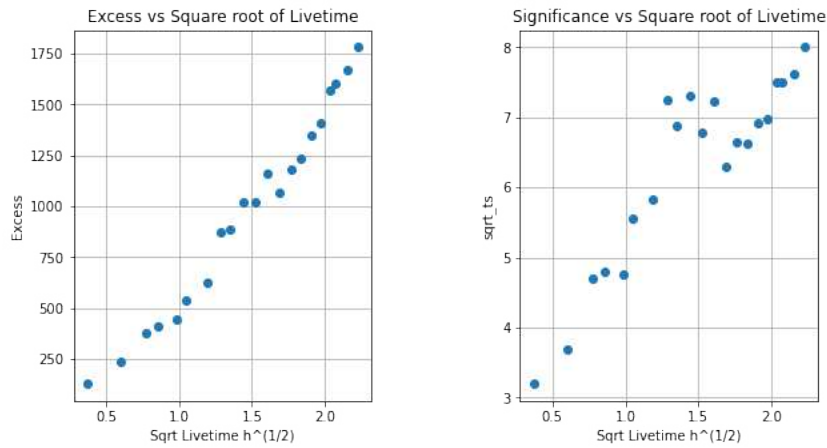


Figure 6.6: Cumulative plots of 2021 dataset excess (*left*) and significance (*right*) in dependence on the square-rooted livetime.

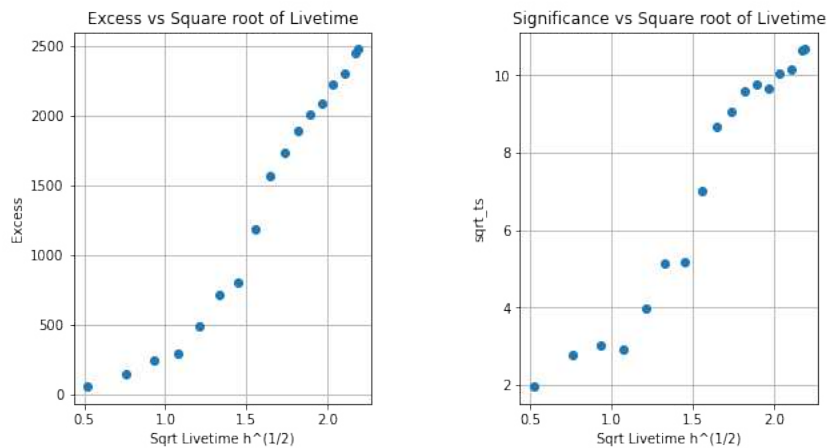


Figure 6.7: Cumulative plots of 2021 dataset excess (*left*) and significance (*right*) in dependence on the square-rooted livetime.

the 2021 dataset plot. For a constant emitting source, the detection significance (and therefore the TS) and the excess are expected to monotonically grow as the livetime increases. For variable sources, like the blazar 1ES1959+650, this is not necessarily true.

**Log Parabola spectral model** The model chosen to parameterise the spectrum is:

$$\phi(E) = \phi_0 \left( \frac{E}{E_0} \right)^{-\alpha - \beta \log\left(\frac{E}{E_0}\right)} \quad (6.1)$$

a "curved" Power Law function because of the energy dependent term in the exponential.  $\phi_0$  is the normalization factor, usually in  $cm^{-2} \cdot s^{-1} \cdot TeV^{-1}$ ,  $E_0$  is the reference energy,  $\alpha$  the spectral index and  $\beta$  the pre-factor of the natural logarithm term. For  $\beta = 0$  the Log Parabola model reduces to a simple Power Law one.

The method employed to fit LST1 data of 1ES1959+650 is the following:

- The stacked dataset of observation is fitted through a Power Law.
- From the estimated parameters, the decorrelation (or *pivot*) energy is computed (see appendix C.2). The decorrelation energy is the energy at which the error on the flux is the smallest, so the confidence band is the narrowest [8]. It is well defined in the Power Law model as in equation C.4.
- The stacked dataset is fitted by a Log Parabola model in which the reference energy is frozen to the decorrelation energy previously derived.
- Given the best model, the fit and light curves energy edges and the stacked dataset, the flux points are estimated.

**Spectral Energy Distributions** In the following the SEDs of the three subsets are reported in plots 6.8, 6.10 and 6.12. They are together with their residuals plots (figures 6.9, 6.11 and 6.13) to show that Log Parabola model reasonably reproduces the data. Such SEDs are produced by keeping the angular ON region radius at  $0.2^\circ$  and the *gammaness* cut at 0.7. They are compared to the results of fitting a Log Parabola model to Crab Nebula data from the MAGIC telescopes in 2009 to 2011 [11]. Upper limits are computed for bins with excess below a significance of  $2\sigma$  and the flux points errors are at  $1\sigma$ . In table 6.1 the fit results.

Parameter	2020	2021	2022	Total
$\phi_0 (cm^{-2} s^{-1} TeV^{-1} \cdot 10^{-10})$	$1.06 \pm 0.01$	$0.26 \pm 0.03$	$0.57 \pm 0.04$	$0.47 \pm 0.3$
$E_0 (TeV)$	0.45	0.60	0.51	0.52
$\alpha$	$2.6 \pm 0.1$	$2.5 \pm 0.1$	$2.5 \pm 0.1$	$2.55 \pm 0.07$
$\beta$	$0.16 \pm 0.10$	$0.26 \pm 0.14$	$0.31 \pm 0.09$	$0.25 \pm 0.07$

Table 6.1: Estimated Log Parabola parameters for the three years datasets with global cuts. In the last column, the ones obtained from the combined fit of all the selected observations available. As explained in the text, the reference energy of the Log Parabola is left frozen during the fit.

**Light Curves** The corresponding Light Curves are shown in the figures 6.14, 6.15 and 6.16 with run-wise and night-wise binning. The LC energy range is from 88.7 GeV to 40 TeV. From 2022 light curve of 1ES1959+650, one sees an intra-week flux variation peaked on the 3<sup>rd</sup> of May. At the peak of the flare, the flux reached  $(2.53 \pm 0.24) \times 10^{-10} (cm^{-2} s^{-1})$ , in the energy band specified in the legend of figure 6.16. The weighted average<sup>2</sup> of the 2022 light curve is of

<sup>2</sup>The formula is  $\bar{x} = \frac{\sum_i x_i \cdot w_i}{\sum_i w_i}$ , where the weight is taken as  $w_i = 1/\sigma_{x,i}^2$ . The error is  $\sigma_{\bar{x}} = \sqrt{\frac{1}{\sum_i 1/\sigma_{x,i}^2}}$ .

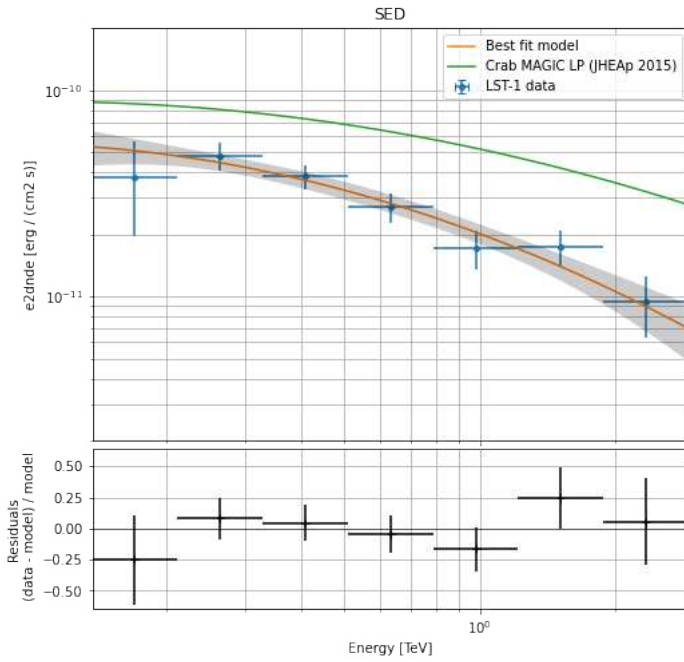


Figure 6.8: (*top*) SED generated from LST1 2020 observations.  $\theta$  and  $\text{gammaness}$  coefficient cuts fixed respectively to  $0.2^\circ$  and 0.7. Log Parabola fit is also presented with the error "zone" in grey 6.1. (*bottom*) LST1 SED residuals plot.

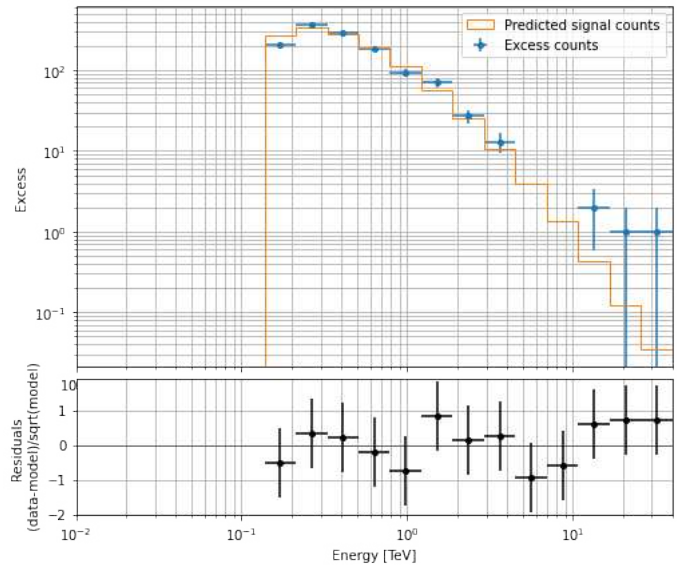


Figure 6.9: (*top*) Excess plot of the 2020 1ES1959+650 dataset: both the predicted signal counts and the detected ones are shown. (*bottom*) The spectral residuals from the ON region (they are divided by the square root of the predicted counts).

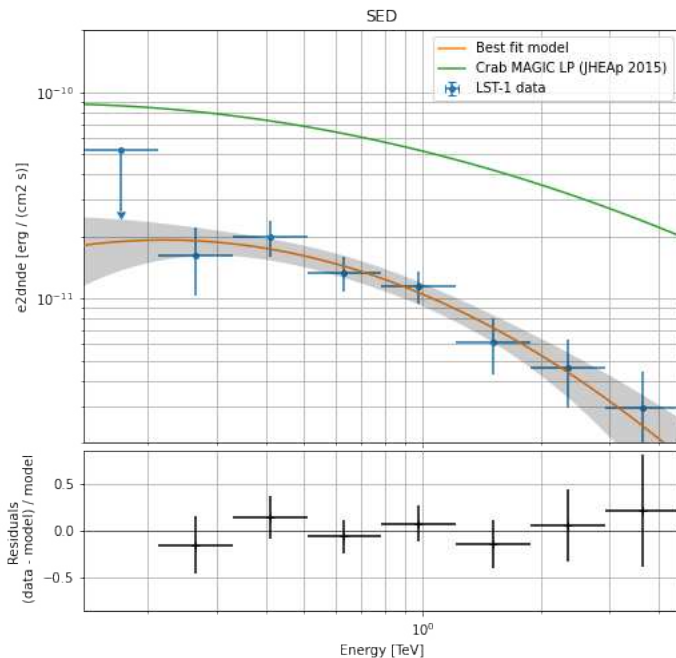


Figure 6.10: (*top*) SED from LST1 2021 observations of 1ES1959+650. ( $\theta$  and  $\text{gammaness}$  cuts fixed respectively to  $0.2^\circ$  and 0.7). Best Log Parabola fit is also presented with the error "zone" in grey 6.1. (*bottom*) 2021 SED residuals plot.

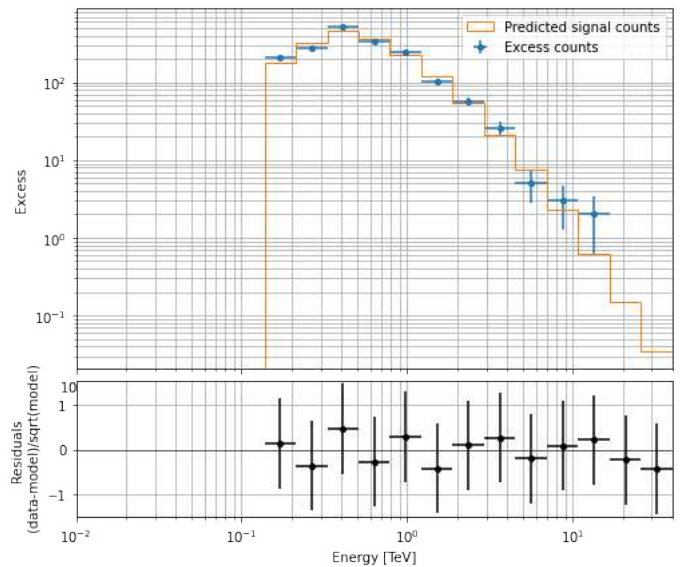


Figure 6.11: (*top*) Excess plot of the 2021 1ES1959+650 dataset: both the predicted signal counts and the detected ones are shown. (*bottom*) The spectral residuals from the ON region (they are divided by the square root of the predicted counts).

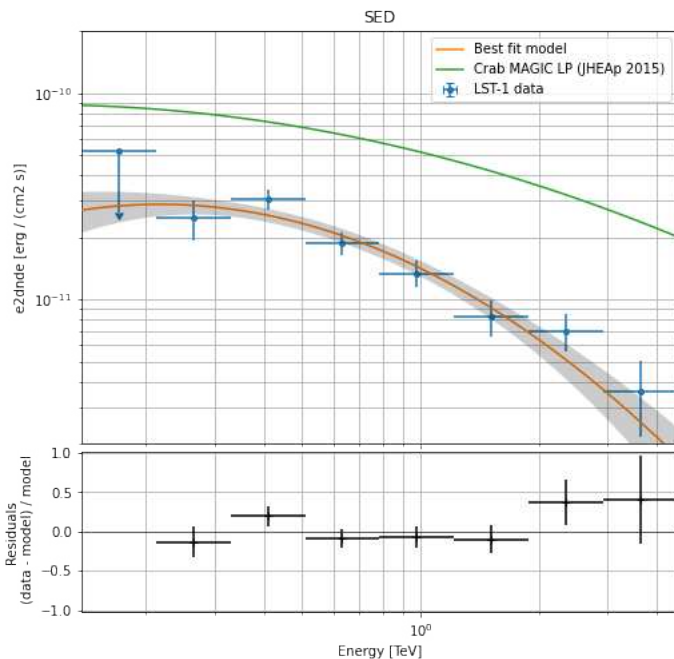


Figure 6.12: (*top*) SED from LST1 2022 observations of the blazar 1ES1959+650.  $\theta$  and  $\text{gammaness}$  coefficient cuts fixed respectively to  $0.2^\circ$  and 0.7. The best fit is also presented with the errors in grey 6.1. (*bottom*) SED 2022 residuals plot.

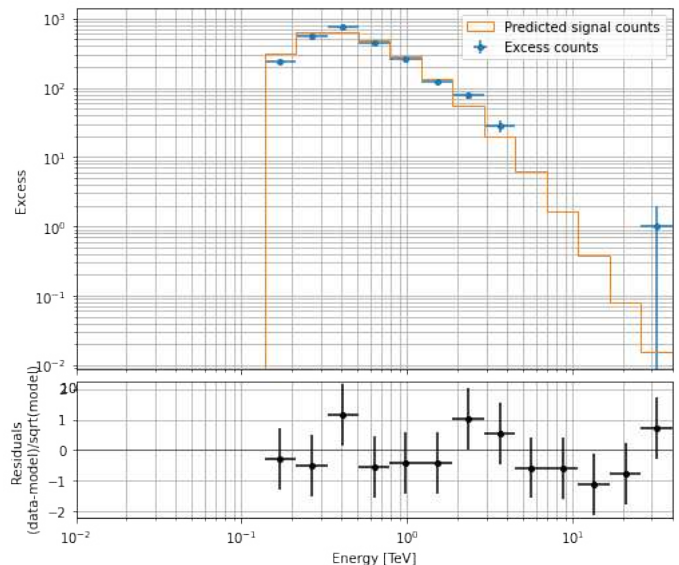


Figure 6.13: (*top*) Excess plot of the 2022 1ES1959+650 dataset: both the predicted signal counts and the detected ones are shown. (*bottom*) The spectral residuals from the ON region (they are divided by the square root of the predicted counts).

$$(1.65 \pm 0.10) \times 10^{-10} \text{ (cm}^{-2} \text{ s}^{-1}\text{)}.$$

Fluxes from LST1 can be compared to the ones obtained during the 2016 flare [44] (section 2.2.1 deals with this events). From those MAGIC observations ( $E > 300$  GeV), the estimated maximum fluxes are  $(4.06 \pm 0.13) \times 10^{-10} \text{ (cm}^{-2} \text{ s}^{-1}\text{)}$  on the 13<sup>th</sup> of June 2016 (its SEDs are reported in appendix B.2),  $(3.28 \pm 0.13) \times 10^{-10} \text{ (cm}^{-2} \text{ s}^{-1}\text{)}$  on the 14<sup>th</sup> and  $(3.76 \pm 0.08) \times 10^{-10} \text{ (cm}^{-2} \text{ s}^{-1}\text{)}$  on the 30<sup>th</sup>. LST1 maximum flux (between 300 GeV and 40 TeV) is of  $(0.56 \pm 0.06) \times 10^{-10} \text{ (cm}^{-2} \text{ s}^{-1}\text{)}$ ,  $\sim 7.5$  times fainter than the highest flux registered on the 13<sup>th</sup> of June 2016.

Neither by taking into account the flux points errors, there is not compatibility with a constant flux. It could be worthy to study it in more details, especially through a multiwavelength analysis (see later in the thesis section 6.5).

## 6.2 Total dataset: two years of observations

A more detailed analysis is presented on the whole dataset of 1ES1959+650 as observed by LST1; the methods are the same reported in section 6.1.

With reference to the estimated parameters in table 6.1 (last column), the **correlation matrix** is shown in figure 6.17: no special correlations between the model parameters can be inferred. In figure 6.18 the **differential spectrum** ( $dN/dE$ ) from the Log Parabola fit. It is a different visualization of the source spectrum.

The stacked predicted signal counts are computed per bin from the tool that creates the flux points. They are the predicted excess counts from the best fit hypothesis. They are plotted together with the excess counts in figure 6.20. At low energies ( $\gtrsim 150$  GeV) a good agreement between predicted and observed counts is spotted.

The total SED with the Log Parabola fit is in figure 6.19: the covered energy range is from  $\sim 100$  GeV to 4 TeV. In the same units of a SED ( $E^2 \cdot dN/dE$ ), the Test Statistic profile is plotted as a density plot in figure 6.21. Each flux point has its own statistic density, that follows

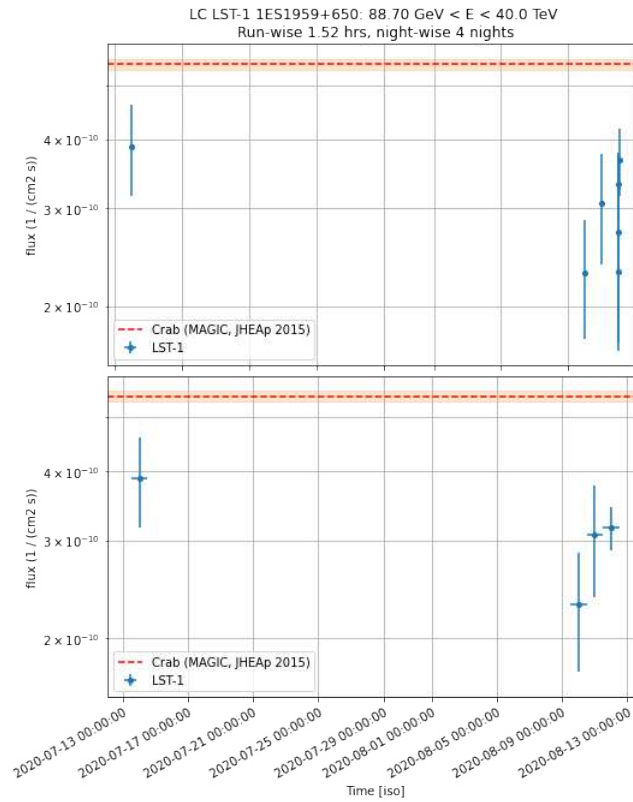


Figure 6.14: Light curve of 1ES1959+650 during the year 2020 as observed by LST1. (*top*) Run-wise flux points, (*bottom*) night-wise ones. In both they are compared to Crab flux with error, as detected by MAGIC in 2015.

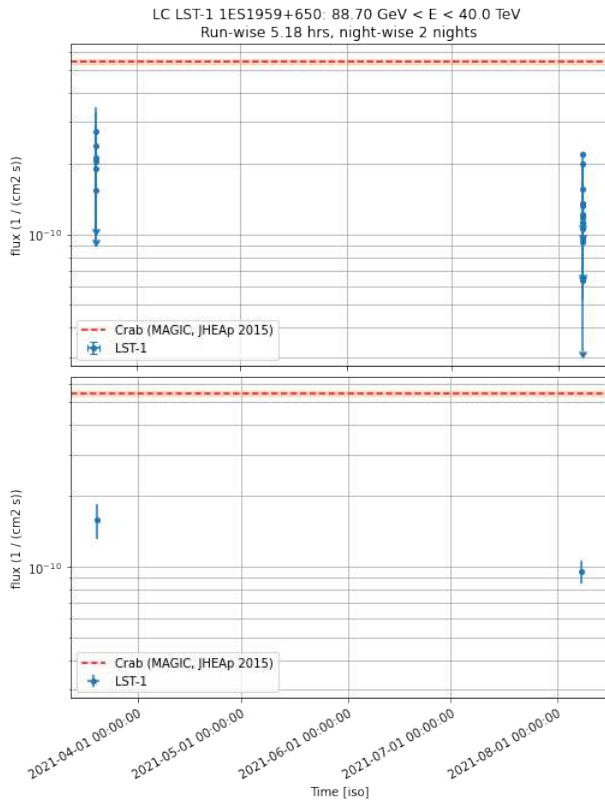


Figure 6.15: LST1 2021 Light Curve of 1ES1959+650: (*top*) run-wise flux points, (*bottom*) night-wise ones. They are compared to Crab flux (with its error).

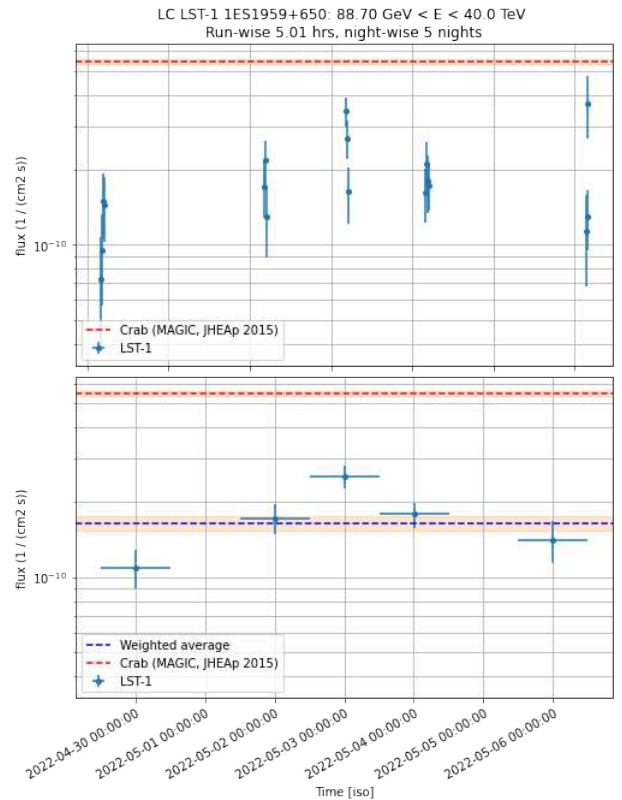


Figure 6.16: LST1 2021 Light Curve of 1ES1959+650: (*top*) run-wise flux points, (*bottom*) night-wise ones. They are compared to Crab flux (with its error).

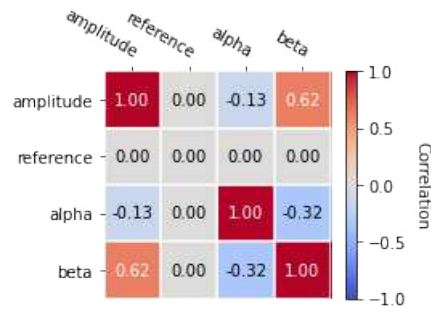


Figure 6.17: Correlation matrix between Log Parabola parameters computed from the fit of the entire dataset. The parameters' values and uncertainties are in 6.1.

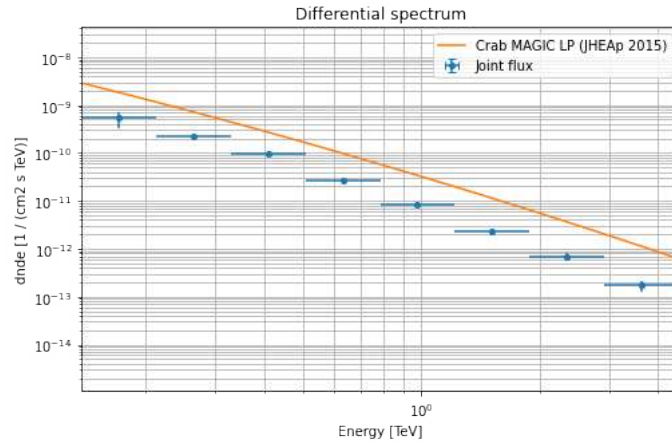


Figure 6.18: Differential spectrum of the joint analysis of all the runs. As usual it is compared to MAGIC Crab Log Parabola fit [11].

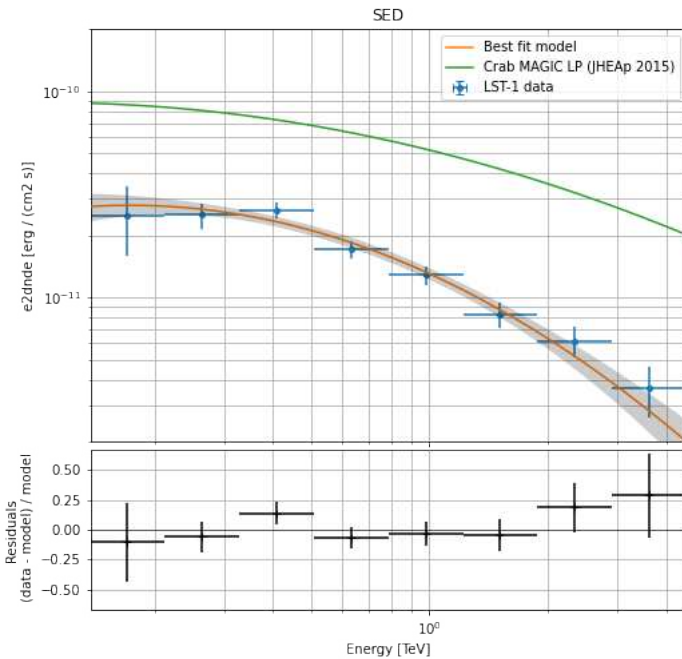


Figure 6.19: (top) Total dataset of 1ES1959+650 SED, applying global cuts, compared to Crab observation [11]. (bottom) Fit residuals.

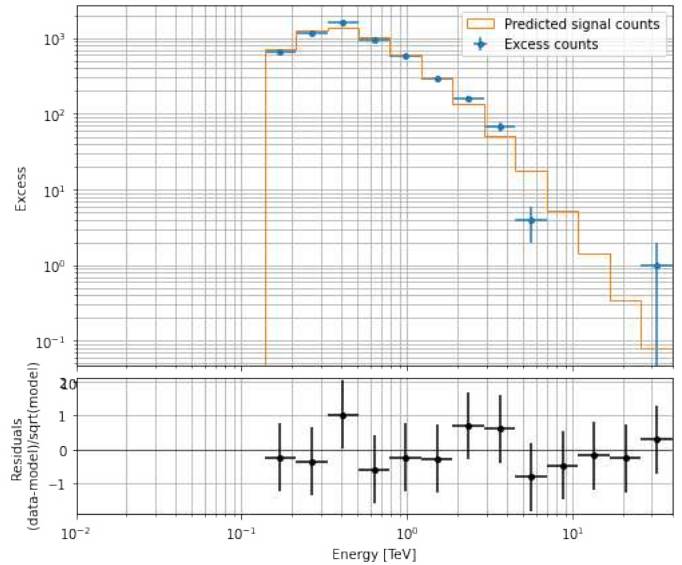


Figure 6.20: (top) Excess plot of the total 1ES1959+650 dataset: both the predicted signal counts and the detected ones are shown. (bottom) The spectral residuals from the ON region (they are divided by the square root of the predicted counts).

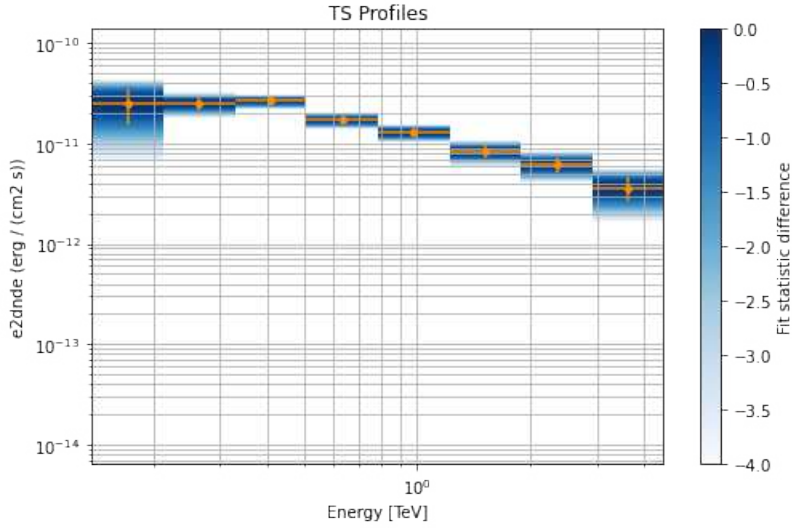


Figure 6.21: Test statistic density profile on the LST1 observations from 2020 to 2022. Global cuts have been applied.

the error bars.

### 6.3 Energy-dependent cuts to discern $\gamma$ -rays from protons

Until now, we have presented spectral fits obtained assuming fixed cuts on *gammaness* and  $\theta^2$ . However, the performance (PSF, energy resolution, hadron rejection power etc.) of the LST1 is energy-dependent, so it is natural to carry on the analysis with energy-dependent cuts on *gammaness*, using the properly-produced IRFs, as in section 5.3. The efficiency is set at 90%, and the maximum and minimum allowed cuts are respectively 0.95 and 0.1, like in figure 5.16. The results are shown in the following SEDs (2020 in figure 6.22, 2021 in 6.24, 2022 in 6.26 and the total in 6.28) for the four dataset analysed, together with the related residuals plots (respectively, figures 6.23, 6.25 and 6.27). The fit estimated parameters are contained in table 6.2.

Parameters	2020	2021	2022	Total
$\phi_0(cm^{-2}s^{-1}TeV^{-1} \cdot 10^{-10})$	$1.3 \pm 0.1$	$0.22 \pm 0.03$	$0.53 \pm 0.04$	$0.4 \pm 0.03$
$E_0 (TeV)$	0.42	0.65	0.53	0.56
$\alpha$	$2.5 \pm 0.1$	$2.5 \pm 0.1$	$2.5 \pm 0.1$	$2.52 \pm 0.08$
$\beta$	$0.26 \pm 0.13$	$0.26 \pm 0.13$	$0.334 \pm 0.99$	$0.29 \pm 0.07$

Table 6.2: Parameters with related uncertainties estimated from the Log Parabola fit of the four dataset analysed, computed with **energy-dependent  $\gamma$ /hadron cuts**. As usual, the reference energy is frozen to the previously obtained decorrelation energy value.

By looking at the SEDs produced with the two different approaches, one infers that, at lower energies, the flux is higher and agrees better with the model in the energy-dependent analysis of the three per-year datasets. It is also visible by comparing the residuals of the fit.

As the total SEDs concern, although the first flux points becomes an upper limit in the energy-dependent approach (it has a significance equals to 1.8), even in this case the first two points have an higher flux with respect to global-cut ones. To examine the upper limit in the total energy-dependent SED, the excess plot is reported in figure 6.29 and compared to the previously obtained excess plot 6.20. What is observed is that, in the energy-dependent case, the predicted

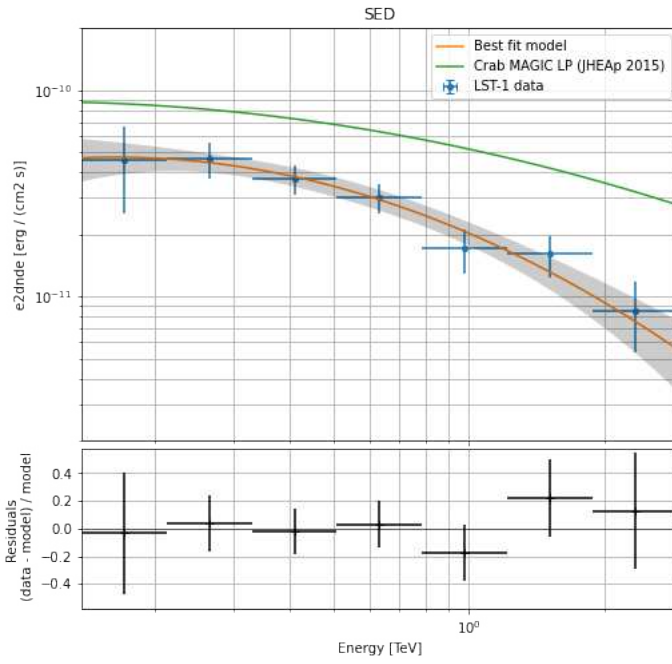


Figure 6.22: *(top)* Log Parabola SED from 2020 **energy-dependent  $\gamma$ /hadron cuts** dataset, compared to the reference Crab model. *(bottom)* Normalized residuals of the fit.

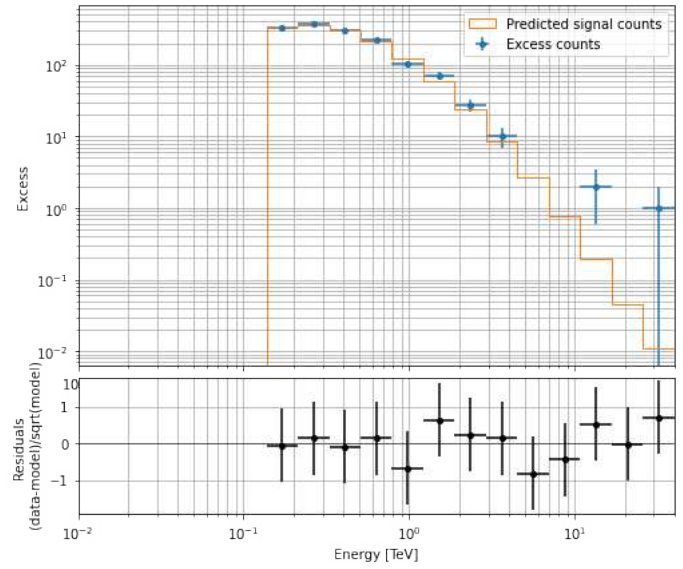


Figure 6.23: *(top)* Excess plot of the 2020 1ES1959+650 dataset **energy-dependent  $\gamma$ /hadron cuts**. Both the predicted signal counts and the detected ones are shown. *(bottom)* The spectral residuals from the ON region (they are divided by the square root of the predicted counts).

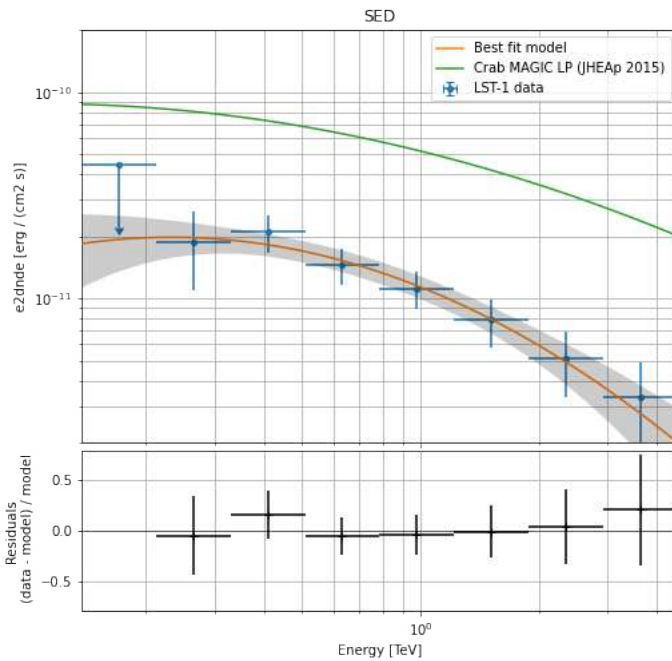


Figure 6.24: *(top)* Log Parabola SED from 2021 **energy-dependent  $\gamma$ /hadron cuts** dataset, compared to the reference Crab model. *(bottom)* Normalized residuals of the fit.

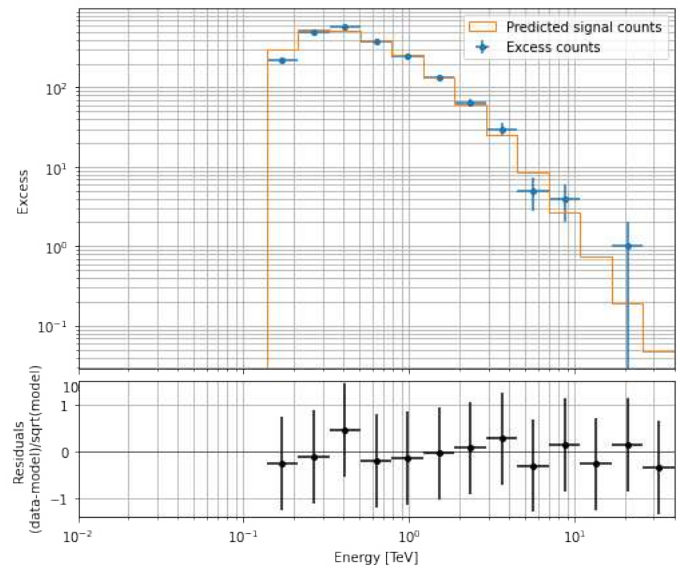


Figure 6.25: *(top)* Excess plot of the 2021 1ES1959+650 dataset **energy-dependent  $\gamma$ /hadron cuts**. Both the predicted signal counts and the detected ones are shown. *(bottom)* The spectral residuals from the ON region (they are divided by the square root of the predicted counts).

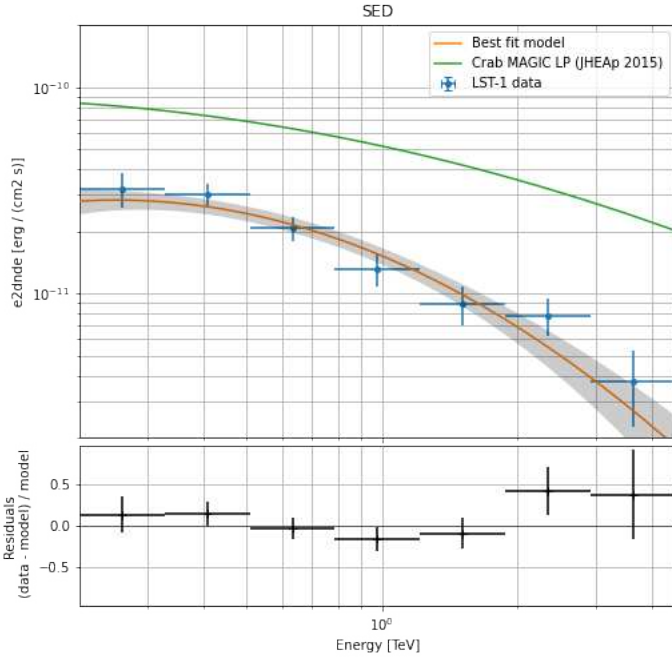


Figure 6.26: (top) Log Parabola SED from 2022 **energy-dependent  $\gamma$ /hadron cuts** dataset, compared to the reference Crab model. (bottom) Normalized residuals of the fit.

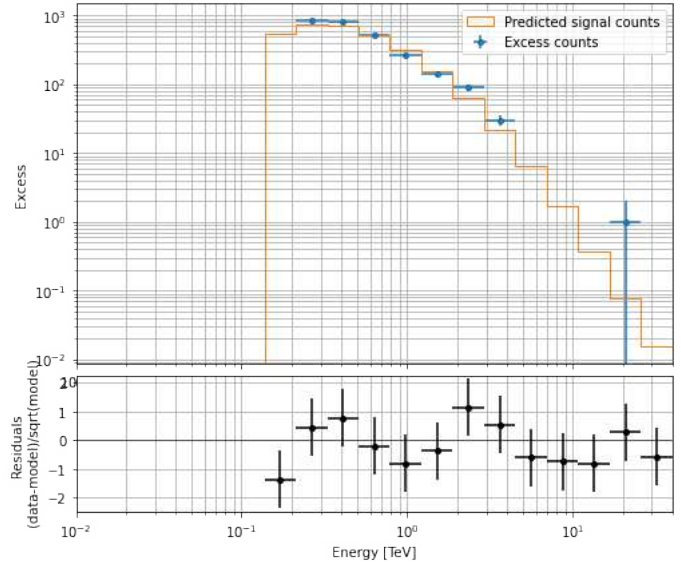


Figure 6.27: (top) Excess plot of the 2022 1ES1959+650 dataset **energy-dependent  $\gamma$ /hadron cuts**. Both the predicted signal counts and the detected ones are shown. (bottom) The spectral residuals from the ON region (they are divided by the square root of the predicted counts).

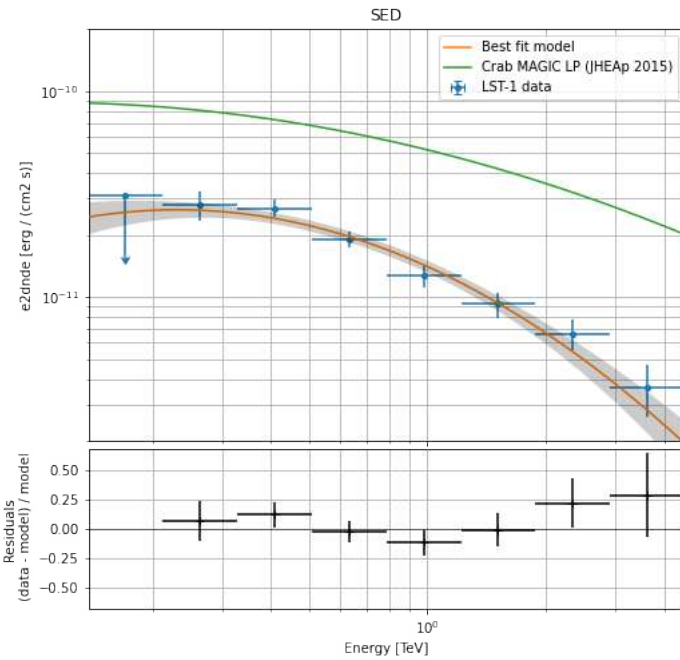


Figure 6.28: (top) Log Parabola SED from all LST1 observations of 1ES1959 in **energy-dependent  $\gamma$ /hadron cuts** dataset, compared to the reference Crab model. (bottom) Normalized residuals of the fit.

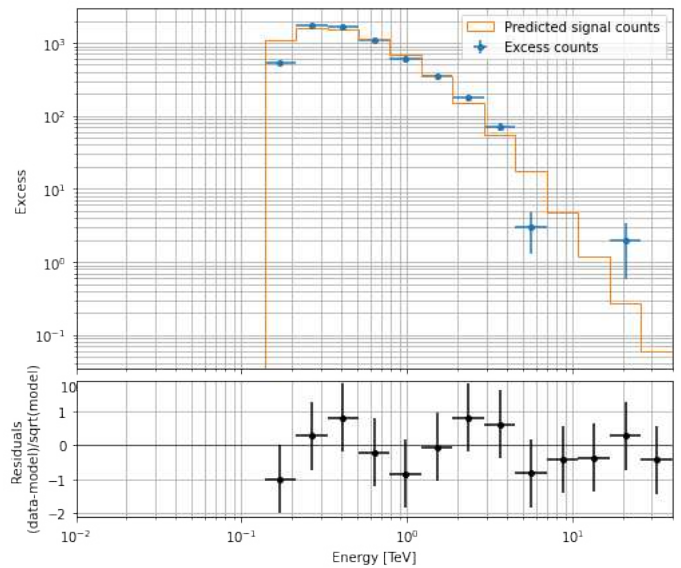


Figure 6.29: (top) Predicted signal counts and excess counts as computed from the total dataset with **energy-dependent cuts on gammaness**. (bottom) Residuals of the upper plot.

signal counts rises up with respect to the global cuts ones. However, the excess counts are the same in both. It could be the reason for obtaining such an upper limit in the energy-dependent approach.

## 6.4 Combination with Fermi-LAT observations

To broaden the knowledge about 1ES1959+650 and its emission properties, Fermi-LAT observations are analysed together with LST1 results. In figure 6.30, the Fermi counts map is reported with labelled the sources in the FoV.

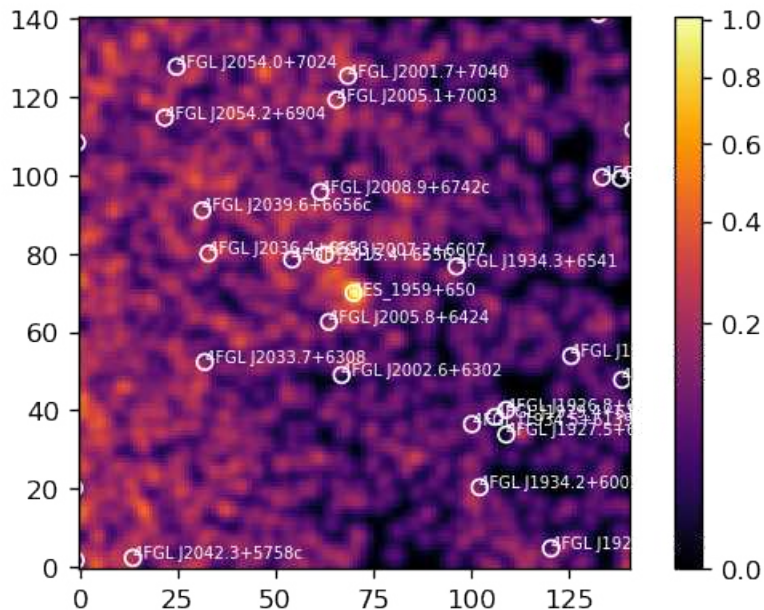


Figure 6.30: Fermi-LAT Field of view centred in 1ES1959+650. The other sources in the map are labelled.

In figure 6.31, LST1 SED and best fit (from figure 6.19) are superimposed with Fermi flux points and derived model. Both come from the observations in the period from 2020 to 2022: almost-simultaneous LAT and LST1 observations produce such SEDs.

On the other hand, all Fermi observations from the 1<sup>st</sup> of July 2020 to the 18<sup>th</sup> of May 2022 are shown and largely discussed in the forthcoming section 6.5. Fermi data reduction and fit are done with Fermi tools (`enrico` pipeline).

Parameters	Fit results
norm ( $cm^{-2}s^{-1}MeV^{-1}$ )	$5.49^{+1.08}_{-1.01}$
$E_0$ (MeV)	1390
$\alpha$	$1.68^{+0.18}_{-0.21}$
$\beta$	$0.065^{+0.077}_{-0.000}$

Table 6.3: Fit results of the Fermi SED in 6.31 (taking into account EBL absorption from [22]). Fermi data are in the energy range from  $3 \cdot 10^2$  to  $10^6$  MeV. Temporal range 59030-59724 MJD, taking the same observational nights of LST1. *Thanks to Dr. Mireia Nieves Rosillo for Fermi analysis through `enrico` pipeline and all Fermi-LAT data analysis.*

The two SEDs, in particular the best models, show an agreement, also in the region in which the two overlap (even if to confirm it one has to consider a larger observational time, especially for Fermi-LAT). It is a starting point to estimate the high energy peak in the blazar SED. More qualitatively, one can have a look at the output parameters of the fit: if Fermi spectral

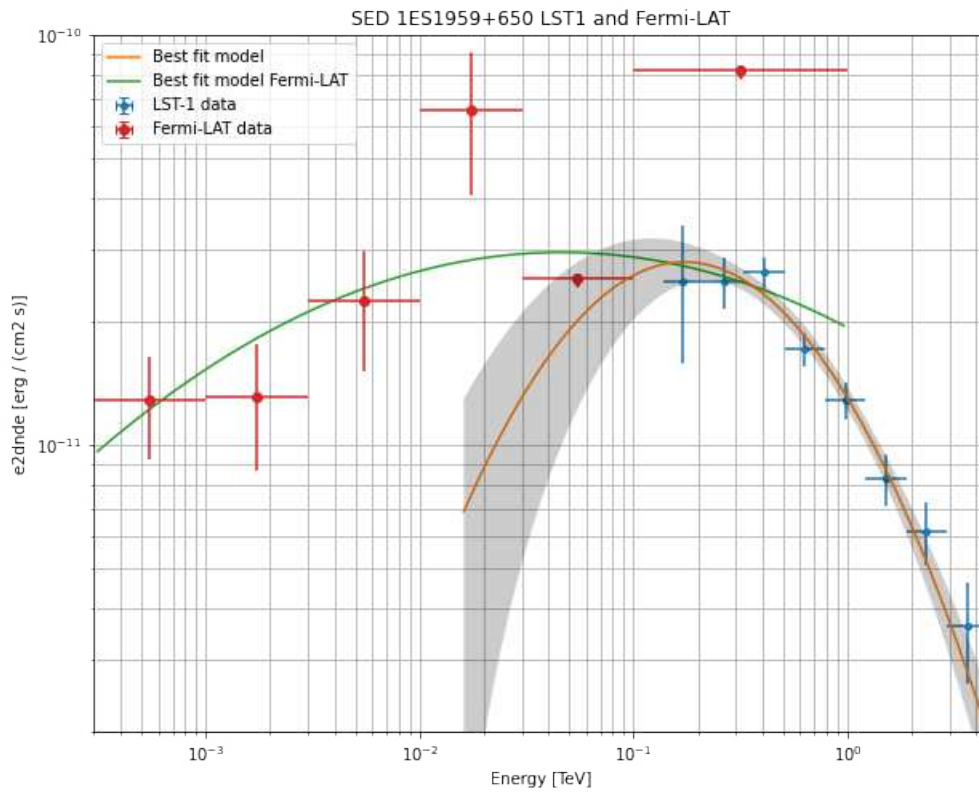


Figure 6.31: Fermi-LAT and LST1 (from figure 6.19) flux points and best Log Parabola fit models (LST1 fit parameters are in table 6.1). Fermi fit parameters are in table 6.3.

In this plot the Fermi data has been corrected for the Extragalactic Background Light (EBL) extinction [22]. However, at those energies and at 1ES1959+650's redshift, it does not relevantly affect the observations.

The last two Fermi points are **upper limits**. LST1 model contains also fit error region in *grey*.

index  $\alpha$  is smaller than 2, the peak is at higher energies than Fermi coverage range, so in the energies detected by LST1.

To notice is the fact that, in figure 6.31, LST1 fit model starts from  $\sim 0.015$  GeV: it is because the dataset has been fitted in the energy range 0.01547-40 TeV. However, the fit in the first energy bins, until 0.137 TeV, does not succeed, because of too low count numbers. The high zenith angle does not allow lower energy photon detection.

### 6.4.1 Broadband modelling of the $\gamma$ -ray emission

The flux points of plot 6.31 are fitted together through a Log Parabola function in figure 6.4. An intermediate fixed value of the reference energy ( $E_0$ ) is chosen<sup>3</sup>. The fitting method is the least squares<sup>4</sup> for the  $\phi_0$ ,  $\alpha$  and  $\beta$  parameters of equation 6.1.

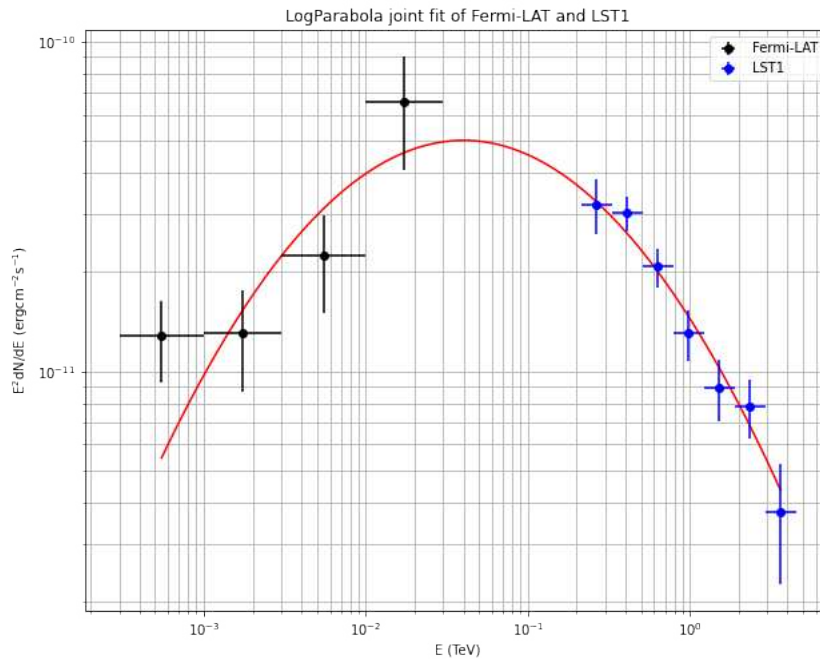


Figure 6.32: The same data of plot 6.31 considering  $1 \sigma$  Gaussian errors and rejecting upper limits are shown with the fitting curve (in red). The parameters values of the curve are reported in 6.4.

The resulting parameters are reported in table 6.4 with the  $\chi^2$  for 8 degrees of freedom.

Parameter	Fit results
$\phi_0 (cm^{-2} s^{-1} TeV^{-1} \cdot 10^{-11})$	$3.98 \pm 0.59$
$E_0 (TeV)$	0.01
$\alpha$	$-0.34 \pm 0.07$
$\beta$	$0.12 \pm 0.02$
$\chi^2$	9.2
$\chi^2_{red} (d.o.f.=8)$	1.15

Table 6.4: Results from the joint LogParabola fit of LST1 and Fermi-LAT (see equation 6.1). The reference energy ( $E_0$ ) is frozen to the value of 10 GeV. The  $\chi^2$  values are also provided.

A good  $\chi^2$  value outputs from the combined fit. Indeed, the reduced  $\chi^2$  is close to 1. The HE peak of the SED inferred from the fit is at  $\sim 40$  GeV, almost one order of magnitude lower

<sup>3</sup>As reported in tables 6.3 and 6.1 (last column), the reference energy employed in the Fermi-LAT SED is of  $\sim 1.3$  GeV whereas in LST1 fit  $\sim 510$  GeV. The criterium for choosing LST1 reference energies is explained in section 6.1.

<sup>4</sup>The Python `scipy` package has been employed.

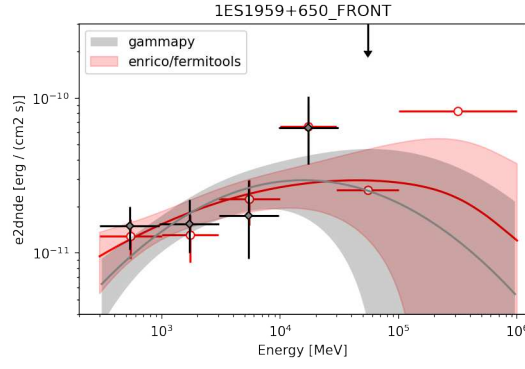


Figure 6.33: Fermi-LAT analysis with Gammapy compared to the results obtained with Fermi pipeline `enrico`. They are referred to only front events.

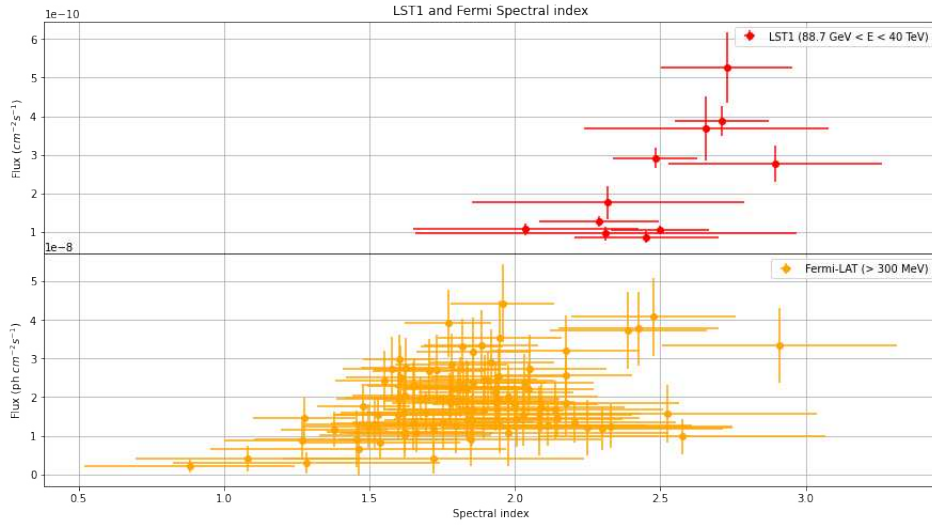


Figure 6.34: (top) LST1 flux *vs* spectral index ( $\alpha$  in the LogParabola equation 6.1). (bottom) Fermi-LAT data from the Light Curve in 6.39: flux *vs* spectral index.

that the energies peaks estimated in [44] (Table 1) during the flaring state of the blazar. However, more sophisticated techniques are required to consistently characterize the HE peak, for instance analysing both high level data through Gammapy. During this work, analysis of Fermi-LAT observations with Gammapy has been attempted<sup>5</sup>. It is a key point to fit the stacked Fermi and LST1 data. However, disagreements in the results Fermi’s pipeline and Gammapy analysis are still present, as shown, for example, in figure 6.33 (referring to only front Fermi events). In addition, once combined Fermi back and front data, issues arise from the LST1 and Fermi-LAT combined fit. It will be a deal of future works, useful to better characterize the high-energy peak position.

## 6.4.2 Dependency of the spectral index on the source flux

With reference to the light curve showed in 6.39 (next section), for each LST1 and Fermi flux point the spectral index has been plotted against the fluxes (figure 6.34).

To investigate on spectral index evolution<sup>6</sup>, in figures 6.35 and 6.37 LST1 and Fermi-LAT data, respectively, have been fitted through a simple linear function ( $y = a \cdot x + b$ ). In the Fermi-LAT sample, four data of no-detection of the source have been removed. The fit results and  $\chi^2$  values

<sup>5</sup>In the Fermi-LAT case a 3D analysis has to be performed with Gammapy, i.e. considering all the sources in the FoV (see the counts map 6.30).

<sup>6</sup>”Harder when brighter” or ”softer when brighter” are usually inferred from AGNs emission observation from X- to  $\gamma$ -ray observations (see for instance [9]).

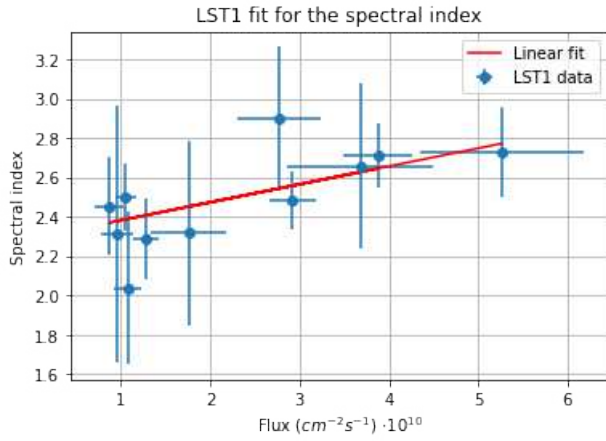


Figure 6.35: Linear fit of the spectral index obtained from LST1 observations.

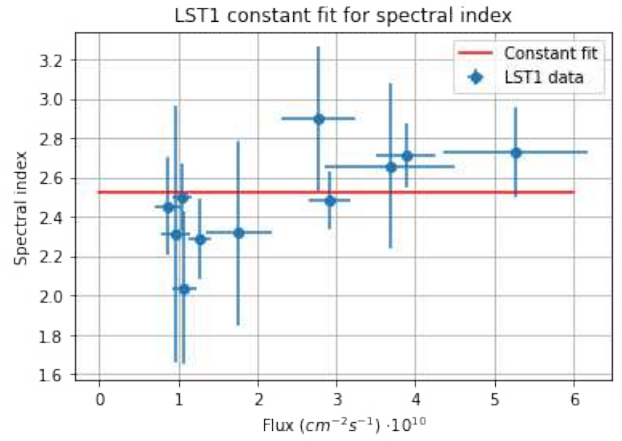


Figure 6.36: LST1 spectral index points fitted by a constant function.

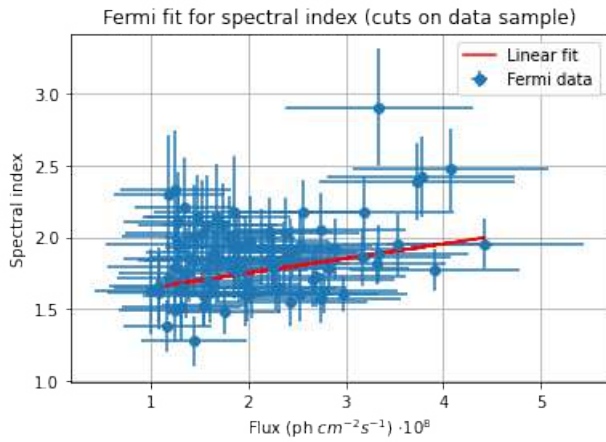


Figure 6.37: Linear fit of Fermi 1ES1959+650 detection and spectral indexes obtained.

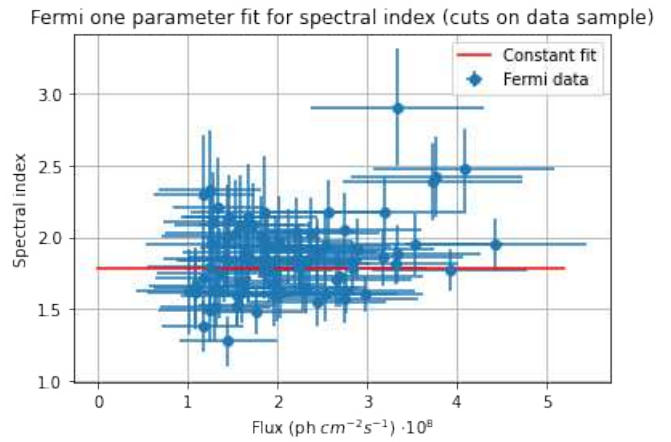


Figure 6.38: Same data sample of 6.37, this time fitted through a constant function.

are reported in table 6.5.

Parameters	LST1	Fermi-LAT	LST1 const.	Fermi const.
$a$ ( $cm^2s$ )	$0.09 \pm 0.03$	$0.12 \pm 0.03$	/	/
$b$	$2.29 \pm 0.09$	$1.51 \pm 0.07$	$2.53 \pm 0.06$	$1.77 \pm 0.03$
$\chi^2$	3.2	40.0	6.7	111.2
$\chi_{red}^2$	0.35	0.43	0.67	1.18
d.o.f.	9	93	10	94

Table 6.5: Resulting parameters from the fit linear function showed in figures 6.35 and 6.37. It contains also the results from the constant fits of figures 6.36 and 6.38.  $\chi^2$ ,  $\chi_{red}^2$  and degrees of freedom are also reported to evaluate the fit goodness.

In both fits the  $\chi_{red}^2$  is smaller than one: it could be likely due to the large error bars for the spectral indexes in both observations. However, in any case both show a positive slope ( $a > 0$ ): it could be a hint for "softer when brighter" source behaviour. It means that the higher flux, the higher spectral index is obtained from fitting the data.

To consistently evaluate if 1ES1959 follows this evolution, it is interesting to compare the linear fit results to the constant fit ones ( $y = b$ ). The fit lines are reported in figures 6.36 and 6.38, whereas the results are in the last two columns of table 6.5.

For LST1 sample the constant fit  $\chi_{red}^2$  increases as well as Fermi one (it is larger than 1). By

taking a look at figure 6.36, it seems that the constant model agrees within the errorbars with most of LST1 points.

## 6.5 Multiwavelength light curve of the blazar

LST1 observations of the BL Lac object 1ES1959+650 have been put in a broader context by examining its light curve together with other telescopes and instruments detection. In figure 6.39 the light curves of LST1, Fermi-LAT, *Swift*-XRT (introduced in section 3.3.2) [63] and TELAMON (section 3.3.3) [34] are plotted with the aim of spotting any possible interesting and peculiar feature. Finding correlations between different energies could be a way to probe physical models that explain such an observed emission. If the fluxes vary simultaneously or with a certain relative delay, the emissions in different wavelength can be traced back to the same processes. An example of such an analysis has been reported in 2.2.1.

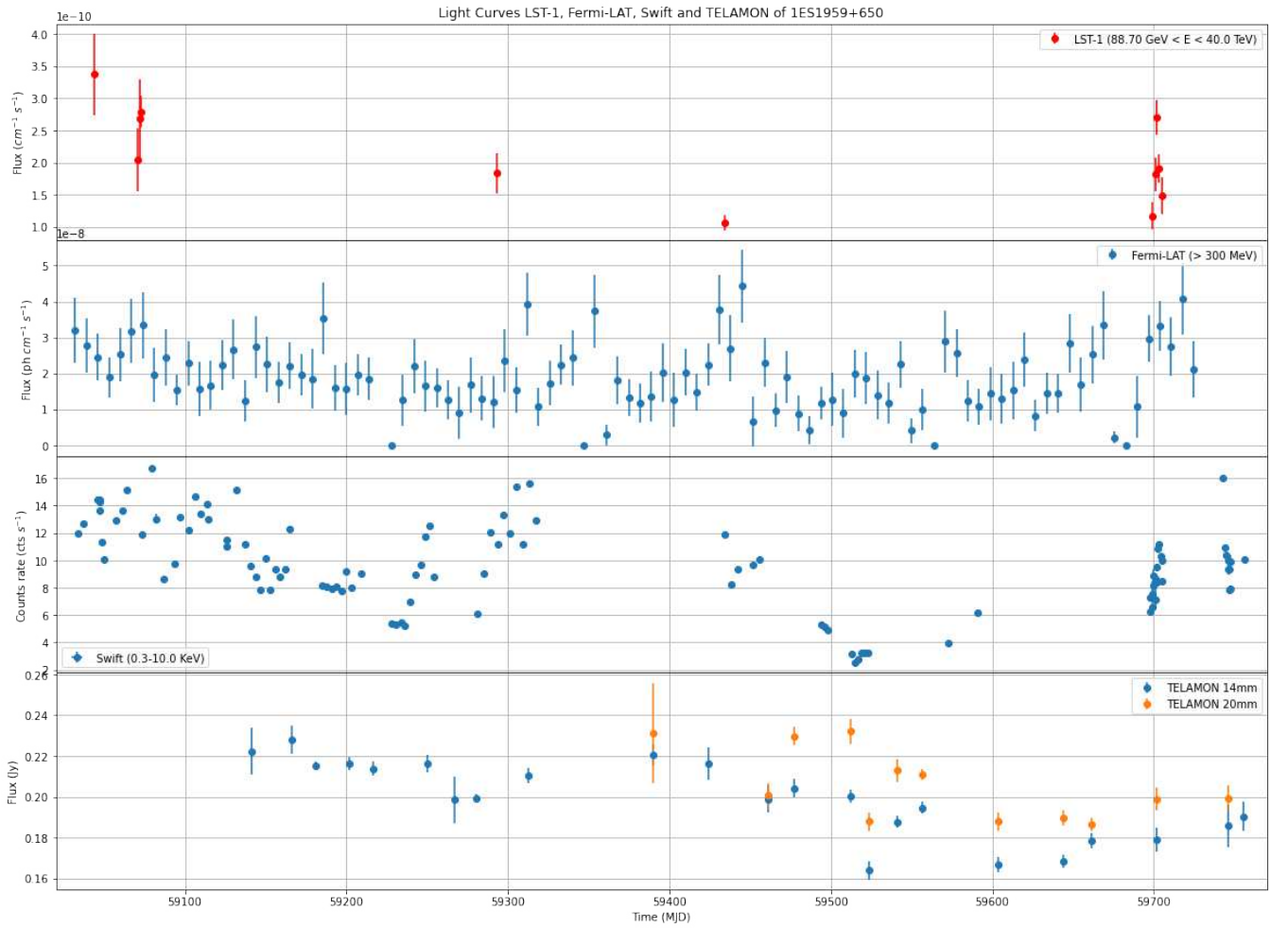


Figure 6.39: 2020 to 2022 1ES1959+650 observations. From the top: (*Panel 1*) LST1 night-wise flux points between 88.7 GeV and 40 TeV (joint light curve of figures 6.14, 6.15 and 6.16). (*Panel 2*) Fermi-LAT observations from 59034.5 MJD to 59727.5 MJD in the energy band from 300 MeV to  $10^6$  MeV. The time binning is of 7 days. (*Panel 3*) *Swift*-XRT count rates in the range 0.3-10 KeV [63], from 53479.3 MJD to 59768.6 MJD. The time binning varies from  $\sim 0.3$  to  $\sim 0.0005$  MJD. The rates are obtained by removing background counts and correcting the PSF; the errors on them are of  $1 \sigma$ . (*Panel 4*) TELAMON radio observations: averaged flux density (equation 3.1) for 20 mm and 14 mm. 7 mm data is very limited: it is difficult to derive the spectral indexes and no significant results can be extracted [34]. *Thanks to the researchers involved in TELAMON project for the radio data.*

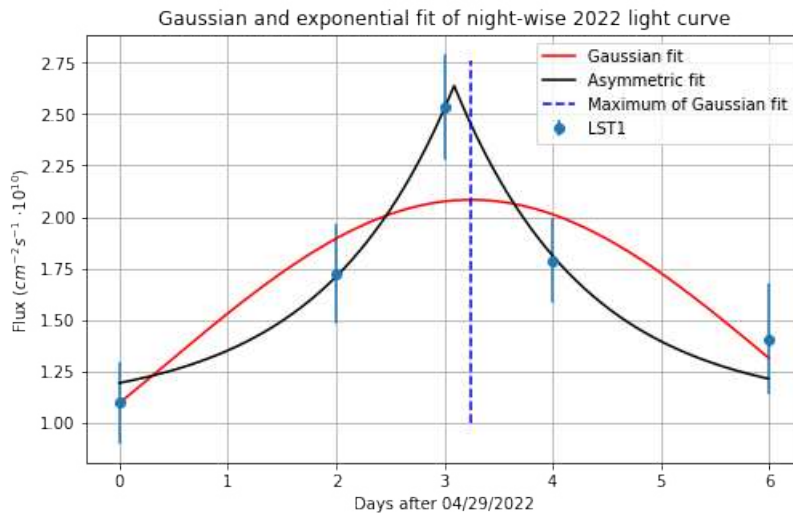


Figure 6.40: Night-wise LST1 2022 light curve of 1ES1959+650 fitted through a gaussian-like function (from 6.16 *bottom*). In *red* the profile obtained from the fit; the blue dashed line corresponds to the  $\mu$  value (in table 6.6) of the gaussian function. The *black* line is the exponential fit.

**Intra-week flare characterization** It is worthy to notice that an interesting rising in 1ES1959+650 flux detected by LST1, Fermi and *Swift*-XRT is *almost*-simultaneously observed in correspondence of the end of April/beginning of May 2022. As radio observations regard, no relevant differences can be spotted<sup>7</sup>. Nevertheless, radio variability cannot be excluded in shorter timescales, e.g. close to the LST1 observations. It would require a more serial monitoring of the source.

Trying to investigate deeper in this feature, in the following a zoom of the night-wise 2022 LST1 light curve is shown. The flux points are fitted by a gaussian function of the form:  $y = norm \cdot exp(-(x - \mu)^2 / (2 \cdot \sigma^2))$ . The fit curve is shown in figure 6.40 and the results are reported in table 6.6.

Parameters	Fit results
$\mu$ (days)	$3.2 \pm 0.5$
$\sigma$ (days)	$2.9 \pm 0.7$
norm ( $cm^{-2}s^{-1} \cdot 10^{10}$ )	$2.1 \pm 0.2$
$\chi^2$	4.9
$\chi_{red}^2$ (d.o.f.=2)	2.4

Table 6.6: Results of the gaussian fit of 1ES1959 flux points from 2022 LST1 observations.

Parameters	Fit results
$t_0$ (days)	$3.1 \pm 0.2$
$\Delta t_{r/d}$ (days)	$1.2 \pm 0.9$
$\phi_0$ ( $cm^{-2}s^{-1} \cdot 10^{10}$ )	$1.6 \pm 0.4$
$\phi_{baseline}$ ( $cm^{-2}s^{-1} \cdot 10^{10}$ )	$1.1 \pm 0.3$
$\chi^2$	0.76
$\chi_{red}^2$ (d.o.f.=1)	0.76

Table 6.7: Results of the exponential fit of 1ES1959 flux points from 2022 LST1 observations.

In any case, the flux rising/falling timescales are not the same in real cases. Intensity increasing depends on the particles acceleration mechanisms, whereas its declining is commonly attributed to particles' cooling processes. So a symmetric function does not generally provide a reliable picture. For this reason a further asymmetric fit has been performed.

The fit function is [44]:

$$\phi(t) = \phi_0 \cdot e^{-|t-t_0|/\Delta t_{r/d}} + \phi_{baseline} \quad (6.2)$$

<sup>7</sup>As the radio light curve concerns, it is interesting to notice how 14 mm fluxes are always higher than 20 mm ones. It is in agreement with the phenomenological model introduced in 2.1 and in particular the profile of radio emission (equation 2.1), with a negative spectral index,  $\alpha_R$ . However, as the difference between the two averaged fluxes changes in time, one can infer how the spectral index varies.

where  $\phi_0$  is the normalization factor,  $t_0$  the time at which it reaches the maximum,  $\Delta t_{r/d}$  is a the characteristic timescale of the rising/falling flux<sup>8</sup> and  $\phi_{baseline}$  is a flux shift. The fit results are reported in table 6.7, and the resulting function is superimposed to the light curve in figure 6.40. Comparing the two  $\chi^2$  the exponential function surely better fits the data, even if the sample is still poor, only five flux points. The reduced- $\chi^2$  of the asymmetric fit is slightly smaller than one.

As usually done in quantifying the intrinsic variations in blazar light curves, although the poor statistical sample, the **fractional variability amplitude**,  $F_{var}$ , is computed with its uncertainty [54] (the formulas are in appendix C.4).  $F_{var} = 0.29 \pm 0.07$  is the outcome and reveals a quite large variation in the one day light curve in 2022 LST1 data, considering the source to be variable wether  $F_{var} > 3 \times err(F_{var})$  [54].

---

<sup>8</sup>Information on how the rising/falling timescale can be estimated is in [44].

# Chapter 7

## Conclusions

### 7.1 Summary

The work presented in this thesis is composed of seven chapters.

The introduction, chapter 1, delineates the context of AGNs and VHE  $\gamma$ -ray observations. Moreover, the thesis aims are stated. Chapter 2, is a detailed review on Blazars with an emphasis on  $\gamma$ -ray astronomy studies. It also deals with previous investigation on the blazar 1ES1959+650 and attempts of modelling the most extreme states of its emission (section 2.2.1). The unresolved mysteries dealing with blazars are presented.

Chapter 3 introduces the reader to the first Large-Sized Telescope of CTA, LST1. It is put in context with the future telescopes of CTA North site in La Palma, Spain, section 3.2. In the same chapter other instruments detecting photons at lower energies than LST1 are briefly described in section 3.3. Those are Fermi-LAT, *Swift*-XRT and TELAMON radio project.

A description of LST1 data analysis is introduced in chapter 4. It gives a picture on the current pipeline developed up to date, from raw data to scientific products.

In chapter 5, data reduction procedures are applied to the observations of 1ES1959+650 performed from 2020 to 2022 by LST1. Checks on each step are presented and discussed.

Lastly, in chapter 6, high-level analysis products are shown and examined. These are the basis to infer the physical emission properties of the source. LST1 observations of 1ES1959+650 are put in a Multiwavelength context in sections 6.4 and 6.5.

### 7.2 Results and future perspectives

As the LST1 analysis pipeline concerns, despite the advances achieved so far by many researchers and developers involved, some issues and pipeline's branches are still open.

In particular, the **new IRFs interpolation** is still being implemented and tested<sup>1</sup>.

Another interesting part to be developed is the **joint analysis of MAGIC I-II and LST1**. There is an ongoing effort to implement LST1+MAGIC joint analyses, but this requires an important effort in translating MAGIC MCs to a format that meets the standards of CTA. It will bring to better performances among the IACTs in the northern hemisphere [46].

The current version of **magic-cta-pipe** starts from DL1 stage: among lots of peculiarities, it exploits, for instance, stereoscopic parameters in the events reconstructions, such as the **disp** one (depicted in 7.1 sketch). Optimization of the time and direction coincidences are still under debate, as well as the Response Functions for the energy reconstructions and *gammaness* cuts<sup>2</sup>.

---

<sup>1</sup>Have a look at the `1stchain` GitHub Pull request #711 to monitor the state of this branch [7].

<sup>2</sup>The Response Functions are different for each combination of the three telescopes: it has to be found out the best way to weight the cuts and the uncertainty of each. They all have different performances; for instance,

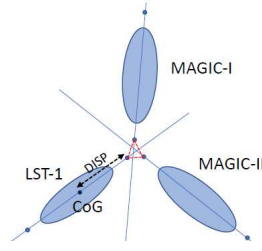


Figure 7.1: Geometrical representation of the `disp` parameter: the ellipsis are the parametrized traces in the three Cherenkov telescopes' Cameras [46]. The arrangement of the three ellipsis comes from the layout of the telescopes in ORM, have a glance at figure 3.4.

The higher analysis Gammapy tools have also to be implemented for MAGIC+LST1 scientific results.

The last two chapters, 5 and 6, report the effective contributions of this work. The present thesis deals with the source independent analysis of four datasets. Three of them have been obtained by grouping the LST1 observations of 1ES1959+650 of performed in 2020, 2021 and 2022. The last dataset is where all the observations from 2020 to 2022 of the blazar are stacked together.

As a future work on 1ES1959+650 would regard, it is interesting to perform the source-dependent analysis starting from low-level stages. The state of art results of this approach are showed in section 4.4, as well as the pros and cons with respect to the source independent approach showed in this thesis.

From the preliminary data selection, useful information about how the telescope works and causes of systematic errors have been studied. Text and graphics in section 5.1 and appendix A give a precise idea on how the datacheck on raw data files (DL1) is performed, i.e. the measurements and parameters to check for each run in order to select good-quality observations. The quantities to monitor are the cosmic-ray and interleaved event rates (in figures 5.3 and 5.4). In addition, the average muon intensity is important to monitor the telescope optical efficiency. It is stable during the observations of 1ES1959+650, as shown in figure 5.5, apart from some runs of 2020, that actually are not in Wobble mode.

Actually, from the  $\sim 14$  hours of observations selected, only 11.21 hours of Wobble mode observation are analysed.

Starting from DL2 stage, i.e. parametrized traces in the Camera, the DL3 files are produced incorporating the proper IRFs: those are produced from the most updated versions of protons, electrons and  $\gamma$ -rays MC simulations. They are classified for different pointing positions of the telescope. These have been a significant improvement in the blazar analysis, although in the presented analysis only the *nearest-IRFs* method have been exploited to create DL3s. A future analysis should be done exploiting the interpolations of the three nodes in the Dealunay triangles grid (in figure 4.9) for each run.

As regards the approaches explored, it has been shown how the energy-dependent  $\gamma$ /hadron separation provides more accurate results: the proofs are in the higher-level analysis products, especially for the SEDs. This is because discerning  $\gamma$ -rays induced showers in the atmosphere from hadrons ones depends essentially on the energy of the primary particle and on the telescope efficiency in that energy bin. For this reason, different cuts are required (as shown in figure 5.18).

To improve the analysis performances, an energy-dependent  $\theta$  cut should also be introduced in the analysis<sup>3</sup>.

The detection (or technically  $\theta^2$ ) plots in section 5.2 are performed exactly with the DL3 files:

---

LST1 achieve the highest ones.

<sup>3</sup>Energy-dependent  $\theta$  cut is supported in v0.20 Gammapy version.

together with the computed Li&Ma significance, they show clearly high excesses in correspondence of the source position. Those have been plotting handling and adapting the scripts presented in the LST data analysis School of January 2022 [46].

The higher-level analysis has been conducted considering only one background region for each run: this is a very basic approach. Using several OFF regions can potentially increase statistics in the background, resulting in a better estimation.

Spectral Energy Distributions are the most important results to characterize the blazar Very High Energy emission and infer the processes behind that. It has been highlighted in the introductory section on 1ES1959+650 previous studies (section 2.2.1). In this work `Python` scripts, relying mostly on `Gammapy` tools, have been implemented to fit the data and produce the SEDs, light curves and differential fluxes plot<sup>4</sup>.

The energy-dependent cut on the *gammaness* results in better performances in the high level products. This improvement is visible especially for the low energy flux points in the SEDs in the four datasets: the residuals with respect to the Log Parabola fit model are smaller.

In section 6.4, LST1 results from 1ES1959+650 observations are compared to Fermi-LAT almost-simultaneous ones; they are superimposed in figure 6.31. The two independent Log Parabola fits are in a good agreement. From the joint fit shown in figure 6.32, the HE peak is located at  $\sim 40$  GeV, however further observations and more sophisticated analyses are required to give an accurate estimation.

This property can also be inferred from the spectral index from Fermi-LAT observations: if it is lower than 2 the peak is located at higher energies, likely at LST1 detected ones. It is shown in plot 6.34 how it is usually the case, even if the spectral index is quite variable and few of them fall in the region  $\alpha > 2$ .

The spectral evolution analysis reveals a hint of *softer when brighter* trend. However, the large errors on the spectral index and the small sample of LST1 data (only 11 nights) cannot confirm it. A richer sample is necessary to reinforce this claim.

In the flares occurred in 2016 [44] an *harder when brighter trend* was found in the VHE  $\gamma$ -ray band of 1ES1959+650 emission. On the other hand, the *softer when brighter* trend would be consistent with the results of [51] in  $\gamma$ -rays during quiescent states. Indeed, in the period from 2020 to 2022 the blazar has not been found in extreme activity states.

By looking at the light curves of 1ES1959+650 in  $\gamma$ -ray band, from LST1 and Fermi-LAT, in X-rays, from *Swift*-XRT and in the radio, from TELAMON project, an intra-week increase in the flux is visible in the higher energies at the beginning of May 2022 (section 6.5).

In particular, LST1 flux shows its maximum value in the observations on 5<sup>th</sup> of May 2022. The exponential fit in plot 6.40 is useful to define the rising/decreasing timescales of 1ES1959+650 flux, although the flux point sample is too low to determine them. In this short epoch the  $F_{var}$  value from LST1 observations is  $\sim 30\%$ , with a relative error  $err(F_{var})/F_{var} = 0.24$ .

To infer causes and properties of this short flare, analyses of the lower frequencies light curves has to be performed.

---

<sup>4</sup>The plots are in the *custom format* of LST1.

# Acknowledgements

This work would not have been possible without the strong support and the kind availability of my two supervisors, Prof. Elisa Bernardini (University of Padova) and Dr. Mireia Nieves Rosillo (Instituto de Astrofísica de Canarias). For introducing me to this research field from the beginning and continuously helping me in this path. It has been a pleasure to work and discuss with them on these topics. A huge thanks to them!

I would also thank the professors and researchers of University of Padova and Universidad de La Laguna/Astrophysics Canarians Institute, I have interacted during the two years of Master degree. From the former, in particular Prof. Alberto Franceschini for giving me some advice on the thesis. As regards the latter, thanks to Prof. Ramón Garcia Lopez and Dr. Monica Vazquez Acosta for hosting and helping me during the period I spent in Tenerife to work on the thesis.

I thank also LST1 analysers and researchers, among all Dr. Chaitanya Priyadarshi (Universitat Autònoma de Barcelona), for helping me in the understanding details of LST1 data analysis flow.

Thanks also to Dr. Matthias Kadler and Dr. Jonas Heßdörfer (TELAMON radio observation project) for their availability. It has been really interesting to discuss with them.

This work, in particular these few lines, are the natural conclusion of the most vivid and emotional two-years of my life, passed, as a friend of mine would say in a nice sense, *wasting life*.

And, as the definition itself suggests, emotions are a *tangled* field, so without an always-good or -bad meaning. However, always incredibly vivid.

Not bad in a Nietzsche's eternal recurrence perspective, but less would be even better.

It has been so because of the people and the places always are in my life. Especially thanks to my family support and love: my dad, mum and sister, my grandparents, uncles and cousins. From you I have learned the enthusiasm and the motivations for hard-working on your passions. To the always' friends: we are incessantly transforming without losing each other.

To the people and places recently exploded in my life.

I understood lots of things from all of you. Including the fact that not all is understandable. Including the reasons why I have been writing this thesis too.

However, we always attempt to understand a little bit deeper, *this is our life!*

# Appendix A

## Details on data quality selection

In this step, as already introduced in 4.2, the cuts have been applied to all the DL1\_datacheck\_202\*.h5 files contained in the IT Container in the directories:

```
/fe/s/aswg/data/real/OSA/DL1DataCheck_LongTerm/v0.9/20 * /
```

The datacheck script scans over all the available LST1 runs of the latest `lstchain` version from 2020 up to 02/06/2022.

The list follows (in bold the Wobble runs that are going to be analysed):

2020-07-11 : [2195]  
2020-07-13 : [2202, **2203**, 2206, 2207]  
2020-07-26 : [2348, 2350, 2351, 2352]  
2020-08-09 : [**2370**, 2373]  
2020-08-10 : [**2380**]  
2020-08-11 : [**2408**, **2409**, **2411**, **2412**, **2413**]  
2021-03-19 : [**4172**, **4173**, **4174**, **4175**, **4176**, **4177**]  
2021-08-07 : [**5520**, **5521**, **5522**, **5523**, **5524**, **5525**, **5526**, **5527**, **5528**, **5529**, **5530**, **5531**, **5532**, **5533**, **5540**, **5542**]  
2022-04-29 : [**8013**, **8014**, **8015**, **8016**]  
2022-05-01 : [**8065**, **8066**, **8067**]  
2022-05-02 : [**8086**, **8087**, **8088**]  
2022-05-03 : [**8111**, **8112**, **8113**, **8114**]  
2022-05-05 : [**8198**, **8199**, **8200**]

Some of the plots mentioned in the section 5.1 are reported in the following.

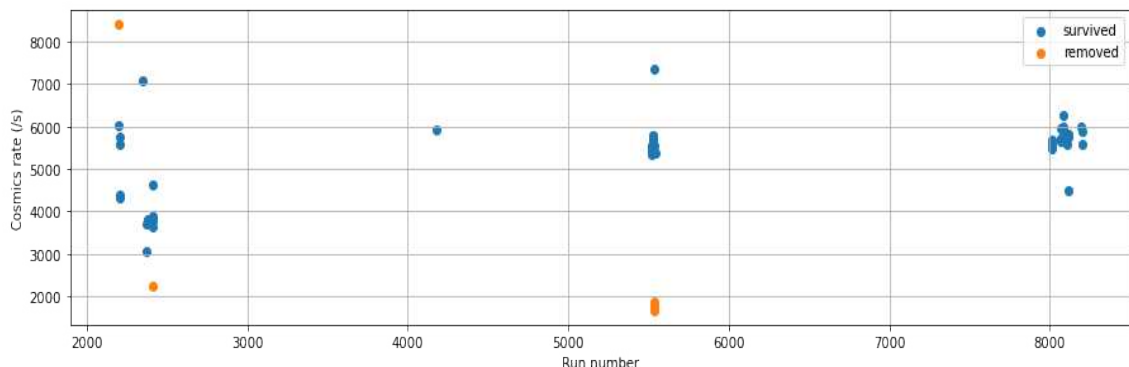


Figure A.1: Cosmic rate per each run: in orange the runs that have been ruled out.

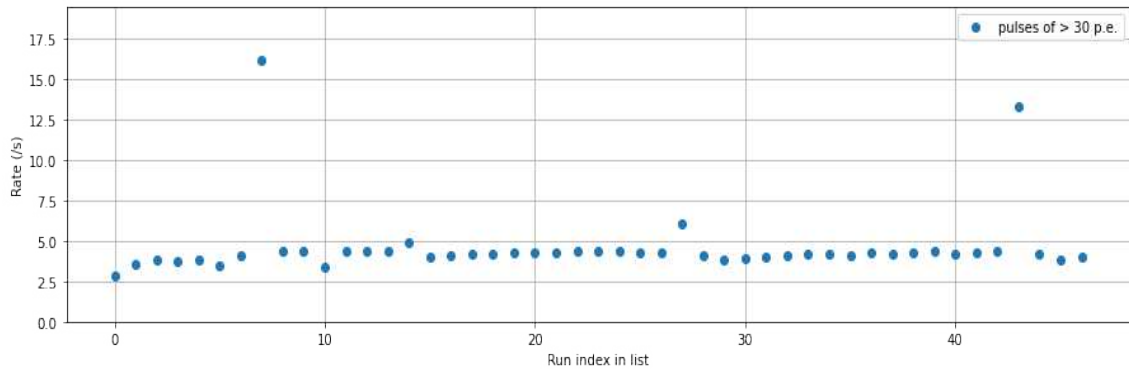


Figure A.2: Rate of pulses with a charge larger than 30 photo-electrons: the runs have been ordered and indexed in an ordered list.

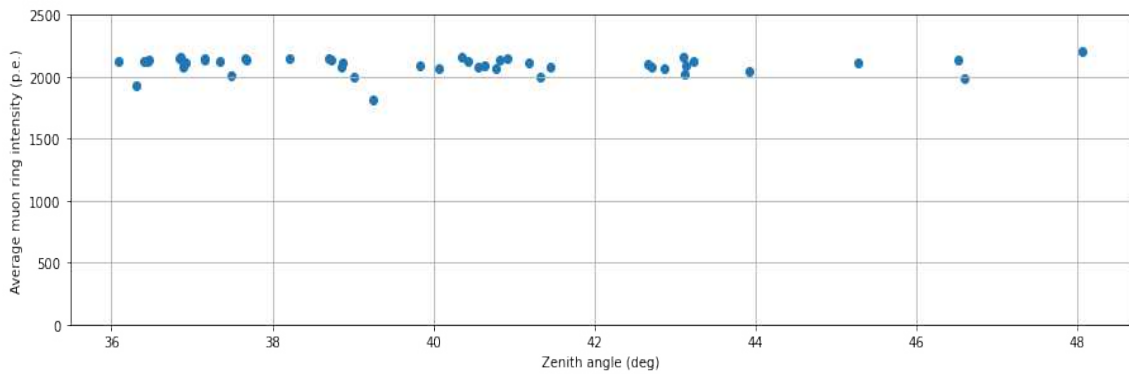


Figure A.3: Estimated intensity of muon rings in dependence on the observation zenith angle.

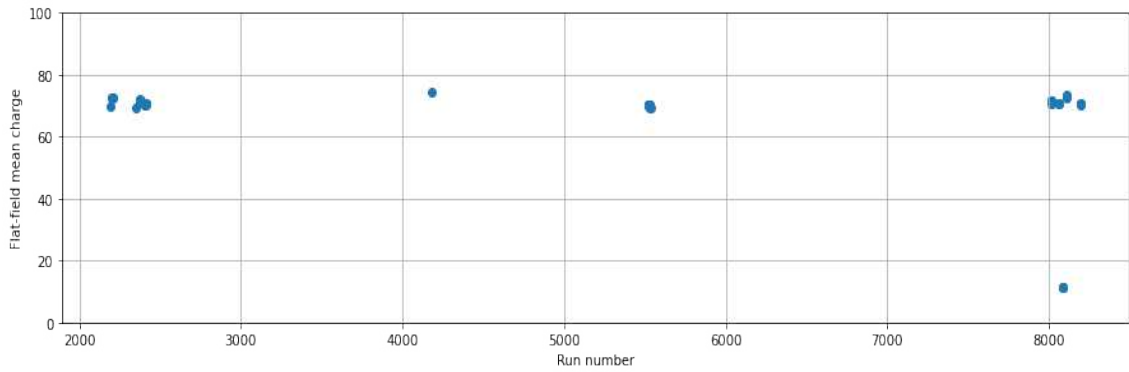


Figure A.4: Flat-Field mean charge for each run.

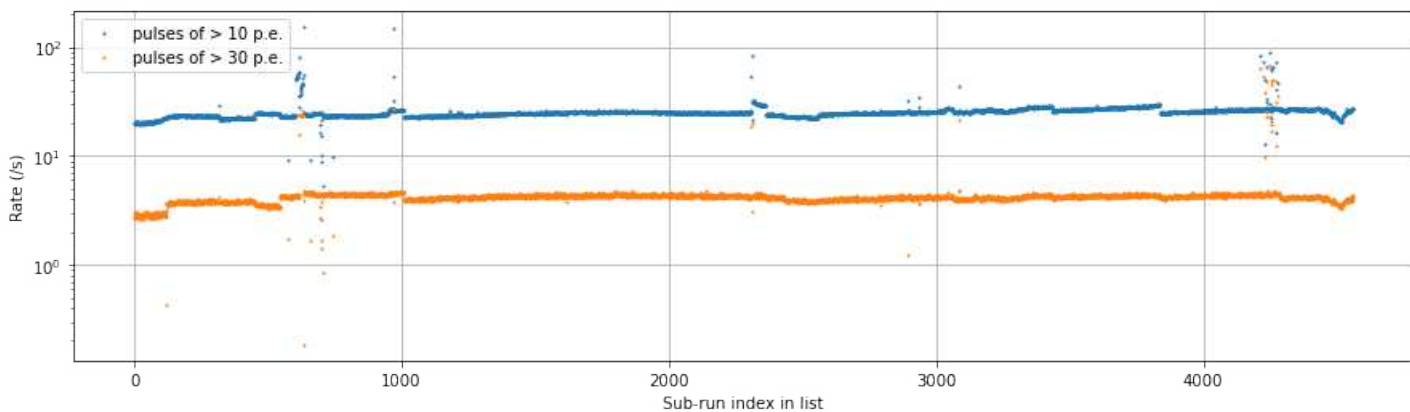


Figure A.5: Check on subruns' rates on both pulses of cosmic rays.

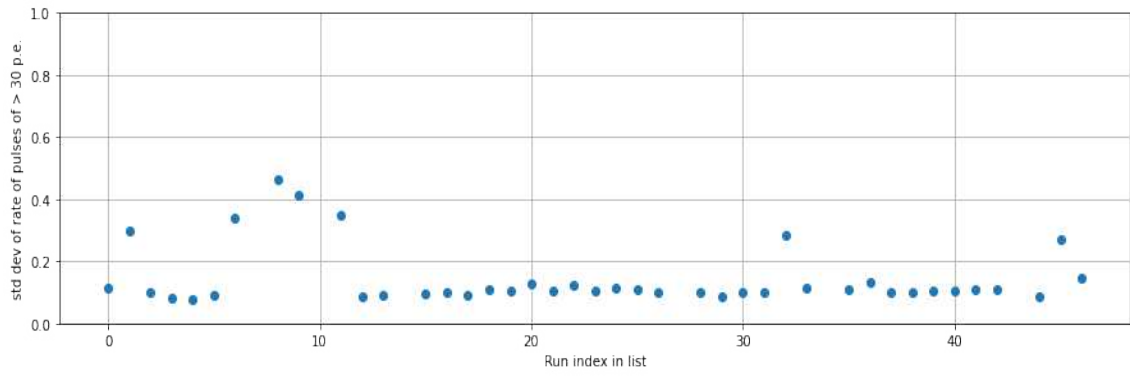


Figure A.6: Standard deviation of pulse rate larger than 30 per each run.

# Appendix B

## Physics of blazar emission

### B.1 Radiative processes

In this section the most relevant physical processes quoted in the text are presented, reporting the most useful formulae.

#### B.1.1 Relativistic beaming

Having two reference systems, S and S', in relative motion with a velocity  $v$ , the velocity of a point in S in terms of S' measured velocities is in general:

$$u_{\parallel} = \frac{u'_{\parallel} + v}{1 + vu'_{\parallel}/c^2} \quad u_{\perp} = \frac{u'_{\perp}}{\gamma(1 + u'_{\parallel}v/c^2)} \quad (\text{B.1})$$

The **relativistic aberration** law gives the relation between the velocity directions in the two frames:

$$\tan \theta = \frac{u_{\perp}}{u_{\parallel}} = \frac{u' \sin \theta'}{\gamma(u' \cos \theta' + v)} \quad (\text{B.2})$$

where  $u' \equiv |\vec{u}'|$ . If one sets  $u' = c$ , the aberration of light is obtained. Setting for instance  $\theta' = \pi/2$ , photon emitted at right angle in S', one has that  $\tan \theta = \frac{c}{\gamma v}$  and  $\sin \theta = \frac{1}{\gamma}$ . So for high relativistic velocities ( $\gamma \gg 1$ ):

$$\theta \sim \frac{1}{\gamma} \quad (\text{B.3})$$

For an isotropic source, as in B.1, most of the photons are emitted in the forward direction. It is an important effect for blazar studies, since the relativistic jet is at small angles with respect to the line of sight. Due to relativistic jet we see a highly collimated jet and the observed luminosity is enhanced:

$$L_{obs} = \delta^p L_{emi} \quad (\text{B.4})$$

in which  $\delta = \frac{1}{\gamma(1 - \beta \cos \theta)}$  is the Doppler boosting factor.  $p$  depends on the emitted spectrum shape and the jet physics:  $p = 3 + \alpha$  is for a moving compact source and  $p = 2 + \alpha$  for a continuous jet ( $\alpha$  is the spectral index) [25].

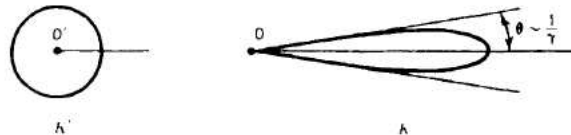


Figure B.1: Isotropic emission in rest primed frame: relativistic beaming effect is observed in the no-primed system [1]

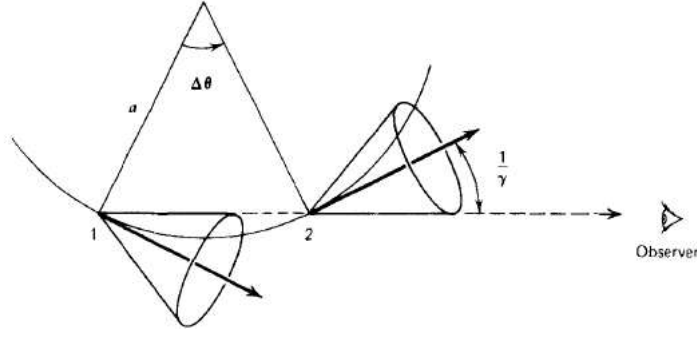


Figure B.2: Charged relativistic particle in a circular uniform motion trajectory; the emission cones with aperture  $\sim \gamma^{-1}$  are drawn [1].

### B.1.2 Synchrotron radiation

Larmor's law quantifies the power produced by a relativistic particle moving in a region with a magnetic field  $\vec{B}$ :

$$P = \frac{2}{3} r_0^2 c \beta_{\perp}^2 \gamma^2 B^2 \quad (\text{B.5})$$

$\beta_{\perp} = v_{\perp}/c$  is the particle velocity in the plane perpendicular to  $\vec{B}$ ,  $r_0 = \frac{q^2}{mc^2}$  and  $\gamma$  is the Lorentz factor.

Synchrotron radiation spectrum depends on the electric field evolution seen by the observer: relativistic beaming effects play a determinant role in that. A sketch is in B.2. The observer sees the radiation only when the particle is in the stretch from 1 to 2, so the distance along the path is  $\Delta s = a \cdot \Delta \theta$ . From geometric consideration and the relativistic Lorentz force, one obtains:

$$\frac{\Delta \theta}{\Delta s} = \frac{qB \sin \alpha}{\gamma m c v} \quad (\text{B.6})$$

where  $\Delta s = v(t_2 - t_1)$  and  $\sin \alpha$  is the factor difference from a circle radius. The time interval the particle emits the radiation in 1 and 2 is:

$$t_2 - t_1 = \Delta t_e \approx \frac{2}{\gamma \omega_B \sin \alpha} \quad (\text{B.7})$$

The observer *sees* the time interval as  $\Delta t_o = \left(1 - \frac{v}{c}\right) \Delta t_e$  because of relativistic Doppler effect. For  $\gamma \gg 1$ , one has  $1 - \frac{v}{c} \approx \frac{1}{\gamma^2}$ , so it is obtained:

$$\Delta t_o \approx \frac{1}{\gamma^3 \omega_B \sin \alpha} \quad (\text{B.8})$$

The observed pulses is smaller than the gyration period of the particle. The consequent characteristic frequency of synchrotron emission is:

$$\omega_c = \frac{1}{\Delta t_o} = \frac{3}{2} \gamma^3 \omega_B \sin \alpha = 280 \left(\frac{\gamma}{100}\right)^2 \left(\frac{B}{1 \mu\text{G}}\right) \text{MHz} \quad (\text{B.9})$$

the last step is derived by inserting numerical values. For an AGN with  $B \approx 1 \text{ G}$  and for ultrarelativistic particles ( $\gamma \gg 1$ ), this emission process can explain GHz radio emission. It can be shown [1] that, in the frequency space, for each electron the emitted power per unit frequency is:

$$P(\omega) = \frac{\sqrt{3}}{2\pi} \frac{q^3 B \sin \alpha}{m c^2} F(\omega/\omega_c) \quad (\text{B.10})$$

To obtain the overall spectra, firstly, one has to consider the particle distribution. For a non-thermal distribution, electrons are distributed as:

$$\frac{dN}{dE} = N_0 E^{-p} \quad (\text{B.11})$$

It can also be written in term of  $\gamma$  since  $E = \gamma mc^2$ . So the total power per unit volume per unit frequency (recalling B.10) emitted by a non-thermal  $e^-$  population is:

$$P_{tot}(\omega) \propto \int_{\gamma_1}^{\gamma_2} F\left(\frac{\omega}{\omega_c}\right) \gamma^{-p} d\gamma \quad (\text{B.12})$$

and defining  $x \equiv \omega/\omega_c$ ,  $\omega_c \propto \gamma^2$ :

$$P_{tot} \propto \omega^{-(p-1)/2} \int_{x_1}^{x_2} F(x) x^{(p-3)/2} dx \quad (\text{B.13})$$

in a wide range  $x_1 \rightarrow 0$  and  $x_2 \rightarrow \infty$ : approximately the integral is constant. In this case:

$$P_{tot}(\omega) \propto \omega^{-(p-1)/2} \quad (\text{B.14})$$

Particle and photon spectral indexes for the synchrotron process are related as  $s = \frac{p-1}{2}$ . From photons spectral analysis one can infer physical properties of AGNs' core, such as the electron distribution. B.14 is valid only if  $e^-$ . There is usually a frequency threshold (so called *turnoff*) before which electrons absorb synchrotron radiation. It is called **Synchrotron-Self-Absorption** and for  $\omega < \omega_{turnoff}$ :

$$P_{tot}(\omega) \propto \omega^{5/2} \quad (\text{B.15})$$

### B.1.3 Inverse Compton

The equation describing the evolution of the distribution function of photons due to repeated nonrelativistic Inverse Compton scattering is the **Kompaneets law** [57]:

$$\frac{\partial n}{\partial t_c} = \left(\frac{kT}{mc^2}\right) \frac{1}{x^2} \frac{\partial}{\partial x} [x^4(n' + n + n^2)] \quad (\text{B.16})$$

where  $n(\omega)$  is the isotropic photon phase space density  $t_c \equiv (n_e \sigma_T c) \cdot t$  (time in units of mean time between two scatterings),  $x \equiv \frac{\hbar\omega}{kT}$  ( $\omega$  photon frequency,  $T$  temperature of thermal nonrelativistic  $e^-$  population) and  $n' \equiv \partial n / \partial x$ .

It is solved only through numerical integration. After photons are scattered up to higher energies following Bose-Einstein distribution ( $n = (e^{\mu+x} - 1)^{-1}$ ,  $\mu$  finite chemical potential), the spectrum is *saturated*, i.e. approximately a Wien law with a small occupation number ( $\mu \gg 1$ ).

For a saturated inverse Compton scattering (considering also free-free processes) the medium spectrum looks like B.3. At low energies it is a blackbody, then it becomes a modified blackbody. At high frequencies, a Wien spectrum is obtained.

As the non-stationary solution regards, i.e. *unsaturated* case, using a modified steady-state Kompaneet's equation, one obtains an intensity

$$I_\nu \sim I_{\nu_s} \left(\frac{\nu}{\nu_s}\right)^{3+m} \quad \nu_s \ll \nu \ll \frac{kT}{h} \quad (\text{B.17})$$

In the intermediate regime.  $m$  is the spectral index that depends on the Compton parameter  $y$ .

For  $\nu \gg 1$  a Wein's law is obtained, whereas for  $x \leq x_s$  one has a "soft" photons input. In B.4 the spectrum generated by *unsaturated* Compton scattering (low energy photons and thermal  $e^-$ ).

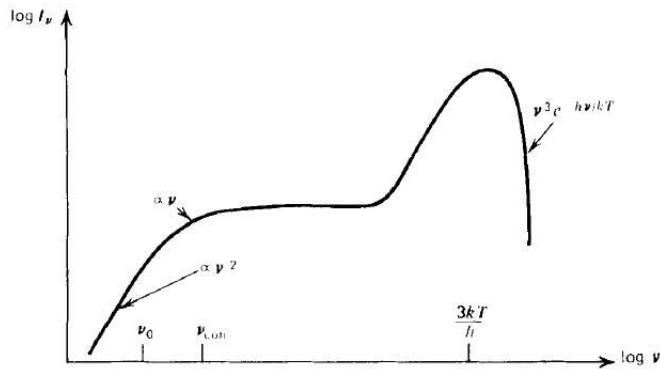


Figure B.3: Spectrum from a non-thermal nonrelativistic plasma: it takes into account free-free emission and absorption, saturated Inverse Compton scattering [57]. At low frequencies free-free absorption is relevant,  $\nu_0$  is the frequency at which scattering and absorption coefficients are equal. From  $\nu_{coh}$  on Inverse Compton effects (incoherent scattering) start to be dominating.

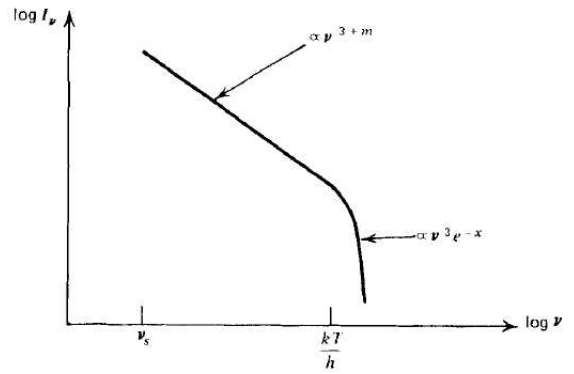
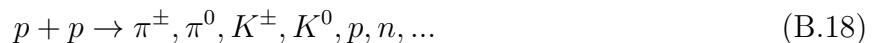


Figure B.4: Intensity spectrum by non-stationary Comptonization.

### B.1.4 Hadronic processes

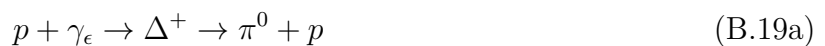
In this section the processes involving protons are going to be treated: these are the most significant mechanisms occurring in the hadronic model [62].

Apart from the detection of  $\gamma$ -rays, another signature of the presence of relativistic protons is commonly given by neutrinos.  $\gamma$ -rays and neutrinos are produced by secondary mesons decays. Mesons can be produced in the  $p$ - $p$  collision:

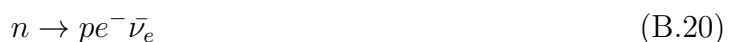


the suspension points are for higher mass mesons or baryons, so more rarely produced. Accelerated protons could interact with environmental protons in the source nearby or during the propagation, far away from the production site. The cross section for B.18 is between 40-50 mb; the particles produced in the inelastic scatter have a small perpendicular momentum.

Another process protons usually undergo (always either close to the source or during their propagation towards us) is the **photoproduction**. Relativistic protons interact with ambient photons<sup>1</sup> producing secondary mesons. It occurs through the  $\Delta^+$  resonance at  $\sim 0.25$  mb:



The cross section  $\sigma_{\gamma p}$  is smaller than  $\sigma_{pp}$  of two order of magnitude. However, since the rate of these processes depends on the  $\gamma$  (in B.19) and proton (in B.18) densities<sup>2</sup>, it could occur that the *photoproduction* process has an higher probability in some high photon density environment. In general, protons are confined by high magnetic field: what escapes from the source are neutrons and decay products of mesons. The former can escape from the strong magnetic field region near to the source and then turn into protons in the weak interaction decay:



<sup>1</sup>Especially in the nearby of AGN there is a high density of various wavelength photons.

<sup>2</sup>The general formula for the event rate for a single  $p$  to interact with a certain particles' population is given by  $r \sim \sigma \cdot n \cdot c$ .  $\sigma$  is the cross section of the process,  $n$  is the number density of the environmental particle population,  $c$  the speed of light.

As the latter concerns, neutral pions decay producing  $\gamma$ -rays:

$$\pi^0 \rightarrow \gamma\gamma \quad (\text{B.21})$$

In the rest frame, each photon has an energy  $E_\gamma^* = m_\pi c^2 / 267.5 \text{ MeV}$  and opposite momentum with respect to the other.

Positive charged mesons decay according to the chain:

$$\pi^+ \rightarrow \nu_\mu + \mu^+ \quad (\text{B.22a})$$

$$\hookrightarrow \mu^+ \rightarrow \bar{\nu}_\mu + \nu_e + e^+ \quad (\text{B.22b})$$

It is the reason why a further probe for the hadronic emission of AGNs is the coincident detection of high-energy neutrinos' fluxes by dedicated instruments (e.g. AMANDA, IceCube etc.).

## B.2 Results from 1ES1959+650 literature

In this section some plots quoted in 2.2.1 are reported in order to visualize how 1ES1959+650's broadband SED is fitted by different emission models. A general phenomenological parametrization of blazars' SEDs has been given in 2.1.

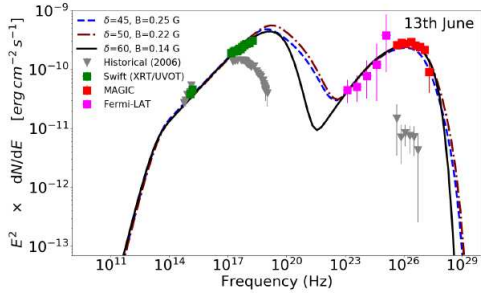


Figure B.5: 1ES1959+650 SED of 13/06/2016 fitted by a leptonic model with three different combinations of the Doppler factor ( $\delta$ ) and magnetic field (B). To agree with the broad band spectra the SSC model requires a large Doppler factor, so highly relativistic small regions in the jet for  $\gamma$ -ray radiation. 2016 data are compared to quiescent one (in grey) [44].

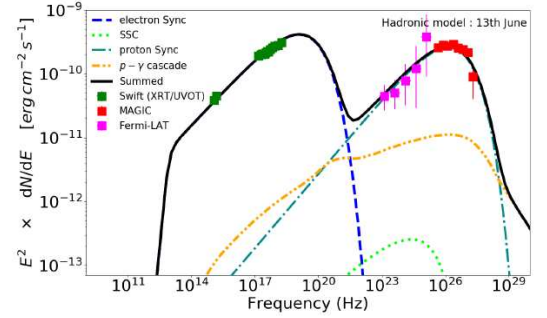


Figure B.6: 1ES1959+650 13/06 SED fitted through the hadronic model. It needs a very high magnetic field ( $\sim 100G$ ) and a acceleration efficiency  $\sim 1$  to agree with MAGIC VHE flux points [44]. Since for this values  $e^-$  cools down very rapidly, a hard injection  $e^-$  spectrum ( $<2$ ) is necessary to explain X-ray emission.

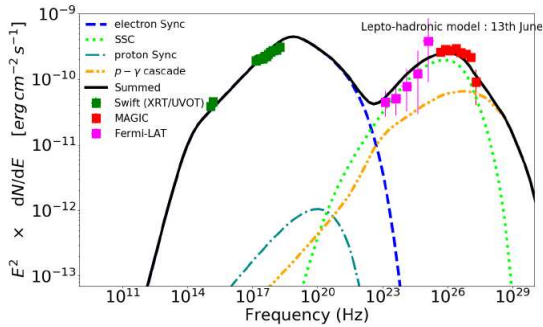


Figure B.7: Same data of the previous two SEDs of the same paper explained by lepto-hadronic model. In this context super-Eddington values of the jet power are required (they are predicted by some other investigations). Jet power can also be reduced assuming an external radiation field [44].

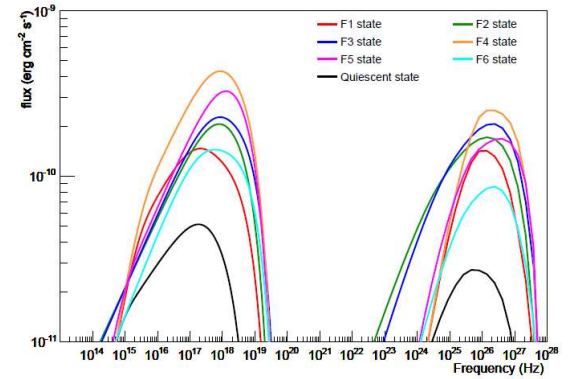


Figure B.8: Evolution of the inner blob of two-zones SSC model used to fit the flux points from 1ES1959+650 2016 flare. A clear shift toward higher energy is spotted for the low-energy peak [51].

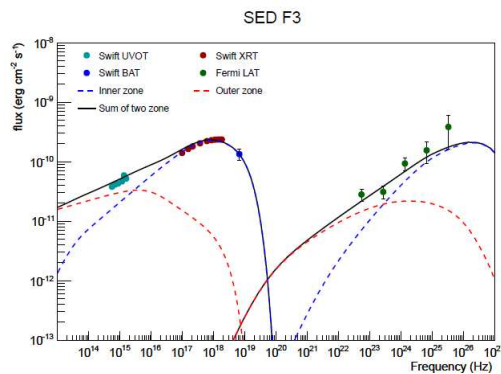


Figure B.9: SED from 11/06 to 20/06 with two-zone model. It does not comprehend VHE data. The inner and outer zone contributions are respectively in blue and red dashed lines. [51]

# Appendix C

## Statistical tools

### C.1 Li&Ma significance

The Li&Ma equation [39] is:

$$S = \sqrt{2} \left( N_{on} \cdot \ln \left( \frac{(1+n)N_{on}}{n(N_{on} + N_{off})} \right) + N_{off} \cdot \ln \left( \frac{(1+n)N_{off}}{N_{on} + N_{off}} \right) \right)^{1/2} \quad (C.1)$$

It is a well-known formula useful to estimate the significance of positive observations in looking for  $\gamma$ -ray sources. Its validity has been probed by MC simulations.

$N_{on}$  is the number of photons detected during the time  $t_{on}$  the detector points towards the suspected source. The background events detected for a time  $t_{off}$  are contained in  $N_{off}$ .  $\alpha$  is the ratio of the on-source time to off-source one. If a sample  $(N_{on}, N_{off})$  is obtained in a observation and they are not too few, C.1 can be used: "S standard deviation event" has been observed.

### C.2 Power Law decorrelation energy

The statistical error on the spectrum can be visualized through a contour that shows the  $1\sigma$  confidence band of the Power Law model just fitted [8]. Taken a Powerlaw:

$$\phi(E) = dN/dE = \phi_0 \left( \frac{E}{E_0} \right)^{-\gamma} \quad (C.2)$$

with normalization and its error  $\phi_0 \pm \delta\phi$ , the photon index  $\gamma \pm \delta\gamma$  and covariance  $cov(\phi_0, \gamma)$ . The contour is defined as:

$$\frac{\delta\phi^2}{\phi^2} = \frac{\delta\phi_0^2}{\phi_0^2} - \frac{2cov(\phi_0, \gamma)}{\phi_0} \log \left( \frac{E}{E_0} \right) + \delta\gamma^2 \log^2 \left( \frac{E}{E_0} \right) \quad (C.3)$$

The diagram has the narrowest point at the decorrelation energy:

$$E_d = E_0 \exp[cov(\phi_0, \gamma)/\phi_0 \delta\gamma^2] \quad (C.4)$$

It is the energy at which the two parameters are less correlated and it is usually estimated by looking at the so-called "butterfly" plot. It is taken as the energy at which the flux errors are the smallest. It has been used as reference energy in the 1ES1959+650 analysis (section 6.1).

### C.3 Statistic in Gammapy fits

The estimation of signal events number or of physical models quantities or excess count significance<sup>1</sup> is performed in Gammapy through Poisson likelihood functions of the type:

$$\mathcal{L}(X|\Theta) = \prod_i^N \frac{f_i^{n_i} e^{-f_i(\Theta)}}{n_i!} \quad (\text{C.5})$$

where  $\Theta$  are the parameter space of the model,  $i$  is the bin index,  $N$  is the total number of bins,  $n_i$  is the number of events in the  $i$ -th bin and  $f_i$  is the test model value of the bin. Using the likelihood function  $\mathcal{L}$ , the fit statistics are the log-likelihood normalized  $2 \times \log\mathcal{L}$  [19].

The approach to model and fit is based on the canonical hypothesis testing, i.e. whether an hypothesis  $H_1$  is statistically preferred to  $H_0$ , the null hypothesis. The  $p$ -value can be estimated through the maximum log-likelihood ratio method<sup>2</sup> (for nested hypothesis), namely  $\lambda = \frac{\max\mathcal{L}(X|H_1)}{\max\mathcal{L}(X|H_0)}$ .

$-2\log\lambda$  is the difference between the fit statistic values hence the Test Statistic (TS). It can be converted to the significance through employing simple `scipy.stats` functions.

For instance, the excess significance one can take the square-root of the measurements TS to get the Li&Ma significance C.1. A useful tool to estimate the significance with an unknown background is `WStatCountsStatistic`.

### C.4 Fractional variability amplitude

The Fractional variability amplitude and its uncertainty are defined as [54]:

$$F_{var} = \sqrt{\frac{S^2 - \bar{\sigma}_{err}^2}{\bar{x}^2}} \quad (\text{C.6a})$$

$$S^2 = \frac{1}{N-1} \sum_{i=1}^N (x_i - \bar{x})^2 \quad (\text{C.6b})$$

$$\bar{\sigma}_{err}^2 = \frac{1}{N} \sum_{i=1}^N \sigma_{err,i}^2 \quad (\text{C.6c})$$

$$\sigma(F_{var}) = \sqrt{\left(\sqrt{\frac{1}{2N}} \frac{\bar{\sigma}_{err}^2}{\bar{x}^2 F_{var}}\right)^2 + \left(\frac{\sqrt{\bar{\sigma}_{err}^2}}{N} \frac{1}{\bar{x}}\right)^2} \quad (\text{C.6d})$$

$S^2$  is the sample variance and  $\bar{\sigma}_{err}^2$  is the mean square error.

$x_i$  and  $\sigma_{err,i}$  are the  $i$ -th flux and its uncertainty of the light curve of  $N$  flux points.  $\bar{x}$  is the mean of the fluxes sample.

<sup>1</sup>It is the probability that a given number of detected events ( $n_{on}$ ) contains  $n_{sig}$  events.

<sup>2</sup>The quantity  $2\log\lambda$  follows a  $\chi^2$  distribution under some hypothesis with degrees of freedom given by the difference of  $H_1$  and  $H_0$  free parameters. It is valid under some conditions, stated in the Wilks theorem.

# List of Figures

1.1	Cherenkov effect . . . . .	2
1.2	Cherenkov telescopes sketch . . . . .	3
1.3	Blazar 1ES1959+650 in optical band . . . . .	4
2.1	Active Galactic Nuclei structure . . . . .	6
2.2	Corona and accretion disk of AGN . . . . .	6
2.3	”Periodic table” of AGNs . . . . .	7
2.4	Spectral non-thermal profile of blazars . . . . .	7
2.5	Phenomenological classification of blazars . . . . .	8
2.6	Parametrization of blazars’ Spectral Energy Distribution . . . . .	9
2.7	Scheme of hadronic mirror model . . . . .	11
3.1	The Large-Sized Telescope LST1 . . . . .	14
3.2	Camera of LST1 . . . . .	14
3.3	Scheme of LST1 infrastructure in La Palma Observatory . . . . .	14
3.4	Cherenkov Telescope Array North site project . . . . .	15
3.5	Layout of the forthcoming CTA telescopes . . . . .	16
3.6	Sensitivity plots of MAGIC and CTA North with extrapolated 1ES1959+650 flux . . . . .	17
3.7	Fermi mission . . . . .	17
3.8	Fermi Large Area Telescope schematic picture . . . . .	17
3.9	<i>Swift</i> observatory . . . . .	18
3.10	TELAMON project radio telescope . . . . .	19
4.1	Gammapy workflow . . . . .	22
4.2	Raw signals from LST1’s Camera . . . . .	23
4.3	Cleaned image in the Camera . . . . .	24
4.4	Muon trace detected by LST1 . . . . .	24
4.5	LST1 optical efficiency determined by muons . . . . .	25
4.6	LST1 efficiency <i>light curve</i> . . . . .	25
4.7	Hillas ellipsis parametrization . . . . .	26
4.8	Corsika simulated atmospheric shower . . . . .	28
4.9	New-MC simulation <i>coordinates</i> . . . . .	28
4.10	Sensitivities of source dependent and independent analysis . . . . .	31
4.11	Discerning $\gamma$ from hadron events in the source dependent approach . . . . .	31
4.12	$\gamma$ /hadron separation in source independent analysis . . . . .	31
4.13	MC <i>vs</i> reconstructed energies in the two approaches . . . . .	32
4.14	Parameter correlation in the dependent analysis . . . . .	32
4.15	Parameters in source dependent case . . . . .	32
5.1	Offset histogram of 1ES1959+650 observations from LST1 . . . . .	37
5.2	Histogram of azimuth and zenith angles . . . . .	37
5.3	Cosmic-ray events’ rates in dependence on the zenith angle . . . . .	37

5.4	Systematic background event rates . . . . .	38
5.5	Intensity of detected muon during 1ES1959+650 observation . . . . .	38
5.6	Camera time resolution . . . . .	39
5.7	Detection plot of a single run . . . . .	39
5.8	2D histogram plot of the source detection . . . . .	39
5.9	Detection plot for 2020 dataset . . . . .	40
5.10	Detection plot for 2021 dataset . . . . .	40
5.11	Detection plot for 2022 dataset . . . . .	40
5.12	Detection plot of the total dataset . . . . .	41
5.13	Excess plot of total dataset . . . . .	41
5.14	Detection plot of the total dataset in different energy range . . . . .	41
5.15	$\gamma$ /hadron separation energy-dependent with a 80% efficiency . . . . .	42
5.16	$\gamma$ /hadron separation energy-dependent with a 80% efficiency . . . . .	42
5.17	Effective area for different zenith angles . . . . .	43
5.18	Energy-dependent $\gamma$ /hadron cuts for different combination of zenith angles . . . . .	43
6.1	Source and background regions (analysis of dataset 2020) . . . . .	45
6.2	Source and background regions (2021) . . . . .	45
6.3	Source and background regions (2022) . . . . .	45
6.4	Single run plots of excess, exposure and energy migration . . . . .	45
6.5	Cumulative excess and significance plot of 2020 dataset . . . . .	46
6.6	Cumulative excess and significance plot of 2021 dataset . . . . .	46
6.7	Cumulative excess and significance plot of 2022 dataset . . . . .	46
6.8	Spectral Energy Distribution of 2020 1ES1959+650 data . . . . .	48
6.9	Excess plot as function of energy for 2020 dataset . . . . .	48
6.10	Spectral Energy Distribution of 2021 . . . . .	48
6.11	Excess plot as function of energy for 2021 dataset . . . . .	48
6.12	Spectral Energy Distribution of 2022 . . . . .	49
6.13	Excess plot as function of energy for 2022 dataset . . . . .	49
6.14	Light curve of 1ES1959+650 as observed by LST1 . . . . .	50
6.15	2021 light Curve of 1ES1959+650 from LST1 . . . . .	50
6.16	2022 light Curve of 1ES1959+650 from LST1 . . . . .	50
6.17	Correlation matrix of fit's parameters . . . . .	51
6.18	Differential spectrum of 1ES1959+650 . . . . .	51
6.19	Total dataset Spectral Energy Distribution (global separation) . . . . .	51
6.20	Excess plot as function of energy . . . . .	51
6.21	Fit Test Statistic spectral profile . . . . .	52
6.22	2020 SED with energy-dependent $\gamma$ /hadron cuts . . . . .	53
6.23	Excess plot as function of energy for 2020 dataset (energy-dependent separation) . . . . .	53
6.24	2021 SED with energy-dependent $\gamma$ /hadron cuts . . . . .	53
6.25	Excess plot as function of energy for 2021 dataset (energy-dependent separation) . . . . .	53
6.26	2022 SED with energy-dependent $\gamma$ /hadron cuts . . . . .	54
6.27	Excess plot as function of energy for 2022 dataset (energy-dependent separation) . . . . .	54
6.28	Total dataset SED with energy-dependent $\gamma$ /hadron cuts . . . . .	54
6.29	Excess <i>vs</i> energy in the energy-dependent cut analysis . . . . .	54
6.30	Fermi-LAT Field of view . . . . .	55
6.31	Fermi-LAT and LST1 Spectral Energy Distributions . . . . .	56
6.32	Joint fit of Fermi-LAT and LST1 spectral flux points . . . . .	57
6.33	Fermi-LAT analysis with Cherenkov telescopes software . . . . .	58
6.34	Spectral index evolution from LST1 and Fermi-LAT . . . . .	58
6.35	Linear fit of LST1 spectral indexes . . . . .	59
6.36	Constant fit of LST1 spectral indexes . . . . .	59

6.37	Linear fit of LST1 spectral indexes . . . . .	59
6.38	Constant fit of Fermi-LAT spectral indexes . . . . .	59
6.39	Multiwavelength light curves of 1ES1959+650 from 2020 to 2022 . . . . .	60
6.40	Gaussian and exponential fit of 2022 LST1 light curve . . . . .	61
7.1	Stereoscopic reconstruction LST1+MAGIC . . . . .	64
A.1	Cosmic rate for 1ES1959+650 observations . . . . .	67
A.2	High-charge rate pulses . . . . .	68
A.3	Intensity of muon rings at different zenith angles . . . . .	68
A.4	Pixels' efficiencies before the observations . . . . .	68
A.5	Cosmic rates rates of smaller samples . . . . .	68
A.6	High-charge rate pulses standard deviation . . . . .	69
B.1	Relativistic beaming effect . . . . .	70
B.2	Synchrotron radiation model . . . . .	71
B.3	Saturated Inverse Compton spectrum from a non-thermal . . . . .	73
B.4	Unsaturated Inverse Compton spectrum . . . . .	73
B.5	1ES1959+650 SED of 2016 flare fitted by leptonic model . . . . .	75
B.6	1ES1959+650 SED of 2016 flare fitted by hadronic model . . . . .	75
B.7	1ES1959+650 SED of 2016 flare fitted by lepto-hadronic model . . . . .	75
B.8	1ES1959+650 evolution of the low- and high-energy peaks in 2016 . . . . .	75
B.9	SED of 1ES1959+650 fitted considering two emission zones . . . . .	75

# List of Tables

6.1	Fits results from Spectral Energy Distrubution (global $\gamma$ /hadron separation) . .	47
6.2	Fits' results from the analysis with energy-dependent $\gamma$ /hadron separation . . .	52
6.3	LogParabola fit of Fermi-LAT SED . . . . .	55
6.4	Results from the joint fit of Fermi-LAT and LST1 SEDs . . . . .	57
6.5	Results from spectral indexes' fits . . . . .	59
6.6	Gaussian fit results of 2022 light curve . . . . .	61
6.7	Exponential fit results of 2022 light curve . . . . .	61

# Bibliography

- [1] *SYNCHROTRON RADIATION*, chapter 6, pages 167–194. John Wiley Sons, Ltd, 1985.
- [2] *Science with the Cherenkov Telescope Array*. WORLD SCIENTIFIC, feb 2018.
- [3] The ogip standard pha file format, 2021.
- [4] Corsika – an air shower simulation program, 2022.
- [5] Data formats for gamma-ray astronomy, 2022.
- [6] Prototype cta pipeline framework (ctapipe), 2022.
- [7] Repository for lst analysis software (cta-lstchain), 2022.
- [8] A. A. Abdo, M. Ackermann, M. Ajello, W. B. Atwood, M. Axelsson, L. Baldini, J. Ballet, G. Barbiellini, M. G. Baring, and D. Bastieri et al. Fermi observations of tev-selected active galactic nuclei. *The Astrophysical Journal*, 707(2):1310–1333, dec 2009.
- [9] AA Abdo, Markus Ackermann, Marco Ajello, and WB et al. Atwood. Spectral properties of bright fermi-detected blazars in the gamma-ray band. *The Astrophysical Journal*, 710(2):1271, 2010.
- [10] M. Ajello, R. Angioni, M. Axelsson, J. Ballet, G. Barbiellini, D. Bastieri, and J. Becerra Gonzalez et al. The fourth catalog of active galactic nuclei detected by the ifermi/i large area telescope. *The Astrophysical Journal*, 892(2):105, apr 2020.
- [11] J. Aleksić, S. Ansoldi, L.A. Antonelli, and P. Antoranz et al. Measurement of the crab nebula spectrum over three decades in energy with the magic telescopes. *Journal of High Energy Astrophysics*, 5-6:30–38, 2015.
- [12] J. Aleksić, S. Ansoldi, L.A. Antonelli, and P. Antoranz et al. The major upgrade of the magic telescopes, part i: The hardware improvements and the commissioning of the system. *Astroparticle Physics*, 72:61–75, 2016.
- [13] Volker Beckmann and Chris R. Shrader. The agn phenomenon: open issues, 2013.
- [14] David Berge, S Funk, and J Hinton. Background modelling in very-high-energy  $\gamma$ -ray astronomy. *Astronomy & Astrophysics*, 466(3):1219–1229, 2007.
- [15] Konrad Bernlöhner. Simulation of imaging atmospheric cherenkov telescopes with corsika and sim\_telarray. *Astroparticle Physics*, 30(3):149–158, 2008.
- [16] Stefano Bianchi, Vincenzo Mainieri, and Paolo Padovani. Active galactic nuclei and their demography through cosmic time. 03 2022.
- [17] M. Błażejowski, G. Blaylock, and I. H. Bond et al. A multiwavelength view of the TeV blazar markarian 421: Correlated variability, flaring, and spectral evolution. *The Astrophysical Journal*, 630(1):130–141, sep 2005.

- [18] Markus Böttcher. Modeling the emission processes in blazars. In Josep M. Paredes, Olaf Reimer, and Diego F. Torres, editors, *The Multi-Messenger Approach to High-Energy Gamma-Ray Sources*, pages 95–104, Dordrecht, 2007. Springer Netherlands.
- [19] C. Deil and R. Lefaucheur et al. Zanin. Gammapy - A prototype for the CTA science tools. In *35th International Cosmic Ray Conference (ICRC2017)*, volume 301 of *International Cosmic Ray Conference*, page 766, January 2017.
- [20] Charles D Dermer, Steven J Sturmer, and Reinhard Schlickeiser. Nonthermal compton and synchrotron processes in the jets of active galactic nuclei. *The Astrophysical Journal Supplement Series*, 109(1):103, 1997.
- [21] F. Di Pierro, L. Arrabito, and A. Baquero et al. Larriva. Monte carlo studies of combined magic and lst1 observations, 2019.
- [22] A. Domínguez, J. R. Primack, D. J. Rosario, and F. et al. Prada. Extragalactic background light inferred from AEGIS galaxy-SED-type fractions. *Monthly Notices of the Royal Astronomical Society*, 410(4):2556–2578, 01 2011.
- [23] A. Donath, C. Deil, and R. Terrier et al. Gammapy: v.0.19, November 2021.
- [24] Florian Eppel. *Variability Study of High-Peaked BL Lac Objects at Millimeter Wavelengths*. December 2021.
- [25] Jun-Hui Fan, Yong Huang, Tang-Mei He, Jiang He Yang, Tong Xu Hua, Yi Liu, and Yong Xiang Wang. Radio Variability and Relativistic Beaming Effect for Blazars\*. *Publications of the Astronomical Society of Japan*, 61(4):639–643, 08 2009.
- [26] G. Fossati, L. Maraschi, A. Celotti, A. Comastri, and G. Ghisellini. A unifying view of the spectral energy distributions of blazars. *Monthly Notices of the Royal Astronomical Society*, 299(2):433–448, 09 1998.
- [27] NRAO GBTIDL. Developer documentation, zfits format, 2016.
- [28] CTAO gGmbH. Cherenkov telescope array, 2022. Available on line.
- [29] G. Ghisellini, C. Righi, L. Costamante, and F. Tavecchio. The fermi blazar sequence. *Monthly Notices of the Royal Astronomical Society*, 469(1):255–266, apr 2017.
- [30] Francis Halzen and Dan Hooper. High energy neutrinos from the tev blazar 1es 1959+650. *Astroparticle Physics*, 23(6):537–542, 2005.
- [31] D. Heck, Johannes Knapp, J-N. Capdevielle, George C. Schatz, and T. J. Thouw. Corsika: A monte carlo code to simulate extensive air showers. 1998.
- [32] J. Heidt and K. et al. Nilsson. High-resolution imaging of einstein slew survey bl lacertae objects, 1998.
- [33] A Michael Hillas. Cerenkov light images of eas produced by primary gamma. In *19th Intern. Cosmic Ray Conf-Vol. 3*, number OG-9.5-3, 1985.
- [34] M. Kadler, U. Bach, and Berge et al. *TELAMON: Effelsberg Monitoring of AGN Jets with Very-High-Energy Astroparticle Emissions*. August 2021.
- [35] Stefan Karge. The frankfurt quasar monitoring project, 2011-2022.
- [36] Demosthenes Kazanas and Apostolos Mastichiadis. Relativistic electrons in blazars: a hadronic origin? *The Astrophysical Journal*, 518(1):L17, 1999.
- [37] Sonia Khatchadourian, jean-christophe Prévotet, and Lounis Kessal. A neural solution for the level 2 trigger in gamma ray astronomy. 03 2007.

- [38] H. Krawczynski, S. B. Hughes, D. Horan, and F. Aharonian et al. Multiwavelength observations of strong flares from the TeV blazar 1es 1959650. *The Astrophysical Journal*, 601(1):151–164, jan 2004.
- [39] T. P. Li and Y. Q. Ma. Analysis methods for results in gamma-ray astronomy. , 272:317–324, September 1983.
- [40] B. F. Liu, R. E. Taam, E. Qiao, and W. Yuan. Coronal accretion: the power of X-ray emission in AGN. In Y. Meiron, S. Li, F. K. Liu, and R. Spurzem, editors, *Star Clusters and Black Holes in Galaxies across Cosmic Time*, volume 312, pages 52–55, February 2016.
- [41] M.S. Longair. *High Energy Astrophysics*. Cambridge University Press, 2010.
- [42] Michael F. L’Annunziata, Željko Grahek, and Nataša Todorović. Chapter 6 - cherenkov counting. In Michael F. L’Annunziata, editor, *Handbook of Radioactivity Analysis: Volume 2 (Fourth Edition)*, pages 393–530. Academic Press, fourth edition edition, 2020.
- [43] JM MacLeod and BH Andrew. The radio source vro 42.22. 01. Technical report, NATIONAL RESEARCH COUNCIL OF CANADA OTTAWA (ONTARIO) RADIO AND ELECTRICAL . . . , 1968.
- [44] MAGIC Collaboration, Acciari, V. A., Ansoldi, S., and Antonelli, L. A. et al. Broadband characterisation of the very intense tev flares of the blazar 1es 1959+650 in 2016. *A&A*, 638:A14, 2020.
- [45] D. Mazin. ”status and results of the prototype lst of cta”. *ICRC 2021: Astroparticle Physics Conference, Berlin, Germany*, 07 2021.
- [46] A. Moralejo Olaizola and R. López Coto. Lst analysis school, jan 2022.
- [47] Curator: J.D. Myers. Fermi gamma-ray space telescope, 2022. Available on line.
- [48] Curator: J.D. Myers. Neil gehrels swift observatory, 2022. Available on line.
- [49] Olivera-Nieto L. Nigro C., Hassan T. ”evolution of data formats in very-high-energy gamma-ray astronomy”. *Universe*, 7:374, 2021.
- [50] T. Nishiyama. Detection of a new TeV gamma-ray source of BL Lac object 1ES 1959+650. In *26th International Cosmic Ray Conference (ICRC26)*, Volume 3, volume 3 of *International Cosmic Ray Conference*, page 370, August 1999.
- [51] S. R. Patel, A. Shukla, V. R. Chitnis, D. Dorner, K. Mannheim, B. S. Acharya, and B. J. Nagare. Broadband study of blazar 1es 1959650 during flaring state in 2016. *Astronomy & Astrophysics*, 611:A44, mar 2018.
- [52] Asaf Pe’er and Eli Waxman. Time-dependent numerical model for the emission of radiation from relativistic plasma. *The Astrophysical Journal*, 628(2):857, 2005.
- [53] R. Floyd R. Penrose. ”extraction of rotational energy from a black hole”. *Nature Physical Science*, 229:177–179, 1971.
- [54] Bhoomika Rajput and Ashwani Pandey.  $\gamma$ -ray flux and spectral variability of blazar ton 599 during its 2021 flare. *Galaxies*, 9(4):118, 2021.
- [55] Anita Reimer, M Böttcher, and S Postnikov. Neutrino emission in the hadronic synchrotron mirror model: the “orphan” tev flare from 1es 1959+ 650. *The Astrophysical Journal*, 630(1):186, 2005.
- [56] Frank M Rieger and Peter Duffy. Shear acceleration in relativistic astrophysical jets. *The Astrophysical Journal*, 617(1):155, 2004.

- [57] George B Rybicki and Alan P Lightman. *Radiative processes in astrophysics*. John Wiley & Sons, 1991.
- [58] Jonathan F Schachter, John T Stocke, Eric Perlman, Martin Elvis, Ron Remillard, Arno Granados, Jane Luu, John P Huchra, Roberta Humphreys, C Megan Urry, et al. Ten new bl lacertae objects discovered by an efficient x-ray/radio/optical technique. *The Astrophysical Journal*, 412:541–549, 1993.
- [59] Marek Sikora, Mitchell C Begelman, Greg M Madejski, and Jean-Pierre Lasota. Are quasar jets dominated by poynting flux? *The Astrophysical Journal*, 625(1):72, 2005.
- [60] Andrei Sokolov, Alan P Marscher, and Ian M McHardy. Synchrotron self-compton model for rapid nonthermal flares in blazars with frequency-dependent time lags. *The Astrophysical Journal*, 613(2):725, 2004.
- [61] Maddalena Spada, Gabriele Ghisellini, Davide Lazzati, and Annalisa Celotti. Internal shocks in the jets of radio-loud quasars. *Monthly Notices of the Royal Astronomical Society*, 325(4):1559–1570, 2001.
- [62] Maurizio Spurio, Spurio, and Bellantone. *Probes of Multimessenger Astrophysics*. Springer, 2018.
- [63] M.C. Stroh and A.D. Falcone. *ApJS*, 207(28), 2013.
- [64] C. Megan Urry and P. Padovani. Unified schemes for radio-loud active galactic nuclei. *Publications of the Astronomical Society of the Pacific*, 107:803, sep 1995.
- [65] P. J. Young, J. A. Westphal, J. Kristian, C. P. Wilson, and F. P. Landauer. Evidence for a supermassive object in the nucleus of the galaxy M87 from SIT and CCD area photometry. , 221:721–730, May 1978.